Laser Wakefield Acceleration of Electrons to GeV Energies and Temporal Laser Pulse Compression Characterization in a Capillary Discharge Waveguide

Paul Andreas Walker
Merton College, Oxford

Thesis submitted in fulfillment of the requirements for the degree of Doctor of Philosophy at the University of Oxford

Trinity, 2013

Abstract

This thesis presents results from three strands of experimental work aimed towards establishing more reproducible, higher energy, and more accurately measured electron beams generated by a laser-driven plasma accelerator. The first experiment calibrated two types of detector frequently used to measure the bunch charge in laser wakefield accelerator experiments, namely scintillating screens and image plates. The experiments undertaken at the DAFNE beam test facility in Frascati, Italy, confirmed that the fluorescence signal from Kodak Lanex Regular screens varies linearly with the charge density for a nanosecond electron bunch for charge densities in the range between $\rho = 2 \times 10^{-7}\,\mathrm{C/m^2}$ to $\rho = 10^{-5}\,\mathrm{C/m^2}$. A sensitivity measurement of FUJIFILM BAS-IP MS image plates resulted in a sensitivity of $S_{MS} = (0.0487 \pm 0.0028)\,\mathrm{PSL}$, which is 2.4 times higher than had been assumed prior to this work.

The second strand aimed at improving the operation of the capillary discharge waveguide by re-designing the discharge circuit and the waveguide housing. The experiment showed that combining a glow discharge circuit with the pulsed discharge circuit of the capillary discharge waveguide reduced electrical noise, the timing jitter between the trigger pulse and the discharge, and the voltage required to initially break down the capillary gas for pressures below 10 mbar and above 150 mbar. The size of the housing of the capillary discharge waveguide was reduced in all three dimensions by an average of 60 %, enabling the device to be used in future staging experiments, and an open design of the housing eliminated the possibility of unwanted discharges. The new capillary design performed without flaw in the Astra-Gemini experiment and no disadvantages compared with the old housing were found.

The third strand of work describes an experiment undertaken with the Astra-Gemini laser at the Central Laser Facility of the Rutherford Appleton Laboratory, United Kingdom. The improved capillary discharge waveguide was used to generate GeV-scale electron beams with good reproducibility. Beams of electrons with energies above 900 MeV, and with root-mean-square divergence of 3.5 mrad, were observed for a plasma density of $2.2 \times 10^{18}\,\mathrm{cm^{-3}}$ and a peak input laser power of 55 TW. The variation of the maximum electron energy with the plasma density was measured and found to agree well with simple models. The energy spectra of the generated electron beams exhibited good shot-to-shot reproducibility, with the observed variations attributable to the measured shot-to-shot jitter of the laser parameters. Two methods for correcting the effect of beam pointing variations on the measured energy spectrum were tested and it was found that using a thin Lanex screen in front of the electron spectrometer was easy to implement and did not degrade the recorded energy spectrum. The first observation of temporal compression of a laser pulse within a plasma channel with simultaneous electron acceleration to energies higher than 500 MeV is also presented. This measurement suggests that the pulse compresses linearly from the back as predicted by theory.

To my wife and parents

Acknowledgements

I want to mention at the very outset of this thesis that whatever virtue you may find in this thesis is most likely due to in large part the advice, discussions, and assistance I received from many of my colleagues and friends. Foremost, of course, I want to thank my advisor, Simon. After discussions with you, I always felt newly motivated, and ready to move on with the next things that needed doing in the lab. You guided me through my DPhil and I will forever be thankful to you for your kind encouragements, honesty, and patience. I am sure you had to accumulate a lot of patience when reading my first drafts of this thesis. My favorite comment on my thesis was about beer, which at that point I am sure you were ready for. It came about when I tried to describe the process of using a 3-D print of a prototype and I had forgotten to include the letter r in the word print. Your comment: “3-D PINT?!? sounds lovely, but I think you mean print." Thank you very much, Simon, for your endurance, guidance, and advice.

Thank you to everyone in Simon’s group, who supported me in many different ways. Thank you very much Nicolas for all the help in endless tasks: simulations, coding, data analysis, laser and capillary alignment, labview, MATLAB, ... you name it, Nicolas can do it. Moving next to your desk during my third year in Oxford, upgraded my experience in the Clarendon laboratory enormously. My only regret is that I did not take advantage of the free French lessons. When can I come and visit you in Martinique? Wolf and James eased long night shifts with German computer skills and British humour. I am sure James will be happy to have upgraded to worthier tasks, than correcting my English while reading chapters of my thesis, shielding cameras with aluminium, and saving each FROG data shot by hand over a period of eight hours. And Wolf is probably very happy to finally write his own thesis rather than helping me to collect data. All these tasks however were very valuable to me. And Chris, thanks for recycling all the Ghirardelli chocolate wrappers, future generations will thank you as well. During my early years, Tom RR and Tom I both helped me get to grips with LWFA terminology and explanations during car and train rides to RAL and while working on the interferometry set-up, which always seemed so close to being done. Svet, thank you for your company and advice during endless hours of MATLAB coding on our fancy new Macs in our window less office. The food options during the night weren’t great, but the dinner parties with your roommates always fun. Kevin and the HHG crew were great company in the lab and thank you Kevin for the burrito lunches and words of encouragement during the final days. It was a ball to be part of the Simon room collective and share lunches with the members of Andrea’s, Justin’s and Gianluca’s group, never short on advice or a game of soccer in the park after lunch.

The experiments described in this thesis were performed mainly at the Rutherford Appleton Laboratory and thanks goes to everyone who worked on this endeavour: the MPQ group with Andreas Maier, Johannes Wenz, Natty Kajumba, and Christian Werle, whose endurance and advice was incredible needed, and without them a successful ending of the

experiment would have been extremely hard to accomplished; Florian Grüner and Stefan Karsch, the bosses who make these things happen; the Imperial College group, with Matt Streeter, Stefan Kneip, Michael Bloom, Stuart Mangles, and Zulfikar Najmudin, with whom we set-up and shared many evenings together in the pub; Dan Symes, who was an excellent and never tired liaison to our experiment who can and will do almost everything for your experiment; P. Rajeev, Steve Hawkes, Oleg Chekhlov, Chris Hooker, Bryn Parry, Y. Tang, Pete Brummit, Ali Zayyani, and the three D's David Rathbone, Darren Neville and Dave Rose, engineers and scientists at the Central Laser Facility; and of course the Leverhulme grant for the tasty dinners and travel arrangements.

During the experiments performed in Italy I was helped by Nicolas Delerue and a whole array of people from the John Adams Institute for Accelerator Science such as Riccardo Bartolini, George Doucas, Armin Reichold, David Urner, and Ken Peach. Many thanks goes to them for helping me enjoy the weather, good food, and espresso and, of course, perform the experiment. For my first year Berkeley research visit, I am thankful to Wim Leemans who organized it, to Tony who explained to me really everything in the lab in simple terms, and Carl and Cameron, who were extremely helpful in explaining to me the details of LWFA theory in my early years.

The guys from the Clarendon workshop taught me how to machine and I just wish I had some of these machines in my basement. Many thanks goes to Rob and Matt, who are wonderful teachers in the art of machining, and Simon, and Mark for the ideas and suggestions over the years. Luis and Anthony helped me understand electrical discharge better with their wealth of knowledge and teaching quality. Thank you also to Sue Gardner and Sue Geddes, for your advice on everything administrative, and to Tom, who did indeed rush your order if you really needed it. Alan provided me with the right amount of ducktape, i.e. lots! I think every experimental thesis should contain some sort of ducktape, if not, it might be considered a theoretical piece of work.

In preparing my thesis I read many doctoral theses and I want to thank the students who wrote them. While one often hears that no-one will ever read your thesis, I find that to be false statement of well written theses. Papers might be quoted often and hopefully fully read, but within a thesis, students talks to other students in more detail, which makes life of later students more pleasant and durable. Especially helpful were theses by Thomas Rowland-Rees, Tony Gonsalves, Matthias Fuchs, Stuart Mangles, Svet Bajlekov, and Chris Murphy, whose introduction is worth reading for all new students of LWFA. I gained much insight reading their theses and many thanks goes to them. If something sounds familiar to any of these people, it's probably because it made so much sense reading your thesis that I just never forgot the way you explained it. Thanks for that!

Thank you to Brigitte Cros and Peter Norreys for taking time to read my thesis and examining me. It was a very happy and encouraging exam. I would do it again! Michail Tzoufras and Christopher Murphy not only read my final version, but took time to pretend examining me and I cannot emphasize how important this was to my success in my viva. Thank you.

I want to thank my wife: without her, I might not have ever finished. Her encouragement and time to listen to me were crucial and I am so thankful for her. The painful task of final read was "awarded“ to her, which, I am sure was not much fun, given that the whole thesis did not have any or had only wrongly placed commas in it. Danke mein Schatz!

I want to thank very much my parents for their support during my graduate studies, a continuing effort from my undergraduate studies. They have always encouraged me, pushed me, and supported me and without their help and advice it would have been hard to under-

take such efforts at all. Thanks for your visits and the time you spent listening to my worries. I also want to thank Doris und Klaus Bergdolt, who visited me in Oxford during my third year. Their visit and enthusiasm for Merton and Oxford encouraged me further to continue my studies.

Lastly, I would like to thank all staff at the various libraries I wrote this thesis in, without their work and the free access to them I would have been confined to my desk at home, and there are just too many distractions. In particular I want to thank the staff of the University of San Francisco at Parnassus Campus, wherein I spend the better part of 2012. While visiting friends and family, the public nature of other libraries allowed me to work undisturbed in different cities, and many thanks goes to the libraries and their staff (and the tax payers of course) of UC Berkeley, Stanford, UCLA, Heidelberg and the sport center cafe of the University of San Francisco.

Contents

List of Figures

List of Tables

Chapter 1

Overview

The Large Hadron Collider (LHC) situated on the border of Switzerland and France provides an extraordinary tool with which to discover new science. While the LHC might have been the most visible accelerator in recent years, other accelerators that are smaller and more numerously available, provide a diverse community of medical, biological, chemical and physical scientists with the tools to probe materials and study life. Such accelerators allow scientists to advance knowledge, probe theories and engineer new devices. Synchrotrons in which electrons are accelerated, stored in large circular rings, and their radiation harnessed to irradiate matter are one example of such accelerators. Free-electron lasers, a more recent invention, are another example in which radiation is generated via undulating electrons at the end of linear accelerators.

All currently available accelerators within user facilities are based on conventional radio-frequency acceleration, meaning that charged particles are accelerated in the electric fields established between conducting electrodes or excited in an electromagnetic cavity. Fig. 1.1 (a) shows the SLAC Linear Accelerator Laboratory which operates a two miles long linear conventional accelerator. Conventional accelerators are built of materials which can sustain fields of order 50 MV/m before electrical break down occurs and, therefore, conventional accelerators have to be long to create high energy particle beams. In contrast, plasma accelerators use fields within a plasma to accelerate particles. Since in a plasma the atoms or molecules are already ionised, these accelerators are not subject to electrical breakdown limits that affect conventional accelerators. As we will see in detail in chapter 2, the accelerating field developed in a plasma accelerator can be three or even four orders of magnitude larger than in a radio-frequency accelerator, and as a consequence, kilometre scale machines can, in principle, be reduced to the metre scale. Therefore, plasma based accelerators present a great step forward in creating new, cheaper and much shorter accelerators for science.

1.1 Outline of the thesis

This thesis describes work aimed at improving the operation of the Oxford capillary discharge waveguide. Its primary aim is to establish a more reproducible, higher energy electron beam and to characterise the electron and laser beam parameters. It also describes

(a) (b)

Figure 1.1: (a) Photograph of the SLAC National Accelerator Laboratory which operates a two-mile linear conventional accelerator, the housing of which can be identified by its linear, white roof. Photo courtesy of SLAC Linear Accelerator Laboratory. (b) Photograph of the Rutherford Appleton Laboratory (RAL) at which the Central Laser Facility (CLF) is situated. The Diamond Light Source, a synchrotron science facility, can be identified as a circular structure with a circumference of about 550 m. Photo courtesy of Central Laser Facility.

experiments aimed at providing a reliable calibration of the image plates which are frequently used to measure the charge of laser-accelerated electron bunches. The thesis is organized as follows.

Chapter 2 The introduction chapter provides a brief review of laser plasma accelerators and examples of waveguides used in the field. The chapter starts with the introduction of the ponderomotive force responsible for creating plasma waves along with non-linear effects and limitations to energy gain of the accelerated electrons. It also presents scaling laws for linear and non-linear regimes. The chapter closes with a discussion of techniques of controlling injection and guiding intense laser pulses.

Chapter 3 describes experiments to calibrate the image plates (IP) used to measure the charge of laser-accelerated electron bunches. Prior to this work the calibration used was based on x-ray experiments and simulations. In the experiments described here, two kinds of detectors — scintillating screens and image plates — were exposed to a 505 MeV beam from a conventional accelerator. It was found that the response of the scintillating screen was linear with charge density. The sensitivity of the IP was found to be higher than had been assumed prior to this work, in agreement with later work by another group.

Chapter 4 describes work aimed at improving the operation of gas-filled capillary discharge waveguides. The chapter starts with a brief discussion of electrical discharges and their properties before a combined glow and pulsed discharge is introduced. The redeveloped discharge proved to reduce noise, main discharge jitter and breakdown voltage. However, it was not used during the experiment described in chapter 6 due to the small operable pressure range. The miniaturising and improvement over previous designs of the housing of the capillary discharge waveguide are described at the end of the chapter.

Chapter 5 The methods used to analyse data from an experiment using the hydrogen-filled capillary discharge waveguide are presented. First, the experimental setup at the Astra-Gemini facility is presented. This includes the laser facility, the optical diagnostics to record the transmitted laser radiation, and the electron diagnostics. Two methods for correcting the effect of electron beam pointing variations on the measured energy spectrum are described, and suggests that using a thin scintillating screen in front of the electron spectrometer is beneficial. The analysis of the laser and electron data is presented last.

Chapter 6 Results from a LWFA experiment using the hydrogen-filled capillary waveguide are presented. In these experiments, electrons were accelerated up to energies of 1 GeV. The reproducibility of the acceleration, within the capillary discharge waveguide, is demonstrated by the result of 36 consecutive electron spectra at energies close to 1 GeV. The reproducibility at this high energy level is the highest of any experiment up to today. The shot-to-shot variations was found to be attributable in large part to fluctuations in the pointing and energy of the driving laser pulses. The variation of the maximum electron beam energy with the plasma density was found to be in agreement with simple analytic models. Injection and acceleration of electrons was also observed at the lowest plasma density published at the time of the experiment. The first observation of temporal pulse compression within a plasma channel, with simultaneous electron acceleration to energies higher than 500 MeV, is presented. The pulse duration is found to decrease linearly with increasing plasma density, in reasonable agreement with a simple model of the pulse compression. The experimental results of the pulse compression are compared to simulations.

Chapter 7 A summary of results, together with an overview of future work is presented.

1.2 Role of the author

The data presented in chapter 3 were recorded during an experiment undertaken in Frascati, Italy. The author shared beam time at the facility with a group from the John Adams Institute in Oxford, which was led by Dr. Nicolas Delerue. All equipment used during the charge calibration experiment were designed, built, and tested by the author. At the experimental site, the author was assisted in data collection by Dr. Nicolas Bourgeois. The data were analysed by a code written by the author for this purpose.

The data presented in chapter 4 were collected and analysed by the author in Oxford during 12 months of redevelopment of the capillary discharge waveguide and its housing. All prototypes, and final designs were built by the author.

The data presented in chapter 6 were collected during an experimental campaign at the Astra-Gemini laser facility at the Central Laser Facility of the Rutherford Appleton Laboratory in Didcot, United Kingdom (Fig. 1.1 (b)). The experiment campaign was led by the author. The experiment was performed by the author and other members of Professor Simon M. Hooker's research group, together with four members of Professor Florian Grüner's and Professor Stefan Karsch's group, both from the Max-Planck Institute for Quantum Optics in Garching. All participating members made sizable contributions to the experiments and the experiment would have not been a success without them. The experiment was setup in col-

laboration with members from Dr. Stuart P. D. Mangles' and Professor Zulfikar Najmudin's research groups from Imperial College London, for which we are very thankful. The waveguide and its housing, required to create electron beams, and the novel electron spectrometer, to record the energy of the electron beams, was designed and built by the author prior to the experiment. Data acquisition for the diagnostics was carried out by an automated system coded by Dr. Nicolas Bourgeois. All data analysis was carried out by the author, using code written by the author for this purpose.

The author also participated in a number of experiments that are not presented in this thesis. These included: an LWFA campaign at the Astra-Gemini laser in June/July 2008 [1, 2]; an experiment to use radio-frequency discharges for capillary pre-ionisation with Dr. Anthony Dyson in 2009; an experiment with the Max-Planck Institute for Quantum Optics to use electrical pre-pulses to ionise the capillary gas in 2009; an experiment to measure the emittance of electron beams in a single shot using pepper-pots and transition radiation detectors with Dr. Nicolas Delerue in 2009 [3]; and interferometric measurements of the electron density inside the capillary undertaken with Dr. Thomas Ibbotson in 2009 [4].

All figures are the author's own work, unless credited otherwise.

Chapter 2

Introduction

In this chapter, a historical introduction of plasma based acceleration using a laser pulse is given and the theory of laser-driven plasma accelerators is introduced. Techniques and experiments used in the field to place electrons in accelerating fields and to guide intense laser pulses conclude this chapter.

Section 2.1 begins with the historical review of key LWFA experiments. The force responsible for the creation of plasma waves is introduced in §2.2.1 and §2.2.2, and typical plasma parameters and electric field strength are discussed in §2.2.3. In §2.3, non-linear effects such as self-focusing (§2.3.2), self-guiding (§2.3.3) and pulse compression (§2.3.4) are discussed. Pulse compression is accompanied by shifts in the spectrum of the laser radiation and this will be addressed in §2.3.5. Limits on the maximum energy electrons can gain due to diffraction (§2.4.1), dephasing (§2.4.2), depletion of the laser pulse (§2.4.3), and beam loading (§2.4.4) are discussed in §2.4. The section will close with a discussion on energy scaling laws in the linear and non-linear regimes in §2.4.5.

Section 2.5 gives an overview of how electrons are placed in the accelerating fields of the plasma wave, with a review of techniques and experiments that use these techniques, such as self-injection (§2.5.1), optical injection (§2.5.2), density transition injection (§2.5.3) and injection via ionisation potentials (§2.5.4). Step refractive index guiding as well as gradient index guiding techniques are discussed in §2.6.1 and §2.6.2. The waveguide used in experiments described in chapters 5 and 6 is introduced in §2.6.3 with a discussion on plasma channel formation.

2.1 Laser-driven acceleration of electrons in plasma

The great potential of plasma waves for particle acceleration was first recognized by Tajima and Dawson in 1979 [5]. The longitudinal plasma waves excited by intense laser pulses are well suited for accelerating charged particles to relativistic energies, because they also propagate with speed near c and can stay in phase with such high-energy particles. Laser-driven plasma accelerators operate in several regimes, depending on the intensity of the driving laser pulse, the density of the plasma, and the duration of the laser pulse relative to the plasma period. A historic review of key experiments from the laser wakefield acceleration scheme (LWFA) in which the pulse length τ is of order of the plasma frequency is discussed.

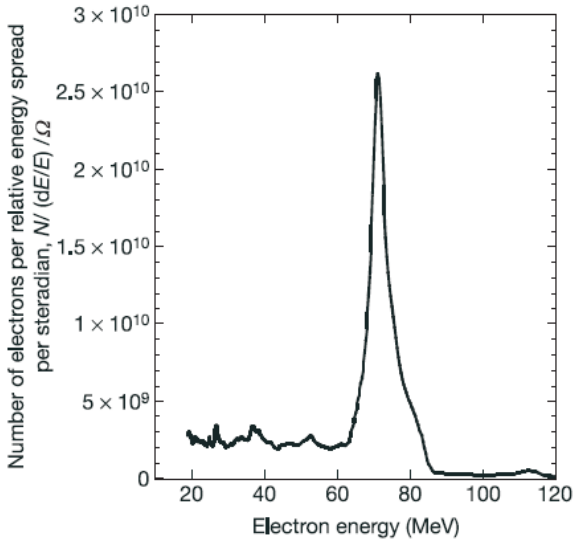

Figure 2.1: Electron spectrum from one of the three "dream-beam" experiments from 2004. The electron beam was accelerated within a laser plasma accelerator using a gas-jet. This figure was taken from [14].

Other laser plasma acceleration schemes, in operation prior to the advent of laser pulses with such short pulses — for example self-modulated laser wakefield acceleration [6, 7] and plasma beat wave acceleration [5, 8] — are not described. A comprehensive review of the physics of these regimes has recently been provided by Esarey et al. [9].

At the time Tajima and Dawson [5] proposed using lasers to accelerate particles the technology for ultra-short high-intensity laser pulses did not exist. However laser technology developed rapidly, most notably through the development of chirped pulse amplification (CPA) in 1985 [10]. CPA involves stretching the laser pulse in time before amplifying it in a gain medium. Because the pulse is stretched, previous limits on intensity, which were imposed by the damage threshold of the gain medium, are eliminated. After re-compression, the laser pulse can have a peak power of many terawatts and a pulse duration of below 50 fs.

The advent of CPA has enabled developments in LWFA to be fast. Early work on laser-driven plasma accelerators [11–13] drove electron energy to greater than 100 MeV but the generated electron beams had very broad energy spectra. The field took a big step forward when three groups in 2004 [14–16] reported for the first time quasi-monoenergetic energy spectra in the 100-200 MeV range with a small energy spread of a few percent. In that work, the target plasma was formed by ionisation of a gas jet by the driving laser [14, 15], or a plasma channel formed by additional laser pulses [16]. Fig. 2.1 shows an electron spectrum from the gas-jet experiment at the Astra laser facility [14].

In 2006, the energy of laser-accelerated electron beams was increased to 1 GeV by guiding the driving laser pulse in the plasma channel formed in a capillary discharge waveguide [17, 18]. Fig. 2.2 shows energy spectra for electron beams with energies of 0.5 GeV (bottom) and 1 GeV (top). In the five years that followed, electron beams with 100s of MeV have been produced by several groups in either capillary discharges or capillary tubes [1, 2, 19–21] and in gas jets or gas cells [22–25]. During this period, techniques for controlling LWFA experiments became more commonplace [25–27]. For example, in 2006 counter-propagating beams were used to control the energy of the accelerated electrons [26]. In 2008, the waveg-

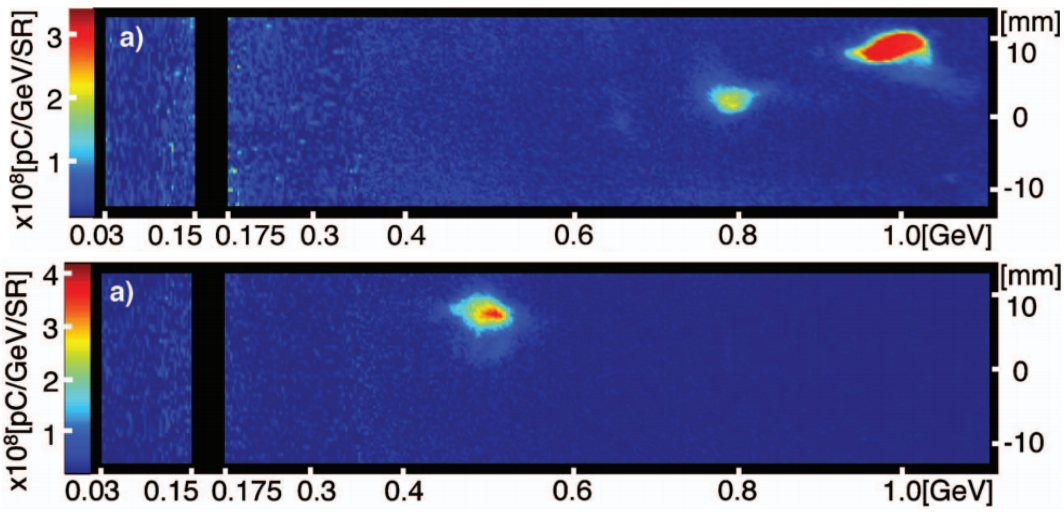

Figure 2.2: Energy spectra for electron beams with energies of 0.5 GeV (bottom) and 1 GeV (top) accelerated in a laser plasma accelerator. These single shot electron energy spectra were recorded in 2006 and taken from [18].

uide used in 2006 to accelerate electrons to 1 GeV, was used without the discharge, which generated beams that were more stable although they had less energy [28]. Techniques and experiments which give more control of the accelerated beam are discussed in more detail in §2.5.

Improving the quality of the accelerated electrons involves not only knowing plasma and electron beam parameters, but also measuring the properties of the laser pulse transmitted through the plasma. In 2005, laser pulse shortening of an initially 38 fs short pulse down to ≈ 12 fs was observed [29]. The broadened optical spectrum — indicative of pulse compression — is shown in Fig. 2.3. The amplitude of plasma waves was measured in 2009 by measuring the wavelength shift [30] and in 2010, asymmetric pulse compression was measured in an experiment [31], in which the authors scanned the plasma length as well as the plasma density. The experiments in 2005 and 2010 both measured the pulse duration of the laser pulse, but neither experiment accelerated electrons simultaneously.

This brings us to the year 2012, in which the current electron beam energy record of > 2 GeV [32] has recently been reported, which is a promising outlook for the future of laser-driven acceleration of electrons in plasmas.

2.2 Introduction to laser plasma interaction

Tajima and Dawson [5] realized the great potential of laser pulses to accelerate particles in plasmas in 1979. The concept of how these plasma waves are created is introduced in this section. The force responsible, the ponderomotive force, is introduced in §2.2.1, the waves in the non-relativistic regime are discussed in §2.2.2 and the section closes with a discussion of laser wakefield accelerator parameters in §2.2.3.

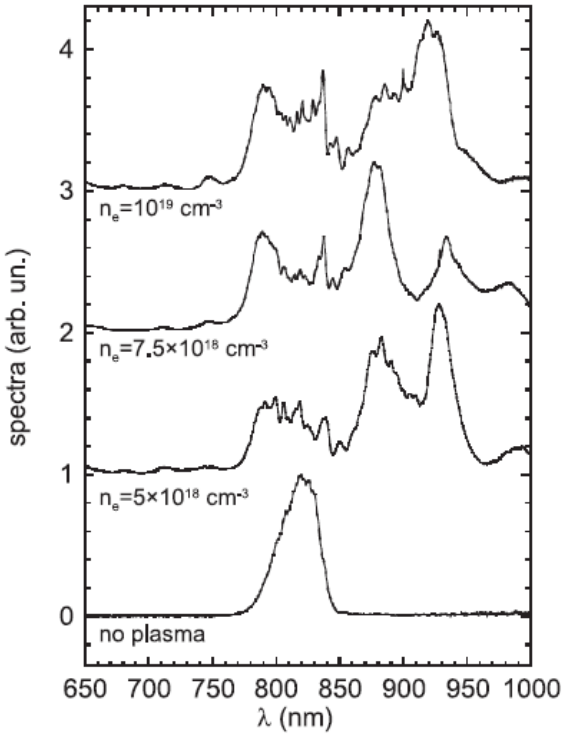

Figure 2.3: Transmitted laser spectra measured for different plasma densities from an experiment performed in 2005. The figure was taken from [29].

2.2.1 Ponderomotive force

The interactions between plasmas and intense laser pulses are often represented in terms of the normalized electromagnetic vector potential of the laser, $\mathbf{a} = e\mathbf{A}/\gamma mc$, and the normalized electrostatic potential, $\phi = e\Phi/\gamma mc^2$, with $\mathbf{A}$ and Φ being the non-normalized potentials in the Coulomb gauge. The constants e, m, and c are the elementary unit of charge, the electron mass, and the speed of light in vacuum, respectively and γ is the relativistic factor. The frequency of the laser will be denoted ω_0 in this introduction.

Within the plasmas of interest to LWFA, the number of negatively charged particles is equal to that of the positively charged. Because electrons are 1836 times lighter than protons, they move quickly when an electric field is applied. To a very good approximation, we can treat the ions as being stationary, and consider all of the response of the plasma to be due to the electrons. The ponderomotive force [33] can be derived by looking at the electron fluid momentum equation in this approximation:

$$\mathrm{d}\mathbf{p}/\mathrm{d}t = -e[\mathbf{E} + (\mathbf{v} \times \mathbf{B})] \tag{2.1}$$

where $\mathbf{p}$ and $\mathbf{v}$ are the momentum and velocity. The electric and magnetic fields can be written as $\mathbf{E} = -\partial\mathbf{A}/\partial ct$ and $\mathbf{B} = \nabla \times \mathbf{A}$ and we will consider the vector potential of the laser being polarised linearly, e.g. $\mathbf{A} = A_0\mathbf{e}_\perp cos(k_0 z - \omega_0 t)$, where $A_0 = |\mathbf{A}_{peak}|$ is the magnitude of the peak value of $\mathbf{A}$, $\mathbf{e}_\perp = (1,0,0)$ is the unit vector in the transverse direction, and $k_0 = 2\pi/\lambda_0$ is the wave vector of the laser pulse radiation of wavelength λ_0 and angular frequency ω_0. Considering the linear limit with $a_0 = eA_0/\gamma mc^2 \ll 1$, the second order motion of (2.1)

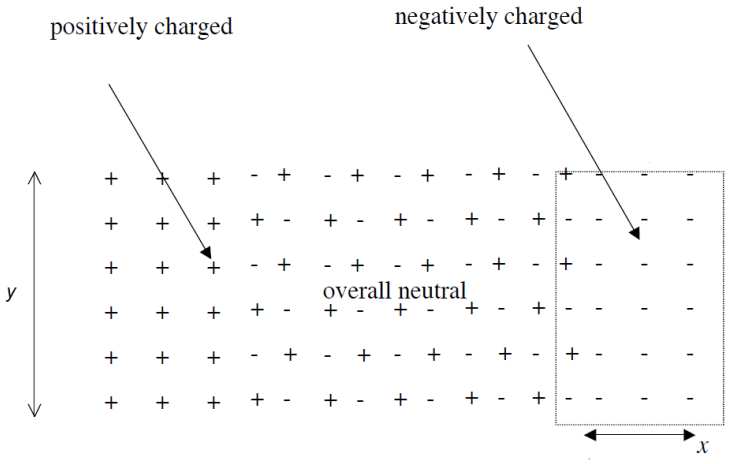

Figure 2.4: A plasma is shown schematically in which a section of electrons has been displaced to the right giving rise to electric fields. The figure was adapted from [35].

becomes

$$\mathrm{d}\mathbf{p}/\mathrm{d}t = -\frac{1}{4}\frac{e^2}{\gamma m\omega_0^2}\nabla a_0^2 \equiv \mathbf{F}_\mathrm{p} \tag{2.2}$$

which is the ponderomotive force. The most intuitive derivation of the ponderomotive force can be found in Dr. Christopher D. Murphy's thesis [34]. Simply put, the force pushes the electrons away from regions of high gradients of the intensity; this force is responsible for driving the plasma waves used to accelerate particles in a laser-plasma accelerator.

2.2.2 Plasma waves

To derive the plasma wave frequency, we will consider a plasma which is overall neutral with a laser pulse propagating along the x-axis. The ponderomotive force of the laser pulse pushes the electrons forward in the direction of the laser. When the laser pulse overtakes an electron, the electron is pulled back by the electrostatic attraction of the ions left behind. The electrons accelerate towards the ions — the ions will move slightly towards the electrons but, as we said, we will ignore this — until the electrons overlap with the ions and the force is zero. Because of their momentum, however, the electrons overshoot their original position and an oscillatory motion of the electrons around the ions is set up. The frequency of the oscillation is known as the plasma frequency ω_p.

Fig. 2.4 shows schematically a plasma in which electrons have been displaced by a distance x, for example by a laser pulse. As described in [35] we will consider the number of n_e electrons in the volume of length y and z which is displaced by a distance x. The field by which they are attracted towards the n_i ions can be calculated using Gauss law. At position x, it is

$$E \cdot y \cdot z = \frac{n_\mathrm{e} \cdot e \cdot x \cdot y \cdot z}{\epsilon_0}, \tag{2.3}$$

where $\epsilon_0 = 8{,}8542 \times 10^{-12}\,\mathrm{AsV^{-1}m^{-1}}$ is the electrical field constant. Using Newton's second

law of motion we find that

$$F = \gamma m \mathrm{d}^2x/\mathrm{d}t^2 = -eE = -\frac{n_\mathrm{e} e^2}{\epsilon_0} x. \tag{2.4}$$

We find the motion to be harmonic with the angular frequency

$$\omega_\mathrm{p} = \sqrt{\frac{e^2 n_\mathrm{e}}{\gamma m \epsilon_0}} \tag{2.5}$$

and ω_p is the previously introduced plasma frequency. Electron plasma waves are longitudinal electrostatic waves and, as seen in Eq. (2.5), only depend on the density n_e of the plasma. This is an oversimplification, due to the fact that, we considered the non-relativistic case in the cold plasma limit and that collisions are neglected. This is warranted, as the time τ_ei between collisions of electrons and ions is large compared to the oscillation motion i.e. $\omega_\mathrm{p}\tau_\mathrm{ei} \gg 1$.

2.2.3 Laser plasma accelerator

The plasma density wave set up by the laser pulse is known as a “plasma wakefield". This wakefield trails the laser pulse as it travels through the plasma with the group velocity

$$v_\mathrm{g} \approx c\left(1 - \frac{\omega_\mathrm{p}^2}{\omega_0^2}\right)^{1/2} \tag{2.6}$$

where ω_0 is the laser frequency. The phase difference between a region in which the wave starts at $t = t_1$ and a region where it starts at $t = t_2$ is given by $\Delta\Phi = \frac{v_\mathrm{g}}{\lambda_\mathrm{p}}(t_2 - t_1)$ and the laser drives a plasma wave at relativistic phase velocity $v_\mathrm{ph} = v_\mathrm{g}$ with a plasma wavelength of

$$\lambda_\mathrm{p} = \frac{2\pi v_\mathrm{g}}{\omega_\mathrm{p}}. \tag{2.7}$$

In order to estimate the electric field of the plasma wave E, we will consider a square pulse and limit the discussion to the linear limit — in which the vector potential of the laser field $a_0 = eA_0/\gamma mc \ll 1$. The leading edge of the laser pulse will perturb the plasma over roughly a time $\Delta t = \Delta x/c$, while propagating the distance Δx. In that time, the vector potential of the laser field rises from zero to a_0 and the ponderomotive force multiplied by the time gives us the momentum of the electrons:

$$p_x = F\Delta t \approx -\frac{1}{4}\frac{e^2}{\gamma m\omega_0^2}\frac{a_0^2}{\Delta x}\Delta t \approx -\frac{1}{4}\frac{e^2}{\gamma m\omega_0^2 c}a_0^2 \tag{2.8}$$

As described in §2.2.2 this leads to a longitudinal oscillatory motion of the electrons with frequency ω_p and hence a longitudinal oscillation of the amplitude of the electric field. The momentum of the plasma electrons in the wave becomes

$$p_x(t) = F\Delta t \times \cos(\omega_\mathrm{p} t) = -\frac{1}{4}\frac{e^2}{\gamma m\omega_0^2 c}a_0^2 \cos(\omega_\mathrm{p} t). \tag{2.9}$$

This momentum is caused by the ponderomotive force of the laser pulse and the electric field the electrons experience due to the plasma wave can be written as

$$E_x = -\frac{1}{e}\frac{\mathrm{d}p_x}{\mathrm{d}t} = \frac{1}{4}\frac{e}{\gamma m \omega_0^2 c} a_0^2 \omega_\mathrm{p} \cos(\omega_\mathrm{p} t). \tag{2.10}$$

The peak accelerating field is given by

$$E_0 = \frac{1}{4}\frac{e}{\gamma m \omega_0^2 c} a_0^2 \omega_\mathrm{p} \tag{2.11}$$

and hence proportional to ω_p. These electric fields within the plasma wave can reach magnitudes three orders of magnitude higher than the limit on conventional accelerators. In 1959, Dawson [36] introduced an equation to calculate the peak electric field before the plasma wave “breaks",

$$E_0^\mathrm{WB} \approx 96\sqrt{n_\mathrm{e}}. \tag{2.12}$$

which is referred to as the “cold non-relativistic wave-breaking" field with the plasma density n_e in units of cm^{-3}. Wavebreaking occurs when the electron fluid velocity of the plasma approaches the velocity of the plasma wave. For typical plasma densities present in LWFA experiments of the order of $n_\mathrm{e} \approx 1 \times 10^{18}\,\mathrm{cm}^{-3}$, the electric fields become $E_0^\mathrm{WB} \approx 100\,\mathrm{GV/m}$.

2.3 Non-linear effects

The interaction between the laser pulse and the plasma during the propagation in the plasma not only affects the plasma, vice versa the laser pulse is influenced by the plasma. The non-linear effects relevant to this thesis are discussed in this section, which encompasses non-linear plasma waves (§2.3.1), self-focusing (§2.3.2), self-guiding (§2.3.3), temporal pulse compression (§2.3.4) and the effect on the laser spectrum (§2.3.5).

High intensity laser pulses can experience strong evolution as they traverse through the plasma. This evolution is mainly governed by the variations of the index of refraction of the plasma, η, which is given by

$$\eta = \sqrt{1 - \frac{\omega_\mathrm{p}^2}{\omega_0^2}} \approx 1 - \frac{n_\mathrm{e} e^2}{2\gamma m \epsilon_0 \omega_0^2} \tag{2.13}$$

where the approximation holds if $\omega_0 \gg \omega_\mathrm{p}$. The following paragraphs describe some of the phenomena and are explained most easily with Eq. (2.13).

2.3.1 Non-linear plasma waves

As seen in §2.2.3, plasma waves in the linear regime are sinusoidal. If the laser pulse driving the plasma waves has sufficiently high intensity the plasma waves become non-linear. For high laser intensities, such that $a_0 > 1$, the electrons' velocity — also called quiver velocity — becomes relativistic and the electric field loses its sinusoidal form and steepens. This is shown in Fig. 2.5 where the electric field and the density perturbation are shown for the case of $a_0 = 2$. The electric fields are now sawtooth shaped and the plasma wave can sustain larger electric fields.

2.3.2 Self-focusing

In the absence of non-linear effects ($a_0 < 1$), a laser pulse focused into a uniform plasma will diffract. At higher intensities the laser forces electrons to relativistic energies, which has the effect of increasing their mass due to the γ factor; this, in turn, affects the refractive index experienced by the laser, as seen in Eq.(2.13). For a laser pulse with a radial profile $a(r) = a_0 e^{-r^2/2\sigma^2}$, Eq. (2.13) can be written as [38]

$$\eta = \sqrt{1 - \frac{\omega_p^2}{\omega_0^2 \sqrt{1 + a(r)^2/2}}} \tag{2.14}$$

and η is peaked on axis. The phase velocity $v_{ph} = c/\eta$ of the pulse traversing the plasma can then be approximated by

$$v_{ph} = \frac{c}{\eta} \approx c \left[1 + \frac{\omega_p^2}{2\omega_0^2} \left(1 - \frac{a(r)^2}{4} \right) \right]. \tag{2.15}$$

One can see that the phase front at the peak intensity, i.e. at the centre of the beam travels at a speed that is less than on its sides. This will cause the laser pulse to focus. A laser pulse with sufficient power can therefore experience relativistic self-focusing which cancels diffraction and the pulse can be guided over many Rayleigh lengths without a guiding structure such as a waveguide. The power requirement for self-focusing [39] to balance diffraction requires the power of the laser to be greater than the critical laser power P_c and can be expressed [40] as

$$P_0 > P_c = 17.4 \frac{\omega_0^2}{\omega_p^2} [\text{GW}]. \tag{2.16}$$

This condition is necessary for self-focusing but not sufficient for the laser pulse to be so-called self-guided.

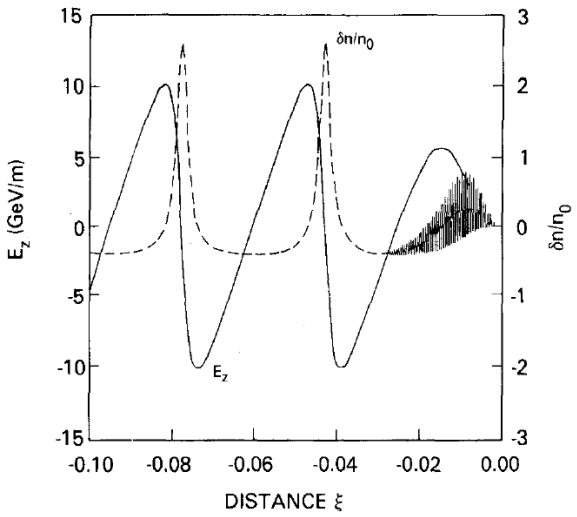

Figure 2.5: Density variations (dashed line) and electric field (solid line) in the non-linear regime. This figure was adapted from [37] where the laser pulsed traversed from the left to the right.

2.3.3 Self-guiding

Eq. (2.16) is valid for long laser pulses, but in many laser-plasma experiments $\tau < \lambda_p$, and in such cases, the behaviour is more complicated. For short laser pulses, the effect on η of the increase in electron density at the front of the laser pulse — due to the ponderomotive force — are canceled out by the effect on η of the relativistic mass increase of the electrons. This can be seen by taking Eq. (2.13) from which we know that the refractive index is dependent on the intensity of the laser pulse — described by either γ or a_0 — and the electron density n_e. Mori [41] shows this dependence in a very useful way by rewriting Eq. (2.13) into the change in refractive index, $\delta\eta$, with density and intensity and find that

$$\delta\eta \propto |a_0^2|/4 - \delta n \tag{2.17}$$

where δn is the density change normalized to the ambient plasma. Sprangle et al. [42] use this to find that, for $a_0 < 1$, the first term cancels the second and so the change in refractive index produced by the density increase is annihilated by the intensity increase meaning that, in the absence of external guiding, the head of the laser pulse diffracts essentially freely.

To limit the effect of a diffracting head of a laser pulse, Lu et al. [43] estimate the laser power required. They show that a laser pulse self-focuses to a spot size of $w_{sf} = 2c\sqrt{a_0}/\omega_p$ and that such a pulse of power P has a normalized vector potential of $a_0 = 2(P/P_c)^{1/3}$. Although the front of a short laser pulse propagating through a plasma diffracts more or less freely, the pulse can be said to be "self-guided" if the rate of erosion of the leading edge of the pulse by diffraction is slower than that caused by the transfer of the laser energy to the plasma wave. Lu et al [43] found that self-guiding requires that $a_0 > (\omega_0/\omega_p)^{2/5}$ which leads to a requirement of a minimum peak power of

$$P \gtrsim P_c^{\text{diff}} = \frac{1}{8}\left(\frac{\omega_0}{\omega_p}\right)^{6/5} P_c \tag{2.18}$$

Since $\omega_0 > \omega_p$ for the pulse to traverse the plasma, $P_c < P_c^{\text{diff}}$, meaning that in the absence of a waveguide relativistic self-guiding requires a laser power above P_c.

2.3.4 Pulse compression

Gordon et al. [44] point out that Eq.(2.17) equates to zero only at the front of the pulse: because the density at the back is lower — the ponderomotive force which increases the density at the front will ensure that fewer electrons are present at the back and centre — η at the back is increased compared to η at the front. Because the group velocity $v_g = c\eta$, the back of the pulse moves faster than the front and the pulse compresses from the back.

A simple model to analytically describe the rate of compression of a short pulse ($\tau c < \lambda_p$) can be derived by taking two points within a laser pulse separated by τ, one at the front and one at the back. Schreiber et al. [31] argue that the refractive index change over one plasma period is constant i.e. $\delta\eta/\delta x \approx (\eta_{min} - \eta_{max})/c\tau$. Having propagated over a distance L with different group velocities v_g^F and v_g^B, the separation between the two points changes with $c\Delta\tau/L = (v_g^F - v_g^B)/c = (\eta^F - \eta^B) \approx c\tau\frac{\delta\eta}{\delta x}$. For $n_0 \ll n_c$ where n_c is the critical plasma density

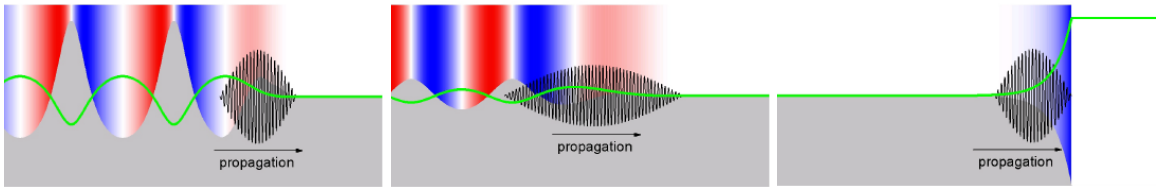

Figure 2.6: The figures shows the laser pulse (black solid line) traveling from left to right, causing the plasma density change (grey fill) and refractive index (green line). The refractive index gradient is shown in a colour scale varying from red (decelerating gradient) to blue (accelerating gradient) through white (zero gradient). The figure was adapted from [45].

$n_c = \frac{\omega^2 m_e \epsilon_0}{e^2}$ above which the plasma cannot sustain waves of frequency ω, the refractive index can be written as $\eta \approx 1 - \frac{1}{2}(n_e/\gamma n_c)$. For $a_0 > 1$, $\eta_{max} \approx 1$ and $\eta_{min} \approx 1 - \frac{n_{e0}}{2n_c}$ and the temporal pulse length evolution can be estimated as

$$\tau = \tau_0 - \frac{n_{e0} x}{2 c n_c}, \tag{2.19}$$

where n_{e0} is the initial plasma density.

For laser pulses that are longer than the plasma wavelength ($\tau c > \lambda_p$), the electron density perturbations caused by the laser pulse will diffract, focus, and compress the laser pulse at different points along the axis of the laser pulse. Where the density is high, η is low and vice versa. This so-called “self-modulation" of long laser pulses at a period of λ_p leads to pulse break up longitudinally and each pulse-let compresses and intensifies in its respective plasma bucket.

2.3.5 Spectral shifts

The change in refractive index which causes the temporal pulse compression also distorts the laser spectrum. This is necessary, because both are related via Fourier transform, and a compressed pulse must have a broader optical spectrum than the original, uncompressed pulse. As was done in [45][1], the change in the spectrum can be derived by observing two phase fronts separated by 2π, which are separated by the laser wavelength λ propagating though the plasma. The change in wavelength is given by

$$\frac{\mathrm{d}\lambda}{\mathrm{d}t} = -\frac{\lambda c}{\eta}\frac{\mathrm{d}\eta}{\mathrm{d}z} \tag{2.20}$$

and the change in frequency is given by

$$\frac{\mathrm{d}\omega}{\mathrm{d}t} = -\frac{\omega}{\eta}\frac{\mathrm{d}\eta}{\mathrm{d}t}. \tag{2.21}$$

Eq.(2.20) and Eq.(2.21) illustrate that a temporal change in η will lead to a frequency shift while a spatial change in η will lead to a change in the wavelength.

[1] In addition to this derivation from [45], the thesis of Christopher D. Murphy [34] has an excellent qualitative explanation of spectral shifts — called photon acceleration in his thesis — in section 5.2.2.

In LWFA experiments, the typical pulse length is shorter than the plasma wavelength ($c\tau < \lambda_p$). This scenario is shown in Fig. 2.6 (a), in which the change in refractive index is negative ($\frac{d\eta}{dz} < 0$), which causes the front of the pulse to be red-shifted ($d\lambda > 0$). Fig. 2.6 (b) depicts a pulse with $c\tau \approx \lambda_p$, which causes the back of the pulse, where $\frac{d\eta}{dz} > 0$, to be blue-shifted ($d\lambda < 0$). In this case, red-shifting can still be observed, which originates from the photons at the front of the pulse. Fig. 2.6 (c) shows the case in which ionisation of un-ionised species causes the pulse to be blue shifted ($d\lambda < 0$), because the refractive index change — this time at the front — is positive ($\frac{d\eta}{dz} > 0$).

2.4 Limitations and energy scaling

While one could think that acceleration and energy gain is limited by the length of the plasma and the strength of the electric field alone, there are more limitations on the maximum electron energy. Diffraction, electron de-phasing with the accelerating fields and the depletion of the energy in the laser beam are discussed in §2.4.1 to §2.4.3; beam loading which limits the charge and accelerating fields is introduced in §2.4.4. The effect these limitations have on the maximum energy electrons can gain is discussed in a section on energy scaling in §2.4.5.

2.4.1 Diffraction

Laser pulses for LWFA experiments are focused down to spot sizes, so that the intensity of the laser is maximized. The propagation of the laser pulse with a Gaussian radial intensity profile

$$I(r,z) = I(0,z)e^{-2r^2/W(z)^2} \tag{2.22}$$

moving along the z-direction is given by

$$W(z) = W_0\left(1+\left(\frac{z}{Z_R}\right)^2\right)^{1/2}. \tag{2.23}$$

Here, $Z_R = \pi W(0)^2/\lambda$ is the Rayleigh length, and W_0 is the spot size. The spot size is most commonly defined as $W_0 = \sqrt{2}\sigma$, where σ is the radius of the laser beam at which the intensity in the laser pulse has dropped to $1/e$ of its peak value.

The laser pulse diffracts and its peak intensity, given by

$$I(0,z) = \frac{I(0,0)}{1+(z/Z_R)^2}, \tag{2.24}$$

drops with propagation distance and thus an unguided laser pulse will drive a wakefield for only the length of the order of the Rayleigh range Z_R.

2.4.2 De-phasing

In a uniform plasma the phase velocity of a laser-driven plasma wave is close to, but slightly less, than c since the laser pulse propagates with a group velocity $v_g = \eta c < c$. The small

difference in the velocity of the accelerated electrons, which for relativistic energies is very close to c, and the velocity of the plasma wave causes the accelerated electron bunch to outrun the plasma wave. The electron bunch moves from an accelerating phase to a decelerating one after the dephasing length L_d which will be derived in the following paragraph.

The difference in the velocity of the electron and the laser pulse can be written as

$$\Delta v = c - c\sqrt{1-\left(\omega_\mathrm{p}^2/\omega_0^2\right)} \approx \frac{c\omega_\mathrm{p}^2}{2\omega_0^2}. \tag{2.25}$$

In linear theory, the accelerating part of the fields are $\lambda_\mathrm{p}/2$ long and the time electrons remain in the accelerating part before slipping in decelerating parts is given by

$$t_\mathrm{d} = \frac{\lambda_\mathrm{p}/2}{\Delta v}, \tag{2.26}$$

and hence one can derive an expression for the linear “dephasing length" L_d which is

$$L_\mathrm{d} = ct_\mathrm{d} = c\frac{\lambda_\mathrm{p}/2}{\Delta v} = \frac{\lambda_\mathrm{p}^3}{\lambda_0^2}. \tag{2.27}$$

For non-linear plasma waves, i.e. wakefields driven by laser pulses with a normalized vector potential $a_0 > 1$, the dephasing length can be written [43] as

$$L_\mathrm{d}^{nl} = \frac{2\sqrt{a_0}}{3\pi}\frac{\lambda_\mathrm{p}^3}{\lambda_0^2} = \frac{2\sqrt{a_0}}{3\pi}L_\mathrm{d} \tag{2.28}$$

2.4.3 Depletion

The energy to create the plasma wave is of course provided by the driving laser pulse and, because of energy conservation, the pulse loses energy while traveling through the plasma. Gordon et al. [44] expressed the length for the laser to lose all its energy in terms of the linear dephasing length:

$$L_\mathrm{pd} = \frac{L_\mathrm{d}}{2a_0^2}, \tag{2.29}$$

where “pd" stand for “pump depletion", and for $a_0 \ll 1$, $L_\mathrm{pd} > L_\mathrm{d}$.

In the non-linear case, the cavity behind the laser pulse enables the laser pulse to only engage the plasma at the front because the back sits basically in vacuum. This means that the depletion of the laser pulse happens at the front — the so-called “etching" of the pulse front [46] — from which photons are strongly decelerated and the pump depletion length for the non-linear case can be written as

$$L_\mathrm{pd}^{nl} \approx \frac{\lambda_\mathrm{p}^2}{\lambda_0^2}c\tau = \left(\frac{3\pi}{2\sqrt{a_0}}\frac{c\tau}{\lambda_\mathrm{p}}\right)L_\mathrm{d}^{nl}. \tag{2.30}$$

2.4.4 Beam loading

The electric fields inside the plasma wave are weakened by the fields of trapped electrons. This process is called “beam loading" and puts a limit on the number of accelerated electrons and the quality of the accelerated beams. The maximum number of electrons that can be “loaded" into a bucket was estimated by Katsouleas et al. [47] for the linear regime to be

$$N_{\max} \approx 5 \times 10^5 \frac{E_{\max}}{E_0} A \sqrt{n_e} \tag{2.31}$$

where A is the cross sectional area of the electron bunch in cm^2, $E_{\max} = a_0^2/2\gamma$ [9], and n_e is given in cm^{-3}. Non-linear beam loading was more recently derived by Tzoufras et al. [48,49].

2.4.5 Energy scaling

The maximum energy electron gain, while being accelerated, before slipping into decelerating fields within the wakefield, can be calculated using the definition of work

$$W = \int F(x)\,\mathrm{d}x = -e \int E(x)\mathrm{d}x. \tag{2.32}$$

From eq. (2.11) we know that the peak accelerating field is proportional to ω_p and we will find the maximum energy gain over one dephasing length in the linear regime to scale with $1/\omega_p^2$ or the inverse of the plasma density $1/n_e$.

Assuming electrons are trapped at $x = 0$, we estimate the energy gain over one dephasing length in the linear regime, which can be calculated with

$$\Delta W_{\max} = -e \int_0^{L_d} E(x)\,\mathrm{d}x = -e|E_x|L_d \propto \frac{a_0^2}{n_e}. \tag{2.33}$$

Eq.(2.33) shows that lower plasma densities enable higher energy gain within a dephasing length because $\Delta W_{\max} \propto 1/n_e$. This is beneficial and, hence, much work is put into using plasma waves at low plasma densities to accelerate electrons.

When the intensity of the laser is increased, the ponderomotive force can expel electrons from the centre of the laser propagation axis. For high enough intensities, all electrons are expelled, forming a cavity — in which only ions remain — which trails the laser pulse. This so-called “bubble" regime — often called blow-out regime — was described in 2002 by Pukhov et al. [50] and, in 2007, Lu et al. derived scaling empirically from simulations done for values of $a_0 > 2$ [43]. They considered a laser whose spot has self-focused to w_{sf} and found that it is approximately equal to the blowout radius $R_b \approx \sqrt{a_0}\lambda_p/\pi$. For the energy gain over one dephasing length they find that

$$\Delta W_{\max}^{\mathrm{nl}} = \frac{2}{3}\frac{mc^2}{e} a_0 \frac{\lambda_p^2}{\lambda_0^2}, \tag{2.34}$$

which depends on the plasma density as well as the laser power.

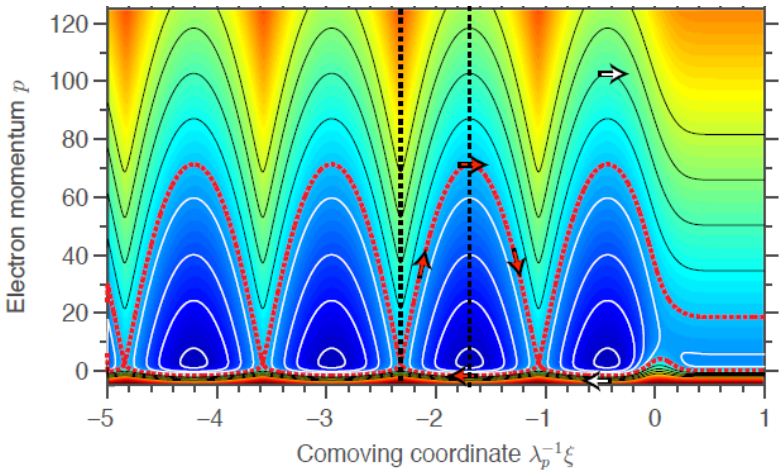

Figure 2.7: Phase-space trajectories of test electrons with different initial energies and their behavior within the fields of the plasma wave. The x-axis can be re-written as the phase in units of π, $(k_0 x - \omega_0 t)/\pi$. The figure was taken from [52].

2.5 Trapping and injection control

So far we have discussed the idea of accelerating electrons in a plasma wave, however we have not discussed the process of how electrons find themselves in the accelerating part of the wave, so-called “trapping". In the linear regime, electrons from the plasma cannot be trapped; however, at higher intensities of the laser pulse, electrons can be injected and accelerated. Early results of quasi mono-energetic beams [14–16], GeV-scale electron beams [17, 18] and the most recently reported electron beams with energies $> 2\,\mathrm{GeV}$ [51] used an injection mechanism called “self-injection". It cannot be easily controlled and spread in energy can be large. Energy spread and the stability of absolute energy and charge can be improved by using methods which control the injection. The idea behind controlled or triggered injection is to decouple the injection mechanism from the acceleration part and control the phase space in which electrons are injected and the amount of charge injected, which usually leads to higher quality beams. In this section, we introduce the mechanism of trapping electrons via a method used for this thesis (§2.5.1), namely self-injection, and several other methods employed by other experiments which have decoupled the injection process from the acceleration process.

2.5.1 Electron trapping and self-injection

The process of electrons remaining in accelerating fields for long enough to be accelerated is called “trapping". It is best described by using the phase-space picture of a plasma wave as shown in Fig. 2.7. It shows the phase-space trajectories of test electrons — which have different initial energies — and their behavior within the fields of the plasma wave. Electrons with an initial velocity smaller than the velocity of the wave (black trajectories) slip back with respect to the plasma wave. Electrons with energies much higher than the wave velocity will overtake the wave. The electrons which propagate with the same phase velocity as the wave are propagating on the so-called separatrix (dotted red line), an orbit which separates untrapped and trapped electrons. Electrons with slightly higher phase velocities

will become trapped and orbit in the phase space (white trajectories). In 2006, Schroeder et al. [53] found that the minimum trapping velocity is dependent on the plasma density and the laser intensity, because the electric field in the wakefield depends on these quantities. For higher laser intensities and higher plasma densities, electrons with lower velocity become trapped: the density dependence can be understood by realizing that for higher plasma density the wave velocity is reduced, and, for higher intensities, the separatrix becomes larger and allows slower electron to become trapped.

For linear plasma waves, electrons in the background plasma cannot become trapped because their initial momentum is too low. However when the plasma wave breaks — a process introduced in §2.2.3 — electrons from the background plasma can gain velocities that exceed the wakefield phase velocity and stay within one plasma bucket. This process cannot be controlled easily, but does allow experiments without a dedicated mechanism for injection to accelerate electrons. The mechanism of injecting electrons via wave-breaking is called self-injection.

2.5.2 Optical injection

Separation of the injection and the acceleration phase can be achieved by using not one but two laser pulses. This second laser pulse — called the injector pulse — is counter-propagating the laser pulse, which creates the plasma wakefield — here called the pump pulse. The injection pulse energy is much less than the pump laser, but when they overlap they form a beat wave with a slow phase velocity. Electrons from the background plasma are accelerated by the force of the beat wave and can reach the injection threshold. When the pump laser intensity is chosen so that wave breaking does not occur, electrons are solely injected at the overlap of the two lasers. By scanning the overlapping point along the pump laser axis the energy can be scanned easily given a certain plasma length. By scanning the length and intensity of the injection pulse, the charge of the beam can be controlled.

In 2006 Faure et al. [26] first demonstrated this approach within a 2 mm short gas jet by accelerating electron beams to energies of 125 MeV with an energy spread of 9 % (Fig. 2.8). Electron beams with energy spread of only 1 % were obtained by the same group in 2009 by Rechatin et al. [54]. A drawback of this counter-propagating method is that the counter propagating injector pulse can propagate through the pump pulse laser system and destroy parts of it.

2.5.3 Density transitions

In 1998, Bulanov et al. [55] suggested using plasma density gradients with density decreasing in the laser direction to control injection, so-called density “down ramps". The decreasing density of the plasma will increase the plasma wavelength along the laser propagation direction and the wake front trailing the laser will slow down. The decreasing phase velocity of the wake front lowers the minimum velocity the electrons need to reach before they can be trapped.

The first mono-energetic beams achieved with this technique were presented by Geddes et al. [56] in 2008. In this paper, the authors presented electrons of energies < 1 MeV.

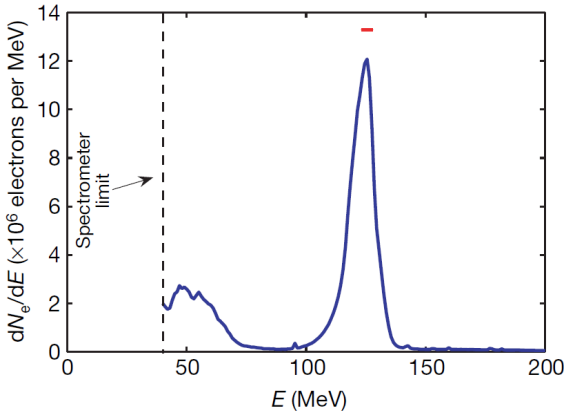

Figure 2.8: A quasi mono-energetic electron spectrum obtained by colliding pulse injection. The peak energy is 125 MeV and the energy spread is 9 %. This figure was taken from [26].

To realize the density ramp, the laser was focused at the decreasing density edge of the gas jet rather then at the middle part in which a constant density is present. Because the acceleration length was small, and hence the energy gained by the electrons was low, the authors suggested using the technique in combination with a secondary plasma stage for acceleration. The injection mechanism was therefore decoupled from the acceleration part. Coupling a density down-ramp to an accelerating stage was realized by the same group in 2011 by Gonsalves et al. [57]. The authors positioned the gas jet inside and at the beginning of the capillary discharge waveguide previously used in the 2006 experiments which achieved an 1 GeV beam with 2.5 % energy spread [17]. Gonsalves et al. used a 40 TW laser system to accelerate electron consistently to 400 MeV with only a few percent energy spread. By adjusting the density or the position of laser focus they could scan the energy of the electrons between 100 and 400 MeV.

In 2010 Schmid et al. [58] used a sharp density transition produced by a shock front inside a gas jet to inject and accelerate electrons to energies between 15 to 25 MeV with charges of 3.3 pC. The authors show that the energy spread and divergence is slightly reduced when using the shock front.

2.5.4 Ionisation-induced injection

Another idea to inject electrons, only recently employed by experiments, was proposed by Umstadter et al. [12] in 1996. So-called ionisation-induced injection uses the difference in ionisation potential within an atom/molecule or between different species of atoms/molecules to ionise electrons at the right phase within the wakefield. To understand the method, we consider a short and intense laser pulse propagating through a gas. The gas is comprised of a low-Z gas e.g. hydrogen and a small amount of high-Z gas e.g. nitrogen. The front part of the laser pulse will fully ionise the hydrogen molecules and the outer shell electrons of the nitrogen. These electrons form the wakefield. For well-chosen parameters of plasma density and laser intensity, electrons will not be injected. However, electrons still bound by the nitrogen core can be ionised at the peak of the laser pulse, and are placed within the accelerating field of the wake. These electrons are ionised at rest — i.e. "born" — and come from the inner shells of the nitrogen molecule. The theory of ionisation-induced injection

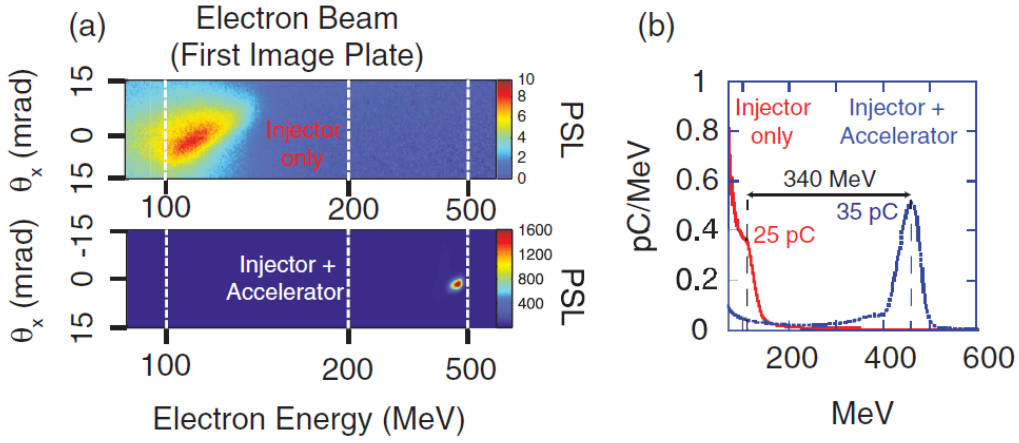

Figure 2.9: Electron spectra from ionisation induced injection experiment. (a) Electron beam spectra from injector-only gas cell (top) and two-stage cell (bottom). (b) Electron spectra from two-stage injector-accelerator cell (blue curve) and the injector-only cell (red curve). This figure was taken from [25].

was recently summarized and modeled in [59].

First experimental evidence of this process in LWFA was published by Rowlands-Rees et al. [60] in 2008. In 2010, Pak et al. [27] and McGuffey et al. [61] used this technique specifically to accelerate electrons. However the energy spread was large in these early experiments due to the fact that electrons born on-axis experience a greater change in the wake potential than those born off-axis and also due to the continuous injection of electrons while the laser propagates through the gas mix. Clayton et al. [62] used this method in late 2010 to achieve a maximum energy of 1.45 GeV; however, as in the previous experiments, the energy spread was large.

To avoid the continuous process of injection, two groups employed accelerators with two stages; the first stage works as an injector and within the second stage, the electrons are accelerated. In 2011, Pollock et al. [25] used a gas cell filled with helium gas and an impurity of high-Z gas to inject electrons (Fig. 2.9). Once injected, the electrons traversed into a second plasma without impurities and accelerated to ≈ 500 MeV with 5 % energy spread. A similar set-up was used by Liu et al. [24] to accelerate electrons to 800 MeV with 25 % energy spread.

2.6 Guiding intense laser pulses with waveguides

The need for guiding laser pulses was illustrated in §2.4.1, where Rayleigh diffraction was introduced. In Fig. 2.10 the laser spot size as a function of propagation distance is shown and it can be seen that without guiding the laser spot increases rapidly. While self-focusing can achieve guiding over many Rayleigh lengths, the power requirements for the driving laser pulse are higher than when using external guiding structures as explained in §2.3.3. In addition, channels enable guiding for low to moderate values of a_0, where self-guiding is not possible, as described by Tzoufras et al. [63]. For such values of a_0 the efficiency of the accelerator is much higher, and therefore, channel guiding has been employed by many

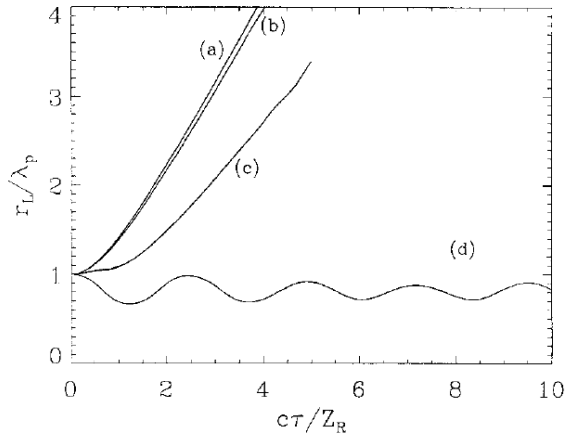

Figure 2.10: Simulations for a laser spot size as a function of propagation distance $c\tau$ for (a) vacuum diffraction, (b) a pulse with $c\tau = \lambda_p/4$, and (c) a pulse with $c\tau = \lambda_p$. The simulation assumes the laser power being equal to the critical power $P = P_c$, and $a_0 = 0.9$, with $\lambda_p = 0.3 \times 10^{-3}$ m. (d) The laser pulse from (c) is shown guided in a preformed, parabolic plasma density channel. The figure was taken from [40].

groups.

This section will introduce several techniques to guide laser pulses — a detailed overview of waveguides can be found in [64] — before introducing the capillary discharge waveguide in §2.6.3, which was first used for LWFA experiments by Professor Simon Hooker and Dr. Anthony Gonsalves in 2006 [17]. Improvements to this original design are discussed in chapter 4.

2.6.1 Step refractive index guiding

A cylindrical waveguide, in which the core material has a refractive index η_{core} larger than the index of refraction of the wall η_{wall}, can guide laser pulses over many Rayleigh lengths. Guiding happens via total internal reflection at the walls. However, in LWFA experiments the core must comprise gas or plasma, for which $\eta \approx 1$. Suitable materials with $\eta < 1$ do not exist to form a guiding structure, although guiding can be achieved in hollow-core capillaries, as first discussed in 1999 by Dorchies et al. [65]. The laser pulse ionises the gas and the refractive index of the plasma becomes $\eta_{plasma} < 1$. For the capillary tubes usually used in LWFA, total internal reflection is not possible under these circumstances. However, choosing to minimize the angle of reflection, guiding can be achieved via grazing incidence guiding.

Benefits of these capillary tubes are, that they can guide very small laser spot sizes over many Rayleigh lengths, and that the guiding structure is independent of the plasma present since guiding structure and plasma formation are uncoupled. However, since the hollow core tubes guide by reflection from the capillary walls a drawback is that damage to the wall can occur by the interaction of the wings of the laser pulse. For laser pulses used in LWFA, the intensity is peaked on axis and decreases towards the wall, which minimizes this damage.

In the paper by Dorchies et al. [65], laser pulses with intensities of $10^{16}\,\mathrm{W/cm^2}$ were guided in capillary tubes of 100 mm length. A subsequent publication in 2002 by Cros et al. [66] calculated the Eigenmodes of capillary tubes. The amplitude of the plasma waves driven in hollow capillaries was measured by the same group in 2009 by Wojda et al. [30] by measuring the wavelength shift and comparing it to theoretical calculation by Andreev et al. [67]. This experiment achieved laser transmission of up to 90 % over 80 mm with laser pulses of $10^{18}\,\mathrm{W/cm^2}$.

In 2011, the capillary tubes were used [20,68] to accelerate electron beams with energies of 170 MeV. The waveguides used had diameters between 150 and 250 μm and lengths of 6-20 mm. In this paper, the authors also employed betatron radiation, from the electron beams, as diagnostic of electron injection.

2.6.2 Gradient index guiding

An electron density profile with minimum on axis can counteract diffraction and guide laser pulses. This is utilized in a plasma channel, where the radial profile of the plasma channel is of parabolic form and the laser beam stays Gaussian during propagation. The phase velocity will increase with distance from the axis, causing the wavefronts to bend towards the axis. The difference in plasma density between the bottom of the channel and at position r_{ch} can be expressed as [69]

$$\Delta n_{\mathrm{e}} = \frac{1}{\pi r_{\mathrm{e}} r_{\mathrm{ch}}^2} \tag{2.35}$$

where r_{e} is the classical electron radius. If the laser spot w_0 is equal to the matched spot of the channel, given by [40]

$$W_{\mathrm{M}} = \left(\frac{r_{\mathrm{ch}}^2}{\pi r_{\mathrm{e}} \Delta n_{\mathrm{e}}} \right)^{\frac{1}{4}}, \tag{2.36}$$

the laser propagates through the channel without oscillations. If $w_0 \neq W_{\mathrm{M}}$ a oscillatory motion can be found [64], in which the size of the spot oscillates according to

$$w_0^2(x) = \frac{w_0^2}{2} + \frac{W_{\mathrm{M}}^4}{2w_0^2} + \left(\frac{w_0^2}{2} - \frac{W_{\mathrm{M}}^4}{2w_0^2} \right) \cos\left(\frac{2\lambda_0 x}{\pi W_{\mathrm{M}}^2} \right). \tag{2.37}$$

However, an unmatched laser spot can still be guided through the plasma channel. Plasma channels of this type have been generated by several methods, some of which are discussed below.

Laser produced plasma channels

Early methods of laser produced plasma channels were suggested by Durfee et al. [70] in 1995 and Volfbeyn et al. [71] in 1999. The ignitor-heater technique from [71] was used in 2004 by Geddes et al. [16] to create quasi-mono-energetic energy beams (Fig. 2.11). The technique works on the principle of using more than one laser pulse to decouple the process of plasma formation and plasma heating which forms the channel. A short intense laser pulse is used to ionise the gas, while the heating pulse is much longer and lower in intensity but higher in energy. The plasma heats through the process of inverse bremsstrahlung

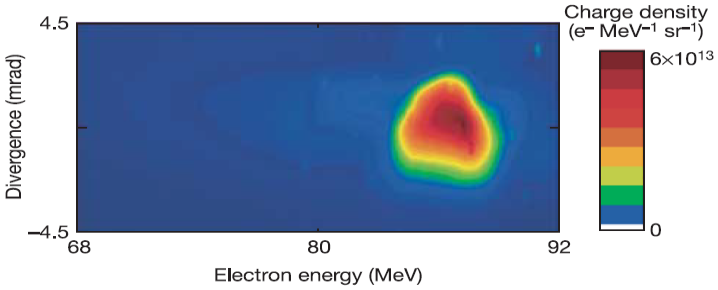

Figure 2.11: Single-shot electron beam spectrum and divergence. The electrons were accelerated to 86 MeV with a divergence of 3 mrad. The figure was taken from [16].

absorption. This causes a fast hydrodynamic expansion of the plasma into the surrounding and unheated and hence cold region, which in turn drives a shock wave. After an appropriate delay, typically a few nanoseconds, the electron density is minimal on axis and forms the ideal waveguide profile for the third laser pulse which drives the wakefield and enables acceleration.

The gas-based guiding ensures destruction free guiding because every shot a new waveguide is being created by the plasma. While the technique works well in gas-jets with densities of $10^{19}\,\mathrm{cm}^{-3}$, the heater pulse does not transfer enough energy to the plasma at densities of $10^{18}\,\mathrm{cm}^{-3}$ in a time short compared to the plasma expansion. The channel is also not only limited by the length of the gas jet, but also by the expansion of the higher density region away from the axis which forms the walls of the channel; while they are expanding with time, and hence provide a time dependent matched spot size of the channel, they are also of finite density and radiation leaks through them. Available laser power to heat the plasma also limits the channel length.

Discharge ablated capillaries

The method using the discharge ablated capillary, pulses a current of roughly 200 A and 500 ns through a capillary via an electrical discharge. The plasma source is material from the walls of the capillary, which slowly erodes. Heat flows to the capillary wall, leading to a temperature profile which is peaked on axis. Since pressure differences are minimal transversely, the density profile has a minimum on axis, and this capillary can be used to guide laser pulses. The advantages are that the set-up is relatively simple for no gas needs to be supplied as plasma source. However usually a capillary lasts for roughly 10^3 shots before having to be replaced. Another problem is that the plasma is partially ionised — an intense laser pulse then leads to further ionisation and hence defocusing [72]. In 2002 Zigler et al. [73] showed guiding of laser pulses using this technique. But it was an experiment by Kameshima et al. [74] in 2008 which demonstrated electron acceleration in an ablated discharge capillary for the first time. Here a laser pulse of 4 J with a pulse length of 26 fs was used to accelerate electrons to above 0.5 GeV with charges of about 10 fC.

Fast discharge gas cell

A new approach to guiding a laser pulse via a channel was introduced by Bendoyro et al. in 2008 [75]. Their structured gas cell produced the plasma via an electric discharge between two hollow conic electrodes. The plasma channel was kept straight by introducing dielectric plates along the discharge path. The ionised plasma cylinder created then expands almost freely and creates a radial parabolic density profile. This again creates the density profile with minimum on axis for high intensity laser guiding. The “fast" in the name of the technique refers to the fact that the current pulse is short compared to the plasma expansion time, and hence it is related to the hydrodynamic expansion channel introduced in 1995 [70]. Initial results show that this device can guide a low intensity laser pulse over almost 17 mm with nearly 100 % energy transmission. The possibility of creating longitudinal variation of plasma density is one of the advantages of the device. These are implemented by changing the fill pressure of individual cells. The device has recently been used at the Astra-Gemini laser facility. The group lead by N. Lopez presented electron beams with energies of 400-700 MeV from a 40 mm gas cell and evidence of energy gains up to 2 GeV were observed [51].

2.6.3 Capillary discharge waveguide

The capillary discharge waveguide used in experiments described in chapters 5 and 6 is introduced. It belongs to the waveguides which use gradient index guiding. Here, previous work is reviewed and the process by which it produces the plasma channel is described. In chapter 4 improvement to its electrical circuit and housing are described in detail.

Previous work

The hydrogen-filled capillary discharge waveguide was originally developed by Professor Simon Hooker, Dr. David Spence [76] and Dr. Arthur Butler [77]. With the Astra laser of the Rutherford Appleton Laboratory (RAL), Butler et al. proved the viability of the capillary to guide fs-short high-intensity laser pulses with high energy transmission [78]. Later work, in collaboration with Professor Wim Leemans’ group at Lawrence Berkeley National Laboratory (LBNL), used this waveguide to extend the acceleration length of a laser-driven plasma accelerator and thereby generated an 1 GeV electron beam for the first time [17, 18]. This experiment was performed using a laser pulse of 1.4 J energy and a 33 mm short waveguide. In 2007, Gonsalves et al. [79] furthered the understanding of the plasma channel by publishing scaling laws of the axial plasma electron density and the matched spot size of the plasma channel deduced from interferometric measurements of the channel.

In 2008, Rowlands-Rees et al. [60] performed an acceleration experiment at RAL with laser pulses of 0.6 J which demonstrated that the injection of electrons is very sensitive to the delay between the onset of the discharge and the arrival of the laser pulse. Using interferometric measurements, this publication suggested that injection of electrons is helped by laser-ionisation of unionised molecules in the plasma. Another experiment was performed using the newly built Astra-Gemini laser at RAL in 2010 and Fig. 2.12 (b) and Fig. 2.12 (f) show the result of an electron beam with an energy above 500 MeV. Ibbotson et al. [1, 2]

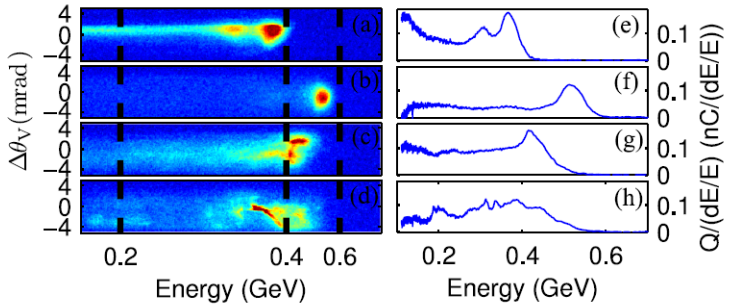

Figure 2.12: Raw electron energy spectra (left column) and the spectra in units of charge per relative energy spread (right column). The figure was taken from [1].

showed that injection depends strongly on the quality of the laser focal spot. By improving the quality of the laser focal spot, the authors found that the threshold for laser energy required to produce electron beams can be reduced.

Plasma channel formation

The process of plasma channel formation was discussed in 1996 by Zigler et al. [80]. They argue that during the discharge the pressure is constant across the capillary since the time taken for an acoustic wave to cross the capillary is short compared to the time over which the current changes. The discharge increases the temperature of the plasma by ohmic heating but heat is lost to the capillary walls. This establishes a temperature profile inside the capillary which is peaked on axis. Because the pressure is constant across the capillary the density profile has a minimum on axis and forms an ideal profile to guide laser pulses.

In 2001, Bobrova et al. [81] simulated the hydrogen-filled capillary discharge waveguide which confirmed Zigler's model. The simulations show that the discharge progresses in several steps: (i) initially the 300 A, 200 ns short discharge ionises the hydrogen molecules, which raises the plasma density uniformly across the capillary and lasts for 30 ns; (ii) the ions are cooled by the wall of the capillary; (iii) the cooled ions reduce the temperature of the electrons around the walls and the temperature and thus plasma density profile is formed over roughly the next 30 - 60 ns. They further found that because the ionisation level of the plasma is lower close to the walls, the conductivity of the capillary is higher on axis. This leads to a higher current level in the centre of the capillary – and to higher temperatures on the axis — which in turn deepens the parabolic plasma density profile needed for guiding. Later simulations by Broks et al. [82] confirmed the main features of this model, and were also used to reproduce interferometrically measured transverse electron density profiles [79].

Chapter 3

Charge calibration experiment

From the middle until the end of March 2009, an experiment was conducted at the DAFNE beam test facility (BTF) in Frascati, Italy. The aim of this experiment was to calibrate two kind of detectors, image plates and scintillating screens, which are often used in LWFA experiments. In §3.1, a motivation for why these calibrations were needed is given with a discussion of the previously accepted calibration and a calculation of the energy deposition for the image plate. The facility infrastructure and detectors are presented in §3.2, and in §3.3 the methods used to analyse both image plate data and scintillating screen data are presented and results and discussion are documented in §3.4. The conclusion are given in §3.5.

3.1 Motivation

Beam charge is one key parameter of any accelerated and charged beam. Charge measurement can be done with various techniques, e.g. using an integrating current transformer (ICT), a previously calibrated light source, or an image plate (IP). ICTs have been used from the beginning of LWFA experiments. However, the uncertainty connected with their ability to measure femtosecond short electron bunches remained and several groups have tried to move towards other techniques.

One way to avoid ICTs is the combination of two detectors: image plates with scintillating screens. While image plates are frequently used to measure the charge of electron beams at low energy, with energies below 1 MeV, their calibration for higher energetic beams, with energies of above 1 MeV, is not well studied, and simulations are used to predict their behaviour. This is further discussed in §3.1.1. Scintillating screens are inexpensive, flexible screens and their response is known and linear for low bunch charge. However, prior to the experimental work reported in this chapter, it was only assumed that the response remained linear at high bunch charges present in LWFA experiments.

Given the importance of knowing the bunch charge, and the three uncertainties in determining this quantity at the time — (i) ICT might not work for femtosecond bunches, (ii) IP charge calibration for electrons is simulated, and (iii) the linearity of scintillating screens is only assumed — it was decided to undertake a direct calibration of the response of scintillating screens and IPs by comparing their responses to bunches of known charge

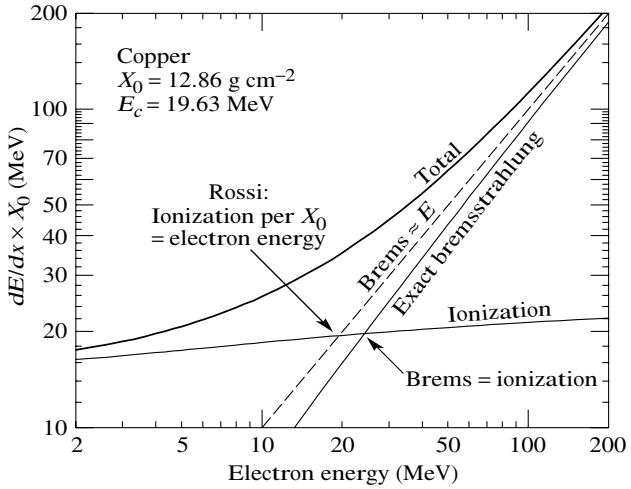

Figure 3.1: Plot of $X_0\,\mathrm{d}E/\mathrm{d}x$ as a function of electron energy, where X_0 is radiation length, which is defined as the mean distance over which a high-energy electron loses all but 1/e of its energy by bremsstrahlung, and $\mathrm{d}E$ is the energy loss over a distance $\mathrm{d}x$. This graph was taken from [85].

from a radio-frequency accelerator. The experiment that is the subject of this chapter is the first experimental calibration for image plates that are exposed to electrons with energies in the order of 500 MeV. It yields a value for the number of electrons per photo-stimulated luminescence (PSL[1]), recorded by a calibrated image plate reader. The image plates studied here are BAS-MS image plates from FUJIFILM which are reasonably cheap, flexible, and readily available. Scintillating screens are sometimes called phosphor screens and often just “Lanex" screens, after an early brand name. The results presented in this chapter comprise the first experimental study reported of the response of Lanex Regular screens from Kodak for a typical range of charge densities presently achieved in LWFA experiments with a single electron beam with energy of 500 MeV.

In work published shortly after our experiment, Buck et al. [83] and Zeil et al. [84] confirmed the results and introduced a clever way of calibrating the optical set-up using a calibrated radio-active source[2]. Work by K. Nakamura [18] from LBNL confirmed the linearity of another scintillating screen, Lanex Fine screens, up to a certain saturation point. The studies of Buck et al. and Zeil et al. will be discussed in detail in the conclusion section of the chapter.

3.1.1 Discussion of previously accepted calibration value

In the following paragraphs, we discuss the value accepted for image plate calibrations prior to the experimental work presented in this chapter. It discusses the way that Mangles [86] used the information from an x-ray experiment performed by Gales et al. [87] to simulate the response of electrons to image plates.

[1]PSL is not only the name of the physical process but also the unit in which the image plate reader records data. A detailed discussion of the process can be found in §3.3.

[2]Such a source was used during the Astra-Gemini experiment. However, it broke and leaked radiation, which unfortunately lead to the shut-down of the experiment for several months.

From Gales et al. [87] and Mangles [86] we know that an IP measurement of 0.02 PSL corresponds to an energy deposition of 50 keV inside the image plate. This energy deposition was recorded in a BaF(Br,I) Europium doped image plate. For these experiments, Gales et al. used x-rays and the BAS IP-IIIS image plate. The read-out was produced by an image plate scanner of model FUJI BAS 2500 with 50 μm resolution. While the BAS IP-IIIS image plate as well as the BAS IP-MS (used in our experiments and in Stuart Mangles' experiment) are made of $BaFBr_{0.85}I_{0.15}$, the phosphor density in BAS IP-IIIS is 4.1 % lower. In addition to this first discrepancy between the two image plates, the active layer of BAS IP-IIIS is 20.8 % thicker. The manufacturer's information shows that the BAS IP-MS can have a 5 – 10 % increased sensitivity to x-rays at low energy compared to BAS IP-IIIS. The relative response to electrons of the IP has never been tested experimentally..

Mangles [86] used the information from Gales et al. [87] and the Monte-Carlo method [88] code MCNP, which considers the loss and deposition of energy into the material caused by collisions and radiative processes [86], to simulate the response of the BAS IP-MS image plate to electrons. He found that one electron passing through the image plate with energies between 1 MeV and 100 MeV deposits 50 keV independent of its energy. The equal energy deposition, independent of the electrons energy, was surprising to the author at first, because it is well known [85] that the energy loss of electrons in material is strongly dependent on energy in this energy range. This can be seen in Fig. 3.1 where the energy loss of electrons passing through material is shown. A brief discussion of why the simulation shows a flat energy loss distribution is given in the next paragraph.

The following argument may help to explain why this occurred: electrons with energies more than 20 MeV predominantly lose energy by bremsstrahlung. The so-called radiation length X_0 is the mean distance over which a high-energy electron loses all but 1/e of its energy by bremsstrahlung. Radiation length distances are several centimetres in length whereas image plates are only hundreds of micrometres thick. In passing through an IP, an electron loses only a small fraction of its energy. In addition, bremsstrahlung photons can escape from the image plate without depositing a significant fraction of their energy in the IP. The bremsstrahlung photons that do deposit their energy are the photons created in the first layers of the image plate. These are created in equal amounts by low and high energetic electrons and hence the energy deposited in the image plate by low and high energetic electrons is the same.

The reasons for the independence of the energy deposited in the IP on the incident electron energy found in Mangles' simulations can therefore be understood. The simulations performed by Mangles were done for electrons with energies ranging from 1 MeV to 100 MeV. Following the argument just presented, it can be assumed that the same energy (50 keV) is deposited inside the image plate by electrons with energies of above 100 MeV.

In summary, Gales et al. [87] showed that 50 keV of deposited x-ray energy leads to a value of 0.02 PSL and Mangles [86] assumed that this was true for electrons. This led to the previously accepted calibration value of 0.02 PSL per electron. However, two statements from Mangles work have not been tested: first, do electrons above 1 MeV really deposit 50 keV of their energy while passing through the image plate and, secondly, is the assumption correct that an electron losing 50 keV create a PSL value of 0.02 PSL just as 50 keV energy loss of x-rays create a value of 0.02 PSL. The uncertainty on the previously accepted calibration value simulated by Mangles is one of the reasons why the experiment discussed in this chapter was performed.

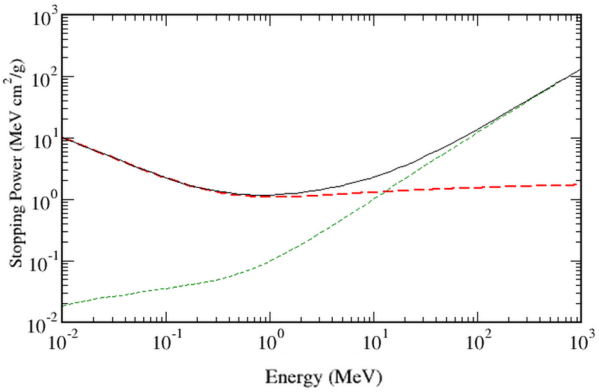

Figure 3.2: Stopping power of electrons in Europium as a function of electron energy. The radiative stopping power is indicated by a dashed, green line, the collisional stopping power by a dashed, red line, and the total stopping power by a solid, black line. This figure was produced using ESTAR provided by the National Institute for Standards in Technology [89].

3.1.2 Calculation of energy deposition

The energy amount lost by an electron passing a detector is dependent on the initial energy of the electron and the material of the detector. Since the company FUJI does not provide details of the exact composition of the image plate, the energy deposition calculation as a function of electron beam energy presented here can only make an upper estimate of the true value. The only statement from the company regarding the amount of Europium inside the image plate was, that it was below 5 %. For simplicity purposes, we will only consider the active material of the image plate, Europium, in which most energy is lost, and neglect the support material.

To calculate the energy lost by one electron as a function of its energy, data from ESTAR, provided by the National Institute for Standards in Technology [89], is used. In Fig. 3.2, the stopping power, defined as the average rate of energy loss per unit path length, is shown for an electron passing through the active material Europium. It can be seen that, for electrons above 100 MeV, the total stopping power is basically equal to the radiative stopping power. Using the data from ESTAR — with the energy loss per unit length in Europium for an electron with an energy of 500 MeV being $\frac{\mathrm{d}E}{\mathrm{d}x} = 67\,\mathrm{MeV\,cm^2/g} \times 32\,\mathrm{g/cm^2} = 2.14 \cdot 10^3\,\mathrm{MeV}$ [89] — the energy loss ΔE can be estimated to be

$$\begin{aligned}\Delta E &= \frac{\mathrm{d}E}{\mathrm{d}x} \times L_{screen} \times p_{IP}^{FUJI} \\ &= 2.14 \cdot 10^3\,\mathrm{MeV} \times 500\,\mu\mathrm{m} \times p_{IP}^{FUJI} \\ &= 1.07\,\mathrm{MeV} \times p_{IP}^{FUJI}, \end{aligned} \tag{3.1}$$

where $L_{screen} = 500\,\mu\mathrm{m}$ is the thickness of the image plate, and p_{IP}^{FUJI} is the unknown factor to correct for the fact, that the image plate does not consist of 100 % Europium atoms. Since the company FUJI does not provide details of the exact composition of the image plate, the energy deposition can only be estimated to be below the value calculated in (3.1) and

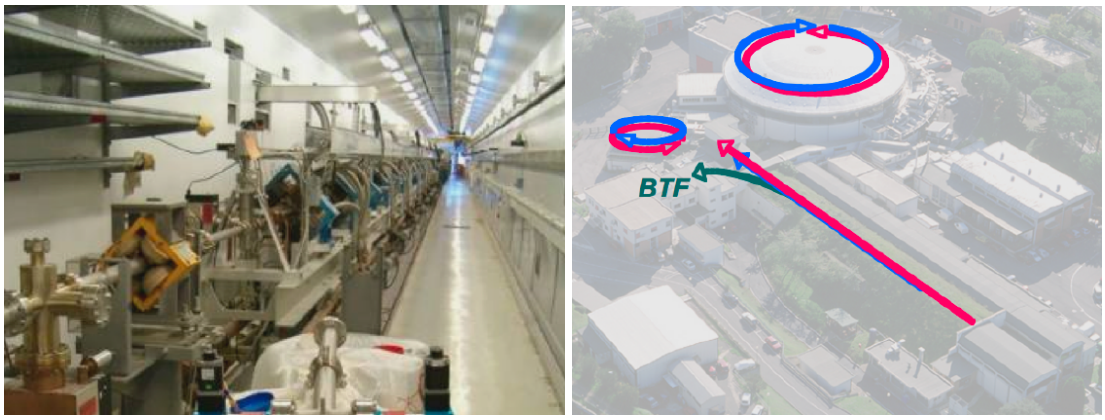

(a) (b)

Figure 3.3: The DAFNE linear accelerator (a) and an aerial view over the two storage rings and BTF (b) [90]. The paths of electrons and positrons are illustrated by red and blue lines respectively.

becomes

$$\begin{aligned} \Delta E &= 1.07\,\text{MeV} \times p_{IP}^{FUJI} \\ &< 1.07\,\text{MeV} \times 0.05 \\ &< 53.6\,\text{keV}, \end{aligned} \tag{3.2}$$

in which the estimate, given to us by the company of 5 %, was used. While the value for the energy deposition of 53.6 keV is very close to the value of 50 keV, used in Gales et al. [87] and Mangles [86], it is not satisfactory for the calibration of charge in electron experiments to know only the upper limit and hence several groups — among them ours — have performed calibration experiments to eliminate this uncertainty. This chapter discusses the calibration experiment performed by our group.

3.2 Experimental set-up and detectors

3.2.1 DAFNE and BTF facilities

The DAFNE [3] accelerator facility is an electron-positron collider mainly dedicated to the study of Charge Parity (CP) violation and K-Meson properties [90]. It creates $\phi(1020)$ mesons by annihilating electrons and positrons in a storage ring at their resonance of m = 1.02 GeV. Electrons and positrons are accelerated in a linear accelerator (Fig. 3.3 (a)) and steered into the smaller of two storage rings (Fig. 3.3 (b)). After being stored and accelerated further, the particles are fed into the collider ring where they collide head on for about twenty minutes. During these twenty minutes, in which the storage ring is not filled, the accelerator can steer the electrons into a beam test facility (BTF). The BTF is an electron beam transfer line which leads into an experimental hall. Its primary purpose is to perform detector calibrations. Fig. 3.4 shows the BTF transfer line and a schematic view of the experimental hall (left top).

[3] DAFNE is often spelled DAϕNE in literature to hint that the experiment produces ϕ mesons.

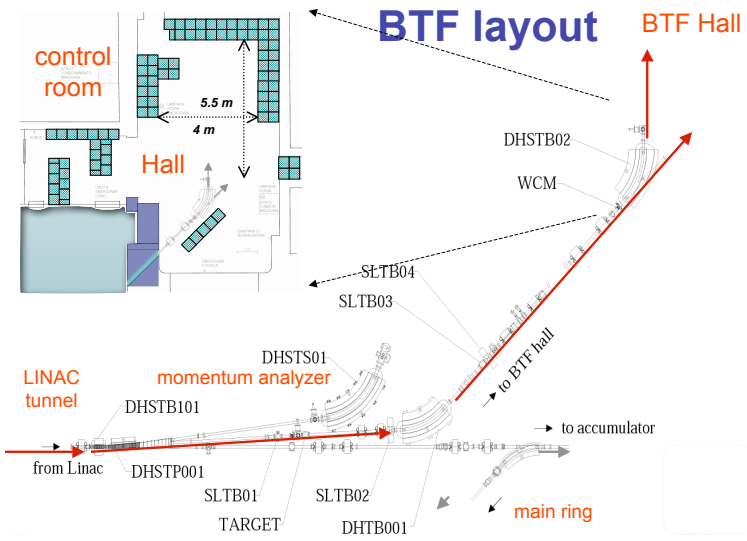

Figure 3.4: The figure shows the BTF transfer line and a schematic view of the experimental hall (left top) [90].

3.2.2 Electron beam properties

The properties of the electron beam used in the BTF are summarized in Table 3.1. Changing the energy of the beam was not possible during the duration of the entire experiment, because it would have required changing the magnet settings in the whole accelerator and would have disrupted the main DAFNE experiment. The magnet settings determine the cross-section of the electron beam and, since only marginal changes were performed on the magnet settings, the area of the beam did not change significantly during the entire experiment.

The bunch charge was changed by the operator at the main DAFNE accelerator by changing the current flowing through the tungsten wire at the start of the accelerator. At the end of the BTF transfer line an integrating current transformer coil was placed around the vacuum pipe to measure the charge of the beam arriving in the BTF. The ICT is described in §3.2.4 and was the only method used to measure the charge of the electron beam.

Electron Beam Properties	
energy	$(505 \pm 5)\,\mathrm{MeV}$
charge	$(10 - 1000)\,\mathrm{pC}$
beam cross-section area	$50 \times 10^{-6}\,\mathrm{m}^2$
beam radius	$4 \times 10^{-3}\,\mathrm{m}$
pulse length	10 ns
shot repetition rate	30 s (IP), 5 s (Lanex)

Table 3.1: Properties of the electron beam during the experiment. The electron beam was provided by the DAFNE facility and properties other then the charge and the repetition rate could not be changed.

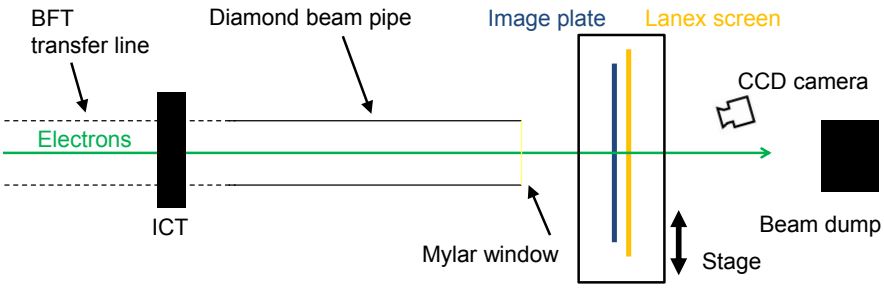

Figure 3.5: Schematic layout of the experiment.

3.2.3 Experimental layout

Fig. 3.5 shows the arrangement of the experiment. The BTF transfer line was connected to a 2.5 m long beam pipe, the Diamond beam pipe[4]. At the end of the Diamond beam pipe the electrons exited the 10 mbar vacuum through a 500 μm thick Mylar window. The image plate was placed 202 mm behind the Mylar window. The Lanex screen was positioned 3 mm beyond the image plate with the photon emitting side facing the camera. The image plate and Lanex screen were both attached to a magnetic stainless steel holder by magnetic strips. The holder was designed to allow for flexible and quick removal and attachment of exposed and new image plates and Lanex screens. Since each region of the image plate could only be exposed once, the holder was designed to be attached to a slide which moved the image plate (and Lanex screen) by 70 mm after each shot so that an unexposed area of the image plate was facing the next beam. A CCD camera was placed 675 mm away from the Lanex screen with an angle of 10° to the electron beam trajectory.

3.2.4 Integrating current transformer

The electron charge was measured with an integrating current transformer (ICT) made by Bergoz [91]. ICTs have a magnetic core which is made from thin ribbons of cobalt and molybdenum alloy interleaved with nickel and iron crystalline alloy. Electrons passing through the ICT induce a current in the magnetic core and the current is proportional to the charge passing through the ICT. By integrating the trace $I(t)$ and dividing it by the calibration factor F, the charge of the electron bunch can be calculated

$$Q = \frac{1}{F}\int I(t)dt. \tag{3.3}$$

3.2.5 Image plate and image plate reader

Image plates are two dimensional detectors widely used for x-ray detection and charge determination of low energy electrons. They consist of several layers: the supporting layer

[4]The beam pipe, which was made for and was used at the Diamond synchrotron facility after this experiment, is a vacuum pipe which had the ability to insert pepper pots and transition radiation detectors. During the IP and Lanex detector runs all other detectors inside the Diamond beam pipe were removed and the electrons traversed it undisturbed.

(500 μm), the active layer (100 μm) and a protective layer (10 μm). The active layer is made of photostimulable phosphor. In this experiment, the image plates used were BAS IP-MS from FUJI [92], which uses barium fluoro-halogenite bromine doped with europium ions ($BaFBr:Eu^{2+}$).

When electrons pass through the active layer, they ionise Eu^{2+} to Eu^{3+}. The electrons, created by ionisation, are trapped in lattice defects created by the absence of the halogen Br. When the trapped electrons fall into a lower lying state, photons are emitted and it is this photon signal which is detected. In the absence of saturation, the phosphorescence is proportional to the number of electrons passing the image plate.

These lattice defects are called F centres or colour centres.[5] Due to quantum mechanical exclusion rules these excited states can not decay into lower states and can live for days. However, 30 – 50 % of these so-called metastable states decay within hours due to thermally induced, spontaneous recombination of the trapped electrons with the Eu^{3+} ions. This process is referred to as “fading". It is therefore important to know the decay characteristic of the fading process and to correct for it. The rate of fading depends on and increases with temperature and this parameter was monitored during the data taking. The average temperature of the experimental hall was 19.3 °C and the average temperature in the room of the reader was 18.3 °C. The degree of fading does not, however, depend on the exposure level and corrections can be made independently of the energy and number of electrons deposited in the image plate.

Reading out the image plate is performed by placing it inside an image plate reader. Within this a laser is scanned over the whole image plate which photo-excites the trapped electrons into the conduction band and allows de-excitation under emission of a 390 nm photon. This process is called photo stimulated luminescence and the blue photons are detected with a photo multiplier.

The image plate reader used during the experiment was a Fuji BAS 5000. Since the IP scanner digitizes the plate readout using a logarithmic amplifier, the measured pixel data have to be converted between the output of the image plate reader (in units of quantum level, QL) to a linear PSL scale. This process is described in §3.3.2. The readout process removes 60-90 % of the excited states. The residual signal on the image plate was then erased by placing the image plate below a white light source for at least ten minutes. De-exciting all remaining excited states allows the image plate to be reused.

After exposure to the electron beam, the plates were transported from the experimental hall to the image plate reader. In order to shield the image plates from room and sunlight, the image plates were wrapped in 11 μm thin aluminum foil. Before placing the plate inside the image plate reader the aluminum foil was removed in a dark environment.

3.2.6 Lanex screen and CCD camera

Lanex screens produced by Kodak (and after the bankruptcy of Eastman Kodak now provided by a company called Henry Schein) are fluorescent screens used mainly for x-ray imag-

[5] Colour centres are regions of normally transparent material that became damaged on the atomic level, so that negative ion places are filled by electrons. These sites then absorb light, appearing coloured instead of transparent. [93]

ing applications and commercially available from dentist suppliers. Like the image plates, they consist of three layers: a supporting layer, an active layer and a protective layer. The active layer in the Lanex screen used in this experiment (Lanex Regular) is made of scintillating phosphor ($Gd_2O_2S:Tb$). Electrons passing through this layer excite electrons in the phosphor to states with lifetimes of less than a microsecond, which radiate photons of 545 nm wavelength. The number of photons emitted is proportional to the energy deposited in the active layer of the screen. The photons are detected by a CCD camera and stored as an image file on a personal compueter. The camera used was a monochrome Flea2 CCD camera produced by GREYPOINT (FL2-20S4C-C) and no gain was needed. Fluorescence from the Lanex screen was reflected by a plane mirror and imaged by a manually operated zoom lens system onto the CCD camera. A trigger from the main DAFNE linear accelerator, indicating the arrival of an electron beam, was used to trigger the camera via a program written in LABVIEW. This program labeled and saved the data in TIFF images.

During the experiment all room lights were switched off and the windows were blackened. Light from blinking electronic equipment inside the experimental hall was shielded by four layers of black plastic sheets. Background shots had an average pixel count of 3.7 whereas beams with the lowest charge produced peak pixel counts of above 230.

3.3 Methods of analysis

This section describes the methods of analysis and is divided in three sections. The analysis methods for the integrating current transformer data are presented in §3.3.1. §3.3.2 presents the methods used to analyse the image plate data as well as the decay constant result, and the methods used to analyse the scintillating screen data are discussed in §3.3.3 which includes a detailed account of the screens absolute calibration.

3.3.1 ICT data

The oscilloscope integrated the current trace and presented a result for the integral. After the experiment, however, it was found that this integral was not reliable, because it integrated over noise and background, and hence the value output by the oscilloscope for the integrated current was not used. Unfortunately the raw data from the oscilloscope were not recorded during the experiment; only colour images of the oscilloscope screen of each shot were saved. In order to gain information about the charge and replace the dependence on the oscilloscope result, a MATLAB routine was written to analyse the images. The following paragraphs describe this routine.

A typical oscilloscope image is shown in Fig. 3.6. Three ICT signal traces and one trigger trace can be seen. The blue trace is the current trace from the ICT positioned closest to the experiment and was the one we used to determine the charge of the electron beams. The MATLAB routine written for this purpose analysed each pixel and all pixels with the colour code 15, representing the blue colour of the ICT signal, were saved into a new TIFF file. All pixels with other colours were ignored. A subroutine, written by Dr. Nicolas Bourgeois, determined the scale of the axes. Fig. 3.6 (right, top and bottom) shows an isolated single ICT trace for a low and high charge beam.

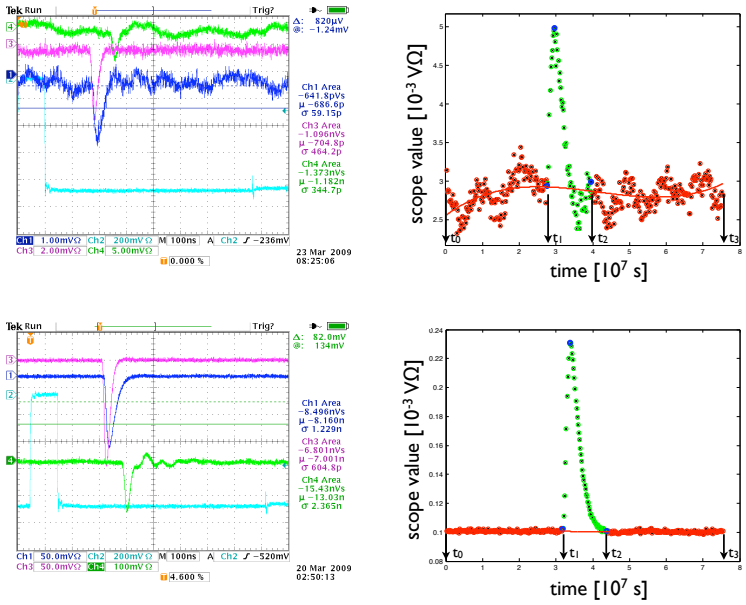

Figure 3.6: (Left, top and bottom) ICT oscilloscope images for a low charge beam (top) and a high charged beam (bottom). The trace recording our beam is shown in blue. (Right, top and bottom) Retrieved oscilloscope traces of the low charge beam (top) and high charge beam (bottom) which where multiplied with -1. Red circles indicate data points belonging to the background region and a solid red line depicts a 4^{th} order polynomial, which was fitted to the background points (excluding the green data points). Arrows indicate t_0, t_1, t_2 and t_3.

In order to integrate the curve and calculate the charge of the beam, the background noise needed to be subtracted. This was done by defining a time period before $(t_0 - t_1)$ and a time period after $(t_2 - t_3)$ the electron beam passed through the ICT. Both of these regions contain only background noise. All data points from these two regions were fitted with one 4th order polynomial. The integral of the polynomial from $t_0 - t_3$ was taken as the background sum and was subtracted from the integral over all data points. The subtraction yields the current $I(t)$ from Eq. (3.3) and dividing by the calibration factor $F = 5$, yields the charge. The calibration factor was provided by Bergoz [91].

To determine t_0, t_1, t_2 and t_3 automatically for the >1000 shots, the following method was used: t_0 was the first data point of the trace. t_1 was determined using the peak of the trace: for every trace, the onset of the electron signal trace starts at a fixed time interval Δt before the peak, that is determined by the electronics of the ICT. The value of t_2 was determined by examining 50 random scope traces with varying charges and finding a value Δt after the peak, that fits all charges. These values ($t_1 = 20.0\,\text{ns}$, $t_2 = 99.6\,\text{ns}$) were chosen to be as close as possible to the signal but also deep enough in the background. The point t_3 was the last point of the data.

3.3.2 Image plate data

To convert the raw TIFF images saved by the image plate reader into PSL values, the programs *image*J and MATLAB were used. The individual steps of the programs are outlined below.

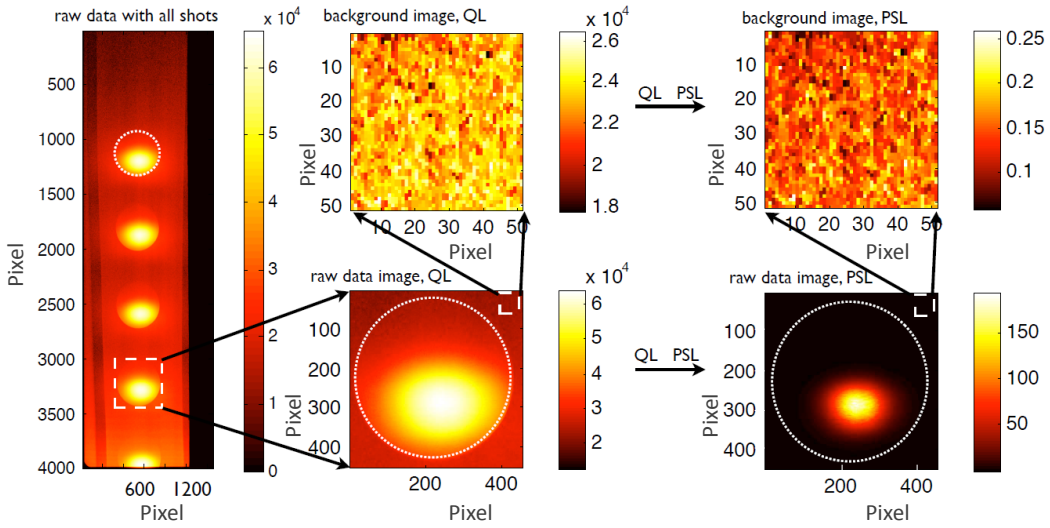

Figure 3.7: Image plate pictures recorded by the image plate reader. The raw data image with all shots of one run is pictured on the left. A single shot is selected (centre, bottom), from which a background region is defined (centre, top). White dashed squares indicate the regions. The white dashed circle indicates the beam pipe. The images on the left and in the centre are in units of quantum level. The images shown on the right are the same data after translating it into PSL.

The image plates used were 400 mm by 100 mm and were exposed to 4 or 5 shots each. An example image plate analysis is shown in Fig. 3.7. In order to analyse the shots separately, a region around the peak of each signal was defined. This area had dimensions of 50 mm × 50 mm and contained all of the exposed area of each shot (Fig. 3.7, centre). Within this 50 mm × 50 mm area a smaller region was defined in which only background signal was present. The smaller region will be referred to as the background image and is shown in Fig. 3.7 (centre, top) and the 50 mm × 50 mm region (Fig. 3.7, centre, bottom) will be referred to as the raw data image.

Overexposed images are excluded from this analysis. As mentioned before, the IP reader uses a logarithmic scale to digitize the image. The background image and the raw data image were converted pixel by pixel from the unit of the reader (quantum level, QL) to a linear scale with units of PSL. The formula used for the conversion stems from FUJI [92] and can be written as

$$\mathrm{PSL(Pixel)} = \left(\frac{R}{100}\right)^2 \left(\frac{4000}{S}\right) 10^{L\left(\frac{QL(\mathrm{Pixel})}{G} - \frac{1}{2}\right)} \tag{3.4}$$

where $R = 100$ is the scanning resolution in μm, $S = 5000$ and $L = 5$ are settings on the image plate reader called the sensitivity and latitude and $G = 65535$ is the bit depth for 16 bit images. The resulting PSL value is a floating-point number.

The average background pixel values were determined and multiplied by the number of raw image data pixels. The result was subtracted from the sum over all pixels of the raw data image.

Since the metastable states decay exponentially with time, the resulting PSL value has

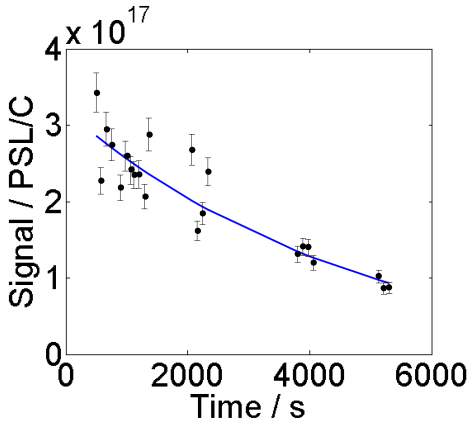

Figure 3.8: Measured decay characteristic of the image plate Fuji BAS IP-MS with an exponential fit (blue).

to be corrected to account for the interval between the time of exposure and the time of readout. To determine the decay characteristic of the image plate, a detailed study was performed, which is described below. Given (i) the measured decay constant, (ii) the knowledge of the time of exposure to the electron beam, and (iii) the time of readout, the original PSL value at time of exposure could be determined. This corrected PSL value was then used to determine the number of electrons per PSL.

Decay constant

Fig. 3.8 shows the fading characteristic of the Fuji BAS IP-MS image plate. The data points come from five runs taken within 6 hours. The image plate in each run was exposed to similar beam charges, but the charge did vary slightly. This was corrected for by dividing the PSL values by the charge of each beam, which was measured by the ICT shown in Fig. 3.5. Image plates were read out after 600, 1000, 2200, 3900 and 5200 seconds. An exponential decay was fitted to the data points and the decay constant k was determined to be

$$1/k = (4783 \pm 717)\,\mathrm{s}. \tag{3.5}$$

The result lies within the error range of the published value of $1/k = (6420 \pm 1143)$ s [94]. The measured value of our study was used to correct all other PSL values of the analysis.

Stability of the PSL value against small changes of the parameters

During the experiment, much care went into ensuring that the IP was not exposed to extra light before readout. Such premature exposure of the image plate to light from sun or the room diminished the image plate reading. Several tests were performed to test if extra light exposed the image plate before readout. These tests are described below.

As mentioned above, the image plate was wrapped in aluminum until it was unpacked in a dark environment created by a black, optical cloth covering the image plate reader. Direct sunlight exposure during the transport or unpacking, however, can lead to significantly reduced signals. A test was performed to see how quickly direct sunlight would erase some

of the metastable states on the image plate: two image plates were both exposed to four electrons shots each with the same charge in each shot. One of the plates was exposed to 5 seconds of direct sunlight. Analysis showed a 39 % reduced PSL value in the image, which was exposed to direct sunlight. Reproducible direct sunlight exposure can be excluded, because the image plates were kept inside the aluminium and underneath the cloth at all times, and accidental exposure to a few plates can be excluded because all image plate data show similar ranges. Indirect exposure to the plates, however, underneath the cloth, must be considered. According to the manufacturer of the IP reader, the effect of indirect light passing through the cloth can be of an order of magnitude lower than direct sunlight. This means if there was exposure of all image plates to indirect sunlight, it would be of the order of 4%. Data taken on day two of the image plate sensitivity experiment was all taken during the night and hence sunlight would have not been a factor. The result from that night, however, shows a higher sensitivity, than data taken on day one[6]. It was concluded that accidental exposure to sunlight was not present at the experiment.

In order to understand the effect of errors in the decay constant, the effect on the deduced PSL value of varying the decay constant was investigated. The effect was found to be small due to the very slow exponential decay of the image plates: given $f = \exp(-t \cdot k)$ and $\Delta f = -t \exp(t \cdot k)\, \Delta k$, errors can be estimated using $\frac{\Delta f}{f} = \Delta k \cdot t$. Given $t = 1000\,\mathrm{s}$ and using the published value of $k = 1/6400\,\mathrm{s}$, the resulting error is 5.2 %. Similar arguments can be made about the readout time after exposure; all images were read out between 700 s to 1000 s after exposure. Errors in the readout time of 200 s, much larger than the estimated error, change the PSL value by less than 5 %.

In a third test, the size of the background image and the raw data image were changed. The background PSL value is two orders of magnitude lower than the raw data image PSL value. Changing the size or shifting the background region to other locations within the raw data image did not change the PSL result significantly. Similarly, the size of the signal region did not greatly effect the result as long as the electron beam and the beam pipe are contained within the image. On most quantum level IP images, the outline of the beam pipe can be seen. Sometimes the beam seems significantly clipped by the beam pipe. However, owing to the logarithmic scaling, after conversion of the QL IP images into PSL values, the outline of the beam pipe is not visible any longer and the beam looks unclipped. The reason, that the QL IP images looks like they show cut beams, is that the QL scale is logarithmic — and that the image plate is very sensitive to even small numbers of electrons — allowing the image plate reader to detect two orders of magnitude lower signal than the peak electron signal.

After performing these tests, it was concluded that it is unlikely that the PSL value was diminished by sun or room light, errors in the decay constant, errors in the readout time, or size of the raw data image.

3.3.3 Scintillating screen data

The CCD images were analysed by a MATLAB program. After removing x-rays hits by excluding isolated maximum-value pixels, overexposed images were excluded. A background

[6] Therefore accidental exposure to sunlight does not explain the discrepancy presented in the result section of this section.

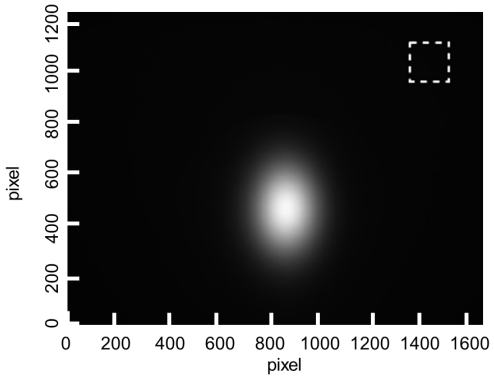

Figure 3.9: CCD image of an electron beam passing a Lanex screen. The background region is shown as a white dotted square.

region was defined in the upper right hand corner of the image indicated by the white, dashed line in Fig. 3.9. The background image was resized to the size of the whole image and a background subtraction was performed by subtracting each pixel by its corresponding background image pixel. The background level remaining was two orders of magnitude lower than the signal values. Since the beam is non-circular, it was fitted to the function

$$L(x,y) = L_{\max} \times e^{\left[\frac{x}{\sigma_x^2}+\frac{y}{\sigma_y^2}\right]/2}. \tag{3.6}$$

This yields $L_{\max}$ and $\sigma = \sqrt{\sigma_x \sigma_y}$, which are the maximum and width of the distribution[7]. Given the beam area $A = \pi\sigma^2$ and the charge Q, determined from the ICT signal (§3.3.1), the charge density $\rho = Q/A$ can be calculated. Plotting $L_{\max}$ as a function of the charge density ρ reveals, that the signal from the Lanex screen increases linearly with increasing charge density.

The Lanex screen was located 3 mm behind the image plate. In order to check that the presence of the image plate did not affect the Lanex screen, some runs were performed without the image plate in front of the Lanex screen. Differences in the CCD signal with image plate in front and without were found to be less than 1 %.

Absolute calibration

An absolute charge calibration was performed for the KODAK Lanex Regular Screen by calculating the number of electrons expected theoretically per measured CCD count. This charge calculation was then compared to the ICT charge measurement. The layout of the experiment was the same as shown in Fig. 3.5 and the variables used are described below in detail.

The charge of the beam ($Q_{\mathrm{b}}^{\mathrm{cal}}$) can be calculated by multiplying five factors which are described in detail in the following paragraphs: (i) the number of CCD counts ($\mathrm{N}_{\gamma}^{\mathrm{det}}$) — corrected for the camera efficiency to detect all arriving photons; (ii) a factor that corrects that the optical set-up only covers a certain angle in space (k_{optic}); (iii) the reciprocal of the number of photons created inside the Lanex screen per electron ($\mathrm{N}_{\gamma}^{e^-}$); (iv) a factor accounting

[7] Even though the beam did have a non-circular shape, σ_x and σ_y only differed by a maximum factor of 1.4.

for the fact that not all created photons reach the surface from within the Lanex screen ($1/\zeta_{\text{trans}}$); and (v) the charge of one electron (e). Hence, the calculated charge is related to the CCD count by Eq. (3.7) and the individual factors are detailed below:

$$\begin{aligned} Q_{\text{b}}^{\text{cal}} &= \text{N}_{\gamma}^{\text{det}} \cdot k_{\text{optic}} \cdot \frac{1}{\text{N}_{\gamma}^{e^-}} \cdot \frac{1}{\zeta_{\text{trans}}} \cdot e \\ &= \frac{\text{CCD count}}{\epsilon_{\text{QE}} \frac{1}{\text{N}_{e^-}^{\text{CCD}}}} \cdot \frac{1}{\frac{d\Omega}{\pi} \cos(\theta_{\text{CCD}})} \cdot \frac{1}{\text{N}_{\gamma}^{e^-}} \cdot \frac{1}{\zeta_{\text{trans}}} \cdot e \end{aligned} \tag{3.7}$$

Number of photons created per electron passing Lanex screen, $\text{N}_{\gamma}^{e^-}$: Using the method described by Glinec et al. [95], the number of photons created inside the Lanex screen by one electron is:

$$\text{N}_{\gamma}^{e^-} = \frac{\epsilon \, \text{d}E/\text{d}x}{\text{E}_{\gamma}} \, d = \frac{1.8\,\text{MeV/cm}}{2.27\,\text{eV}} \, 87.4 \cdot 10^{-4}\,\text{cm} = 6.1 \cdot 10^{4}, \tag{3.8}$$

where $\epsilon \, dE/dx$ is the yield of kinetic energy of an electron passing the scintillating screen transformed into visible light, E_{γ} is the energy of the photon of the central wavelength of the emitted light from the screen, and d is the screen's thickness.

Fraction of generated fluorescence photons leaving Lanex screen, ζ_{trans}: T. Radcliffe et al. [96] estimate that 22% of the photons created inside the Lanex screen exit the screen:

$$\zeta_{\text{transmission}}^{\text{Lanex}} = 0.22.$$

Fraction of photons reaching the first lens: The lens in front of the camera had a diameter of 52.4 mm, but only photons entering inside a 7 mm radius from the centre of the lens reached the CCD chip. This result was determined by measuring the light intensity hitting the CCD camera chip, while closing an iris placed in from of the lens system. From this measurement, the solid angle collected by the CCD camera was found to be,

$$\begin{aligned} \text{d}\Omega &= \int_0^{\theta_0} \sin\theta \, \text{d}\theta \, \text{d}\phi = 2\pi \left[-\cos(\theta)\right]_0^{\theta_0} = 2\pi \left[1 - \cos(\theta_0)\right] \\ &= 2\pi \left[1 - \cos\left(\tan^{-1}\left(\frac{0.014/2}{0.455}\right)\right)\right] = 0.74 \cdot 10^{-3} \end{aligned} \tag{3.9}$$

and with $\theta_{\text{CCD}} = 10\,^{\circ}$

$$\cos(\theta_{\text{CCD}}) = 0.985. \tag{3.10}$$

Quantum Efficiency: Quantum efficiency (QE) is defined as the reciprocal of the number of photons per CCD pixel required to generate one electron in the CCD circuit. The manufacturer of the camera measure the QE to be 50 %.

$$\epsilon_{\text{QE}} = 0.5 \tag{3.11}$$

Number of electrons per CCD count: The conversion between the number of electrons and CCD counts (analog to digital) was measured by the manufacturer to be 0.195784 electrons per ADU (Analog to Digital Unit). They used the FL2-20S4M camera with Firmware 1.2.2.0 and the mode in operation was MONO16 pixel format with maximal bandwidth at 1624 ×

1224 resolution. The author used the same settings. Since the camera is a 12 bit model, this results in a factor of 3.13 electrons to increase the CCD count by one.

$$\frac{N_{e^-}^{\text{per ADU}}(=N_{e^-}^{\text{CCD}})}{\text{levels}} = \frac{N_{e^-}^{\text{CCD,x bit}}}{2^x} = \frac{0.195784}{\frac{1}{2^{16}}} = \frac{N_{e^-}^{\text{CCD,12 bit}}}{\frac{1}{2^{12}}} \tag{3.12}$$

$$N_{e^-}^{\text{CCD,12 bit}} = 0.195784 \cdot \frac{2^{16}}{2^{15}} = 3.1325 \tag{3.13}$$

Using the information of the previous paragraphs and Eq. (3.7) results in the absolute calibration of the calculated beam charge of:

$$Q_b^{\text{cal}} = \frac{\text{CCD count}}{0.5\,\frac{1}{3.1325}} \cdot \frac{1}{\frac{0.74\cdot 10^{-3}}{\pi}\,0.985} \cdot \frac{1}{6.1\cdot 10^4} \cdot \frac{1.6\,10^{-19}\,\text{C}}{0.22} = \tag{3.14}$$

$$Q_b^{\text{cal}} = 3.2\cdot 10^{-19}\,\text{C} \times \text{CCD count}. \tag{3.15}$$

3.4 Results

The results of the DAFNE experiment are presented in this section. First, the sensitivity result for the image plate is discussed in §3.4.1 and in §3.4.2 the results for the Lanex screen are presented. Results are compared to other work published after the experiment was performed.

3.4.1 Sensitivity of FUJIFILM BAS-IP MS image plates

The results for the sensitivity of FUJIFILM BAS-IP MS image plate scanned with a BAS 5000 reader from FUJI with 100 μm resolution are presented. Data was taken on two separate days and, unfortunately, the two data sets do not agree: data taken on 19th March 2009 yield a ten times lower value of PSL per electron than data taken on 22nd March 2009. Both results are shown in Fig. 3.10 accompanied by the previously accepted calibration [86], shown in black. The mean value of the sensitivity of IP-MS image plates for the day 1 is

$$S_{\text{MS}}^{\text{day1}} = {}^{\text{PSL}}/_{n_e} = (0.0053 \pm 0.0002)\,\text{PSL}, \tag{3.16}$$

which corresponds to (189 ± 8) electrons per measured PSL. For day two the result is

$$S_{\text{MS}}^{\text{day2}} = {}^{\text{PSL}}/_{n_e} = (0.0487 \pm 0.0028)\,\text{PSL}, \tag{3.17}$$

which corresponds to (20.5 ± 1.2) electrons per measured PSL.

Both data sets were analysed with the same software and, therefore, the difference must lie in the raw data. That the ratio of the two sensitivity measurements is close to a factor of ten, hints at the possibility, that a simple resistor in the ICT set-up or a switch on the image plate reader was set incorrectly. Both possibilities were extensively investigated, but none were confirmed. Between the two experimental days, however, a DAFNE scientist optimized

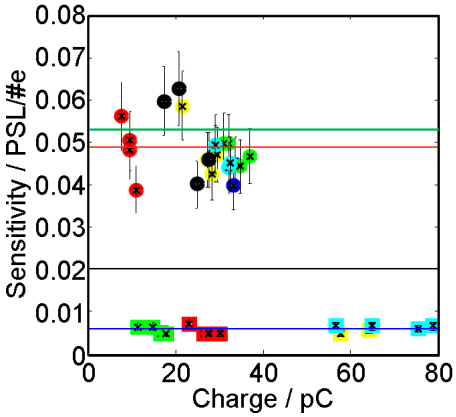

Figure 3.10: Experimental result for the IP sensitivity. Data points from day one (square) and from day two (circle) are shown, with different runs indicated by a different colour. Clearly visible is the divide between day one and day two. The average values are indicated by blue and red lines, the previously accepted calibration value is shown as a black line [86]. The result from the publication [84] is shown as a green line.

the ICT set-up. While we were assured that the ICT (which was beyond our control) had been set up identically on both days, the most likely source of error was a faulty ICT reading on day one.

Shortly after our experiments were concluded, Zeil et al. [84] published a similar study on the sensitivity of image plates. Our sensitivity result from day two ($S_{MS} = 0.0487\,\text{PSL}$) is in good agreement with the experimental result published by Zeil et al. of $S_{MS} = 0.0534\,\text{PSL}$. Zeil's et al.'s experiment operated with a beam energy of 20 MeV and beam charges of up to 60 pC. The measurement from Zeil et al. of the same quantity makes it even more likely that some instrument during day one of our experiment was set-up incorrectly, and that the measurement of $S_{MS} = 0.0487\,\text{PSL}$ represent a correct, and independent measurement of the image plate sensitivity. Zeil's et al.'s and our value deviate significantly from the previously accepted value of 0.02 PSL — for which reasons were discussed in the motivation — and show the importance of experimental confirmation.

3.4.2 Charge density response of Kodak Lanex regular screens

Fig. 3.11 shows the signal from a Kodak Lanex Regular screen as a function of charge density ρ between $\rho = 2 \times 10^{-7}\,\text{Cm}^{-2}$ and $\rho = 10^{-5}\,\text{Cm}^{-2}$. The charge density scan was predominantly a charge scan and charges were changed from 10 pC to just over 1000 pC. This result shows clearly, that the Lanex signal varies linearly with charge density up to charge densities of at least $\rho = 10^{-5}\,\text{Cm}^{-2}$ with no saturation effect observable. It is worth emphasizing that, in current laser wakefield experiments, the charge density of the bunches detected lies within the linear range tested.

These results are in good agreement with a publication by Buck et al. [83], which were performed at the same time as the experiment of Zeil et al. [84], and published a short time after our experiment was concluded. In these experiments, Buck et al. [83] used a 40 MeV beam with charge densities ranging from $\rho = 10^{-9}\,\text{Cm}^{-2}$ to $\rho = 10^{-5}\,\text{Cm}^{-1}$ to calibrate eight

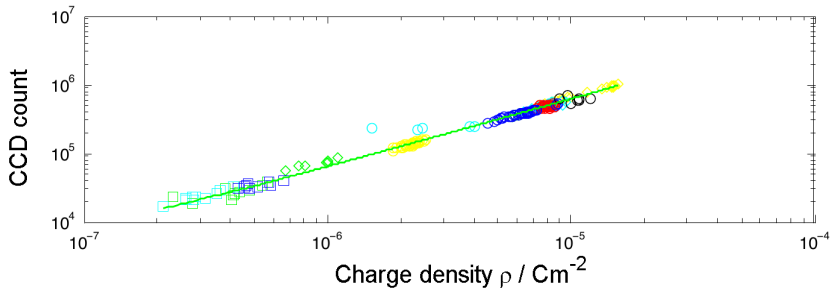

Figure 3.11: Fluorescence signal from Kodak Lanex Regular screen for different charge densities.

different scintillating screens. While the experiment calibrated more screens, and introduces a very interesting technique to calibrate the optical set-up with a radioactive source, the larger range of charges densities were achieved in multi-bunch mode: each 50 pC bunch was separated by its predecessor by 154 ns resulting in 3 to 300 μs short bunch trains. Thus, the nanosecond short, single bunch experiment, described in this chapter, gives a stronger indication, that saturation in Lanex screens is not present up to $\rho = 10^{-5}\,\mathrm{Cm}^{-2}$. How scintillating screens reacts to femtosecond bunches — present in LWFA experiments — is a different question and cannot be answered by either experiment. An experimental run at a facility like SparX or a different femtosecond short electron accelerator facility would be beneficial in this regard.

The ratio between the absolute calibration of the Lanex screen and the charge measured by the ICT was ≈ 2. Given the many uncertainties on which the calculated value is dependent, the agreement is reasonably good.

3.5 Conclusions

The response of FUJIFILM BAS-IP MS image plates and Kodak Lanex Regular screens, to electron beams with energies of 505 MeV, has been studied.

The studies confirmed that fluorescence signal from Kodak Lanex Regular screens varies linearly with the charge density of nanosecond electron bunches for charge densities in the range between $\rho = 2 \times 10^{-7}\,\mathrm{C/m^2}$ to $\rho = 10^{-5}\,\mathrm{C/m^2}$. This result is in agreement with measurements by Buck et al. [83]. The charge densities typically encountered in laser wakefield experiments lie in this range. The only remaining uncertainty, in assuming that the Lanex response is linear, is, that the electron bunches from LWFAs are in the femtosecond regime, whereas our measurements were done with nanosecond bunches. Further work is required to eliminate this uncertainty.

The sensitivity measurement of FUJIFILM BAS-IP MS image plates resulted in a value of $S_{MS} = (0.0487 \pm 0.0028)$PSL or (20.5 ± 1.2) electrons per PSL. This value is significantly larger than that simulated by Mangles [86], but it is in close agreement with measurements by Zeil et al. [84].

Chapter 4

Discharge and waveguide development

This chapter discusses the discharge and waveguide development of the capillary discharge waveguide.

The chapter is divided into two parts: in the first, electronic development of the capillary discharge waveguide is discussed, and in the second, the miniaturising of its housing is summarised. Electrical discharges in general are introduced in §4.1.2 and the capillary discharge of our waveguide is discussed in §4.1.3. Experiments performed to improve the electrical discharge design are investigated in §4.1.4 and conclusions are drawn in §4.1.5. In the second part of this chapter, the motivation for, the benefits of, and the implementation of miniaturising the housing of the waveguide are discussed in §4.2.1, §4.2.2, and §4.2.3, respectively.

4.1 Electrical discharge development

4.1.1 Motivation

Laser wakefield experiments usually employ gas-jets or a waveguide filled with gas to accelerate electrons. Our group uses the capillary discharge waveguides [72]. While gas-jet experiments do not ionise the gas — the laser pulse itself does — the electrical discharge in our waveguide is used to ionise the gas, which then forms the guiding structure. Because the electrical noise created by the initial breakdown of the gas can interfere with sensitive electronic equipment — either that controlling the laser system, or associated with the diagnostics — it was decided to investigate ways by which this might be reduced.

This section starts with a brief introduction to electrical discharges in §4.1.2. The electrical circuit of the capillary discharge waveguide is introduced in §4.1.3 and attempts to improve on the existing discharge design with a glow discharge circuit are described in sections §4.1.4. Section §4.1.5 explains the conclusions of these studies.

4.1.2 Introduction to gases discharges

The phenomenon of conduction of electricity through gas is discussed at length in many books and articles [97–100]. This chapter follows the approach of F.M. Penning [101]. In this introduction, no attempt will be made to review all discharge types, but it will be confined to the discharges present in the experiments described in this chapter.

The conduction of electricity through a metal wire is governed by Ohm's law $V = IR$, where V is the voltage, I the current, and R the resistance of the wire. In the wire, the electrons can flow via the conduction band when a potential difference is applied to its two ends. The simple picture of moving electrons in a wire is quite different to the conduction of electricity in a gas: firstly, the electrons are initially bound to each molecule and enormous forces need to be applied to ionise them. Hence a gas usually acts as an isolator until broken down. Secondly, once ionised species are present, the current consist of two flows: one of electrons towards the positive electrode and another made of ions flowing towards the negative polarity. The velocity acquired by the ions, however, is much slower than their electron counterparts due to their heavier mass. The ions remain inside the volume of ionised gas much longer and — if there are equal numbers of electrons and ions — create a space charge effect. The electrons and ions can move freely around the volume and, as a consequence, they can collide, excite and further ionise. Heat is created in gaseous discharges and can either heat the gas or leave the plasma in the form of radiation. In the next few paragraphs, arc and glow discharges are introduced.

A gas, placed between two metal electrodes, is the simplest discharge set-up. When the voltage between the electrodes is low, the gas remains an insulator. Upon increasing the voltage further, the gas at some point reaches the breakdown voltage V_b at which point the gas becomes conductive. The transformation of the gas from an insulator into a conductor may take the form of sustained or un-sustained discharges. The latter is called an *arc discharge* or more often a *spark discharge* and constitutes a current of high intensity and very short duration, which drops the initially high resistance of the gas to a few Ohm. In this regime, the number of electrons in the current is proportional to $\mathrm{e}^{\eta V_\mathrm{b}}$, where η is the number of ionisations created by a single electron per volt of potential difference. When $\mathrm{e}^{\eta V_\mathrm{b}}$ becomes large, the spark commences and the electrons drive a heavy current through a very narrow conductive channel. Because the channel over which the electrons conduct is narrow and fully ionised, the current dies out fast for there are no more replenishing molecules to be ionised. Hence the current is strong, but short lived. During the time of the spark, the ions do not move significantly and, therefore, do not contribute to the current flow. As an extreme example, a spark discharge might have a peak current of more than 1 kA, at voltages exceeding 100 V. However, because the current only flows for a short time, the charge transferred might only be 1 C, corresponding to an energy dissipation of 100 J.

The second type of discharge discussed here, is the called a *glow discharge*. While the current for spark discharges is high, and the current is short lived, the current present in glow discharges is of the order of milliamperes, but is sustained over a long period. The breakdown voltages V_b vary between 100s of volt and several 10s of kV. The simplest glow discharge is the direct current (DC) glow discharge, which starts to conduct current through the gas when an initial molecule is ionised randomly, for example, by a cosmic ray or thermal collision within the plasma. Electrons and ions are forced through the gas to their respective opposite polarity electrode, ionising more molecules on their way. For the time the voltage

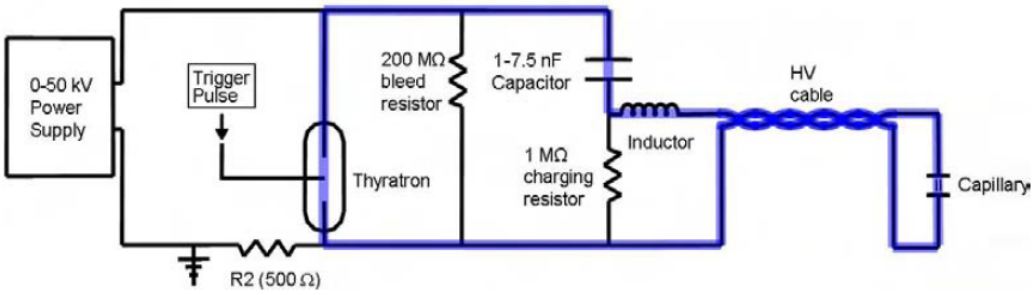

Figure 4.1: The high voltage circuit used to drive the current pulse through the capillary. The capacitor is charged via the 1 MΩ resistor, and when the thyratron switches, current flows through the capillary as shown by the blue shaded path. The circuit diagram was taken from [64].

on the electrodes is supplied, the population of electrons and ions remains high enough to sustain a constant current. Molecules of the gas are not the only part that contribute to the current flow: ions and molecules hitting the cathode eject molecules of the cathode material which can then become ionised and drift towards the respective electrodes. When ions recombine with electrons, a photon is released and it is this radiation, which constituted the word “glow" of the glow discharge. An example of a glow discharge in every day life is the plasma TV screen.

This concludes the introduction and in the following, the pulsed discharge used by our group, is introduced.

4.1.3 Pulsed discharge

The electrical circuit of the capillary discharge waveguide, which was introduced in §2.6.3 and used in the experiments described in chapters 5 and 6, is introduced.

Discharge circuit

Fig. 4.1 shows the discharge circuit diagram of the capillary discharge waveguide. A power supply of 30 kV was used to charge the 1.7 nF capacitor initially via a 1 MΩ resistor. An inductor can be included in the circuit which, in combination with the inductance of the high voltage (HV) cable, lengthens the discharge pulse. The capacitor is discharged — and the plasma channels forms — when the trigger is activated and the Thyratron switch completes the discharging circuit, shown here in blue. The discharge circuit can be synchronised with a laser system trigger via a digital delay generator and, hence, the time between the discharge and the laser pulse arrival at the capillary can be varied. A bleed resistor is implemented to allow the capacitor to discharge when the power supply is turned off.

Fig. 4.2 shows the temporal variation of the discharge current measured by a Rogowski coil. The measurement uses the induced current in a Rogowski coil connected to an oscilloscope. The length of the HV cable was kept as short as possible, but the distance between the capacitor and capillary was ≈ 2 m. Clearly visible are modulations in the current pulse, which are due to impedance mismatch between the discharge and the electrical ca-

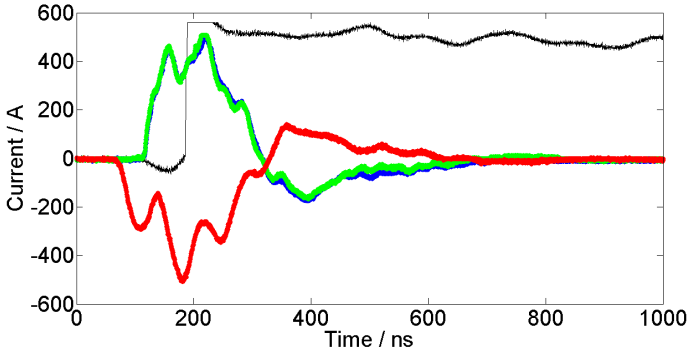

Figure 4.2: Temporal variation of the discharge currents. The green and blue traces are the input and output current at the capillary, the red trace displays the current variation close to the capacitor and the black line indicates the arrival of the laser pulse.

bles connecting it to the capacitor. Different profiles were measured depending on where the Rogowski coil was placed, which are indicated by different colours.

The waveguide

Fig. 4.3 (a) shows a photograph of the waveguide and its housing used by Ibbotson et al. [1][1] The waveguide used by the author is built on the same principle as described by Gonsalves' thesis [64] and is described briefly here. The waveguide is built by two sapphire blocks — a 2-D plot of one sapphire block with gas-slots is shown in Fig. 4.5 — which each have a semi-circular groove laser-machined along their length [102]. The two sapphire blocks are then placed into the perspex holder and a cylindrical capillary is formed by aligning

[1]The housing used by the author in experiments described in chapters 5 and 6 differs from the one shown in Fig. 4.3 and is described in detail in §4.2 of this chapter.

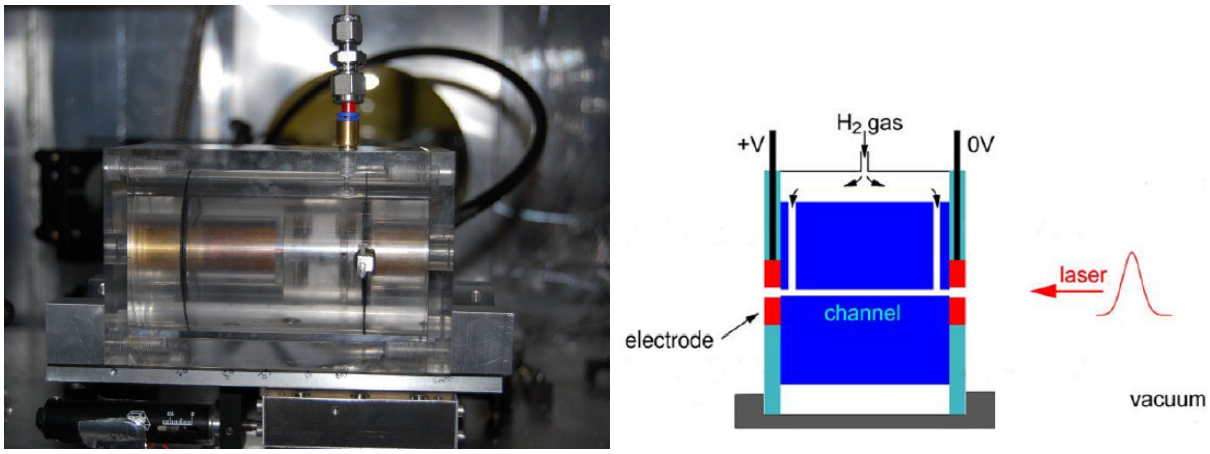

(a) (b)

Figure 4.3: The hydrogen-filled capillary discharge waveguide within the old housing. (a) Photograph of the waveguide and its housing on top of a 5-axis stage in the Astra-Gemini vacuum chamber. This photograph was taken by the author during the experiments by Ibbotson et al. [1, 2] (b) Schematic of the waveguide taken from [64].

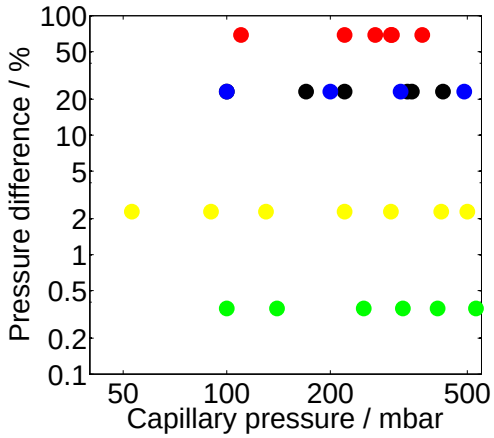

Figure 4.4: Difference between the fill and capillary pressure in % as a function of capillary pressure for different gas slot diameters. The red (blue, black, yellow) data points were taken with a gas slot diameter of 75 μm (312 μm, 400 μm, 650 μm) and pulsed gas supply. The green data points were taken with a gas slot diameter of 400 μm and the gas was free-flowed into the capillary. All data was accumulated with a capillary with a diameter of 200 μm. The experimental equipment to take the data was prepared by Dr. Anthony Gonsalves and details of the set-up can be found in [64].

the two semi-circular grooves with metal screws. In addition to the semi-circular groove, one of the sapphire blocks has two 650 μm diameter groves cut into it perpendicular to and overlapping with the capillary groove. These two so-called gas-slots let hydrogen gas flow into the capillary and are situated 4 mm away from either end of the capillary. A gas tube connected to the housing fills the housing, the gas slots, and the capillary with gas. A pressure regulator regulates the gas pressure which can be either pulsed into the capillary for 2 s via a solenoid switch, or free-flowed by leaving the valve open. Earlier work by

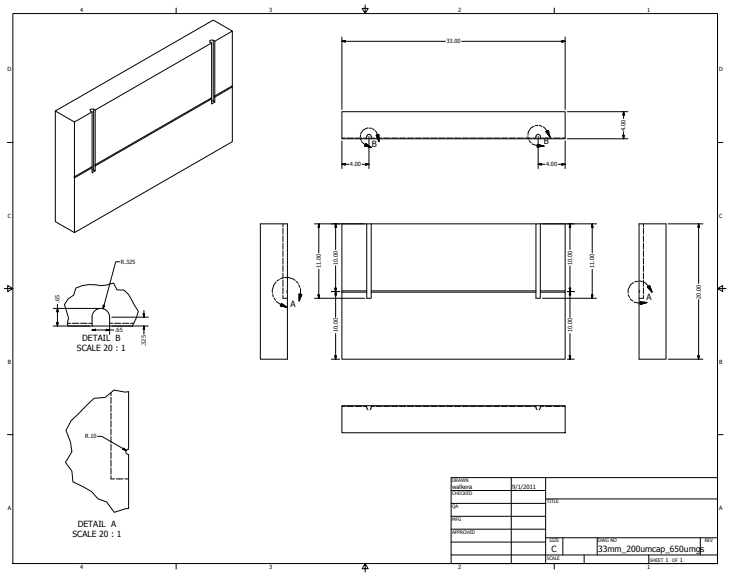

Figure 4.5: A 2-D view of the sapphire blocks with gas slots on either side of the capillary. This graph was produced with the AutoCAD software.

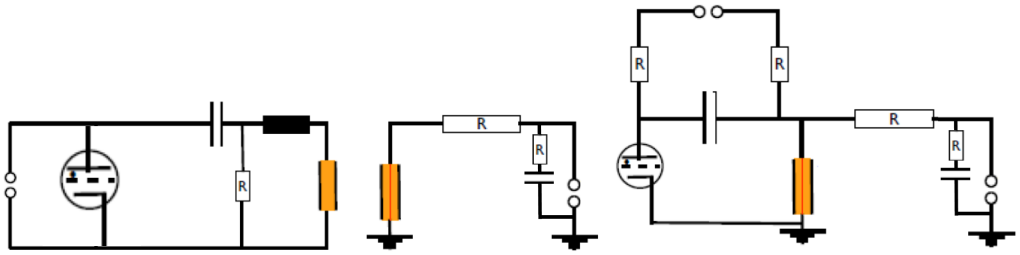

Figure 4.6: Schematic diagrams of (a) pulsed, (b) simmer, and (c) combined circuit also referred to as circuit 1, circuit 2, and circuit 3, respectively. The capillary is displayed in orange colour with the simmer current suggested as red line.

members of the group showed that if the diameter of the gas slots was larger than that of the capillary by a small factor, then the pressure inside the capillary is equal to that of the pressure inside the gas supply line. Experiments performed by the author, of which the results are presented in Fig. 4.4, confirmed that 650 μm diameter gas-slots are sufficient to create a pressure difference between the fill pressure (or gas supply line pressure) and the capillary pressure of less than 5 %. The red (blue, black, yellow) data points in Fig. 4.4 were taken with a gas slot diameter of 75 μm (312 μm, 400 μm, 650 μm) and pulsed gas supply. The green data points were taken with a gas slot diameter of 400 μm and the gas was free-flowed into the capillary. One can see that the free-flow method does reduce the requirement for large gas-slots, however it has the disadvantage of filling the chamber with more gas than is needed. After the gas is flowed into the capillary, the discharge is activated and the plasma channels forms.

4.1.4 Glow discharge

Combining a glow discharge with the pulsed discharge circuit of §4.1.3 has potential benefits in comparison to the pulsed discharge on its own. That is because: (i) the voltage required to drive the main discharge current could be reduced, since the simmer current creates a constant low impedance current flow through the capillary; (ii) the main discharge pulse would generate less electrical noise because of the lowered voltage; (iii) the main discharge pulse would rise faster; and (iv) the jitter of the main discharge pulse would drop. For these reasons, a glow discharge circuit was built and tested by the author.

Experimental setup

Fig. 4.6 shows schematic diagrams of the electrical circuits of the simplified pulsed discharge [64] (a), the glow discharge (b), and the combined circuit (c). The capillary with its gas is indicated in orange and the simmer current is portrayed as a red line. In Fig. 4.6 (b) the HV power supply supplies the break down voltage V_{br} and in simmer mode the current I_{s}. The capillary — set in the housing used by Dr. Anthony Gonsalves [64] — was placed in the interferometry vacuum chamber in Oxford. Because the pressure p close to the exits of the capillary was $p \approx 0.1\,\mathrm{mbar}$, and a better vacuum pump was not available, the high voltage applied to the HV electrode discharged to the grounded vacuum chamber frequently. To

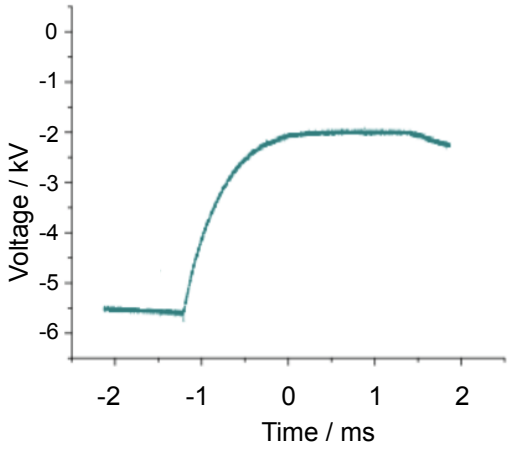

Figure 4.7: Voltage measured for the initial spark discharge. The voltage was measured at the HV side of the capacitor.

study the characteristics of the simmer circuit, it was therefore necessary, to shield the HV electrode by a perspex block and epoxy glue. This eliminated the discharges onto the vacuum chamber and enabled the study of the glow discharge. The gas used in all experiments was helium gas. For simplicity, the pulsed, simmer, and combined circuit will be called circuit 1, circuit 2, and circuit 3, respectively, all displayed in Fig. 4.6.

The glow discharge was tested in three steps: (i) a glow discharge was established with circuit 2, with the HV electrode isolated from the grounded vacuum chamber; (ii) the glow discharge was combined with the pulsed discharge to form circuit 3, and improvements of the combined setup were investigated; and (iii) with the isolation of the HV electrode removed the glow discharge was tested without the pulsed discharge (circuit 2). While improvements were good, the small range of operable pressures for the glow discharge found in (iii), forced us to abandon the design change at this point. Results of these three steps are presented below.

Glow discharge with isolated HV electrode

A stable glow discharge was achieved in a 15 mm short, 300 μm diameter, sapphire capillary with helium pressures varied between 2 mbar to above 200 mbar. The gas supply was free flowed into the capillary. DC currents of the order of milliampere were observed with an operating voltage $\geq 10\,\mathrm{kV}$. Details of the investigation are given below.

For voltages of $-5\,\mathrm{kV} \geq V \geq -10\,\mathrm{kV}$, the discharge was found to be unstable: an ampere-sized current pulse was observed, followed by a period of 10s of microseconds in which no current flow was recorded within the capillary. This behaviour is characteristic for spark discharges: the capillary with its two electrodes form a capacitor, which breaks down in a spark, when the breakdown voltage of the pressure-capillary length system is reached. The jitter in time between the trigger pulse and discharge is large. In Fig. 4.7 one can recognize the discharging curve of the capacitor.

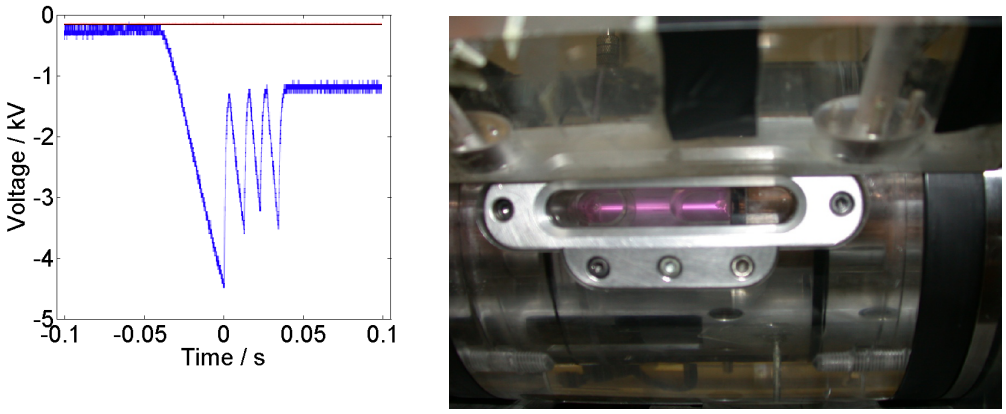

(a) (b)

Figure 4.8: (a) Voltage trace measured close to the capillary for a 15 mm capillary while entering the stable simmer current state. (b) Stable glow discharge inside a 50 mm capillary.

For voltages of $-10\,\mathrm{kV} \geq V \geq -18\,\mathrm{kV}$, the initial spark evolves into a stable glow discharge which can be seen in Fig. 4.8: sparks occur initially — several times the capacitor discharges through the capillary within 1 ms followed by its charging over a time of 10 ms — but after the initial discharges, the charge density is sufficiently large for the voltage and current to stabilise at a few kV and few mAs. A stable glow discharge has formed and can be maintained indefinitely. In Fig. 4.8 (a), the voltage trace is shown over a period of 200 ms: the power supply voltage is turned on at $t \approx -50\,\mathrm{ms}$ and breakdown happens at $t = 0\,\mathrm{s}$, followed by several spark discharges before the simmer current is stable. After operating at voltages between $-10\,\mathrm{kV} \geq V \geq -18\,\mathrm{kV}$ for several minutes, the discharge can be initiated and maintained as a simmer discharge with voltages $V \geq -10\,\mathrm{kV}$. The data shown in Fig. 4.8 were taken after five minutes of operation.

Note that it was found that using a coaxial cable to connect the capacitor and electrodes meant that a stable glow discharge could not be obtained: spark discharges were created with or without coax cable for voltages of $V \geq -10\,\mathrm{kV}$. With the coax cable, however, these sparks did not disappear when operating at voltage of $-10\,\mathrm{kV} \geq V \geq -18\,\mathrm{kV}$, because of the charging and discharging of the intrinsic capacitance of the coax cable. The stable glow discharge was only observed using separate, isolated wires for either electrode.

Glow and pulsed discharge combined

After the initial test of the glow discharge, circuit 1 and circuit 2 were combined as shown in Fig. 4.6 (c). To simulate long capillaries — which need higher breakdown voltages than were available — a 15 mm short, 300 μm inner diameter capillary was used, but operated at low voltage. Fig. 4.9 shows the results obtained with circuit 1 (black) and circuit 3 (green), which indicate the great advantages the combined circuit (circuit 3) has over the pulsed discharge (circuit 1) alone.

Operating the combined circuit with $V_{\mathrm{simmer}} = -20\,\mathrm{kV}$ and $V_{\mathrm{pulsed}} = +7\,\mathrm{kV}$, the peak current of the main pulse is 22 % higher and its standard deviation is an order of magnitude lower than operating with circuit 1. The simmer current also reduces the jitter between the

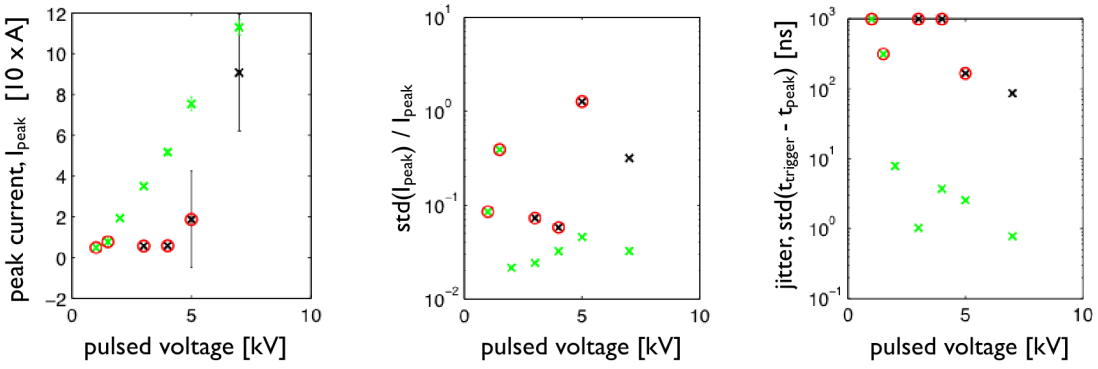

(a) (b) (c)

Figure 4.9: (a) Peak current, (b) standard deviation, and (c) jitter for a 15 mm, 300 μm capillary using 50 mbar of Helium pressure for the combined circuit (circuit 3, green crosses) and the pulsed discharge alone (circuit 1, black crosses). Red circles indicate unstable discharges.

trigger pulse and main discharge pulse to less than 1 ns.

When reducing the pulsed voltage V_{pulsed} to $\leq 5\,\text{kV}$— to simulate very long capillaries at higher voltages — the simmer current of circuit 3 enables the main pulse to discharge through the capillary every time, while the pulsed discharge of circuit 1 becomes unstable — indicated by the red circle — and often does not discharge through the capillary. The jitter of both circuits increases but it stays around several nanoseconds for circuit 3. For $V_{\text{pulsed}} \leq 1.5\,\text{kV}$ circuit 3 does also not discharge through the capillary reproducibly any longer.

When V_{pulsed} is raised to 10, 20, or even 25 kV, the picture is similar to the case of $V_{\text{pulsed}} = 7\,\text{kV}$: for circuit 3, the peak current is higher and the standard deviation lower, while the time jitter becomes comparable in both circuits. A short experiment was performed with a 50 mm long capillary; however, within hours of operation, the housing melted due to the heat produced by the glow discharge.

Simmer discharge with no HV electrode isolation

In order to use the glow discharge for laser wakefield experiment, the capillary exit at the HV electrode needed to be unblocked. Two major problems needed to be addressed, however, in order for the glow discharges to be used: (i) the heat, created by the glow discharge, melted the housing, requiring a new design for the housing; and (ii) discharges from the HV electrode to the grounded chamber wall — mentioned earlier, and the reason why the HV side was blocked off — made it impossible to establish a glow discharge. In addition, these unwanted discharges pose a risk to all electronic equipment inside the vacuum chamber — for example motorized stages — and risked damaging them. The steps taken to remove both problems are outlined in the next two paragraphs.

Heat melts perspex housing. While the sapphire capillaries exhibited no damage, the perspex housing melted and unusable after several hours of use. This problem was addressed by using a different material for the body of the housing which could sustain temperatures

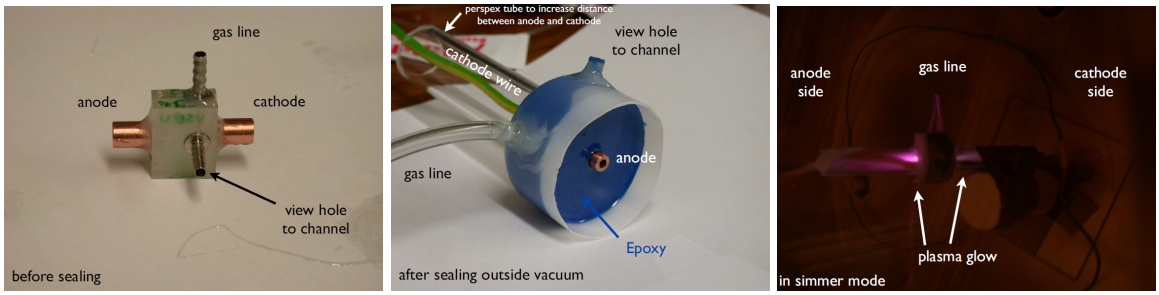

(a) (b) (c)

Figure 4.10: The prototype housing for the 15 mm capillary: (a) before epoxy was applied, (b) with epoxy applied, and (c) in operation in simmer mode inside the vacuum chamber.

of $T > 100\,^{\circ}\mathrm{C}$. The new housing prototype could both (i) deal with the heat by using an epoxy which did not melt and (ii) make it impossible for the discharge to strike through the housing by eliminating the gas load around the sapphire blocks. The latter was performed by connecting the gas slots directly with the gas supply, rather then having the housing filled with gas.

Discharge to grounded vacuum chamber. Two approaches were taken. (a) First the glow discharge voltage type was switched from negative to positive voltage. The reason for switching the polarity is that discharges of positive polarity are less aggressive and prolonged than discharges of negative polarity; that is because positive voltage requires an electron being created — for example by cosmic rays — between the HV electrode and the vacuum chamber, for an initial discharge to occur, and after this initial discharge no additional electrons are supplied, until a new seed electron is created randomly. Operating at negative voltage supplies the initial discharge with a constant reservoir of electrons and the discharge continues for longer and with higher currents. (b) The second approach was that a Faraday cage was used to shield the HV electrode. With the Faraday cage properly enclosing the HV electrode, only a single discharge over a period of several days of experiments was observed at a voltage of 12.4 kV. This discharge however did not leave the Faraday cage and, hence, electrical equipment in the vacuum chamber will not be affected.

After the two problems were eliminated, prototype housings were built. Fig. 4.10 shows the 15 mm prototype. In order to study the behaviour the simmer circuit was connected and tested in (i) pulsed gas supply mode and (ii) free-flow gas supply and the results are presented below.

Pulsed gas supply: only spark discharges were produced for simmer voltages of 6, 10 and 12 kV for capillaries length of 15, 50 and 100 mm, respectively. The pressure was varied between 50 mbar and 200 mbar but no stable glow discharge could be established.

Free-flow gas supply: stable glow discharges were established for pressures above 150 mbar and below 10 mbar. In the high pressure range, the glow discharges were initiated with DC voltages above 10 kV and a simmer current was established at 7 mA. Fig. 4.10 (c) shows the simmer mode in the 15 mm capillary in operation. Simmer currents below 10 mbar were of order ≈ 1 mA. These results are in agreement with the data presented for the glow discharge with an isolated HV electrode. For DC voltages below 10 kV, only spark discharges were observed. For pressures above 10 mbar and below 150 mbar, only spark discharges could be measured for any voltage applied.

Summary

In summary, a stable DC glow discharge was established in a 300 μm capillary with helium pressures below 10 mbar and above 150 mbar. The gas was free-flowed into the capillary via 650 μm diameter gas-slots and the glow discharge was started by voltages $V \geq 10$ kV and simmer currents of 7 mA were recorded for the high pressure range, and 1 mA for the pressures below 10 mbar. The HV electrodes were shielded by a Faraday cage, which protected electrical equipment in the vacuum chamber from potential discharges. A pulsed gas supply did not establish a stable glow discharge. Heat created by the simmer current is significant and material, used for the housing, needs to sustains temperatures of $T > 100\,^{\circ}$C.

The glow discharge — with the HV side blocked from the vacuum chamber — was combined with the pulsed circuit of the capillary discharge waveguide. In comparison to the pulsed discharge on its own, the combined circuit had several benefits: (i) the voltage of the pulsed discharge could be lowered; (ii) the main discharge pulse rose faster; (iii) the jitter of the main discharge pulse was reduced; (iv) the main pulse created less electrical noise; and (v) the repetition rates of consecutive main discharge pulses was raised.

The results described above are in agreement with publications. Glow discharges are used in capillaries for HHG experiments at a low pressure of 2-4 mbar Xenon gas by a group in Colorado [100, 103] at a few milliamperes. For higher pressures glow discharges in capillaries of 300 μm have not been reported to date.

4.1.5 Conclusions

In conclusion, the pulsed discharge was introduced and an investigation for improving the existing electrical discharge design was presented. The glow discharge in combination with the pulsed discharge improved the discharge design for pressures below 10 mbar and above 150 mbar.

Although it was found, that the use of a simmer current brought some significant advantages in terms of reduced timing jitter and lower voltage required for the main current pulse, the range of pressures over which it could be used, did not match those required for plasma accelerator experiments. Recent experiments of the group accelerated electrons in the range of 200 MeV - 600 MeV [1, 60] with pressures above 80 mbar and usually below 200 mbar. When these two ranges — (i) glow discharge improving current discharge design and (ii) electron beam production — are compared, there is little overlap between them. The remaining pressure overlap between 150 mbar and 200 mbar was deemed to small to give the upcoming Gemini experiment enough flexibility to scan the pressure parameter.

For pressures below 10 mbar, the goal of the Gemini experiment of GeV scale electron the capillary would only have been possible with capillaries of length ≥ 100 mm. The glow discharge employed was longitudinal and hence the distance between the electrodes grows linearly; this increases the initial voltage requirement to greater than 50 kV and was deemed too large. A transverse glow discharge — employed along the short axis of the capillary — could be investigated in the future. To complicate matters further, at pressures below 10 mbar, mechanisms for injection other than self-injection are required.

It is quite possible that future plasma accelerator experiments will indeed operate in this

low pressure regime, but at the time this work was undertaken, the immediate concern was the preparation for the up-coming experiment with the Astra-Gemini laser — the topic of chapters 5 and 6. It was decided that it was too risky to attempt acceleration in 100 mm long channels, using an entirely new design. Rather, it was decided to use the pulsed discharge design and improve some of its flaws via a redevelopment of its housing. This is the topic of §4.2.

4.2 Miniaturising of the existing waveguide housing

After an initial motivation, in this section, the individual improvements to the waveguide housing are outlined in §4.2.2 and photographs are displayed in §4.2.3.

4.2.1 Motivation

After it was clear that the pulsed discharge without the glow discharge would be used for the upcoming Gemini experiment, efforts were turned towards miniaturising the housing of the waveguide. The previously used housing was developed by Dr. Anthony Gonsalves for experiments at the Astra laser facility in 2007. The waveguide housing was designed to be part of the vacuum chamber, i.e. rather then being placed inside a large vacuum chamber, the housing formed part of the vacuum system, with vacuum bellows sealed to either end. It could be used in combination with the Astra target chamber at the Rutherford-Appleton Laboratory and the interferometry setup at Oxford University. Thomas Rowlands-Rees and Thomas Ibbotson used the design *within* a vacuum chamber, but essentially unchanged for their thesis experiments at the Astra and Astra-Gemini facility, respectively. The outer body of the housing was designed to accommodate capillaries of 15 -70 mm length. The housing was, therefore, always 120 mm long even when the actual capillary size was only 15 mm in length. The diameter of the housing was 90 mm to match the vacuum chamber diameter at the Astra target chamber.

Another reason to redesign the housing was that it accumulated a volume of gas inside the housing — along the transverse laser beam path and around the sapphire blocks — every time the capillary inside the sapphire blocks was filled with gas. This gas volume had to be pumped out through the capillary exits after each shot before another shot could be fired and slowed down the shot rate to 1 pulse every 10 s or less. This volume also created a path for the discharge to misfire *around* the capillary rather then *through* it. Glue and a steady hand were needed every time a new capillary was used to seal the o-rings adjacent to the electrodes to eliminate this discharge path.

The purpose of the development of the housing was to maintain the benefits of the previous housing — the ability to be used in the interferometry set-up *and* in LWFA experiments — while designing it small enough, so that two waveguides could be placed in series, allowing the potential for staged acceleration, and removing the disadvantages outlined above.

4.2.2 Development of the waveguide housing

Early development

For the first time, a 3-D printer was available to us during the development process. This was helpful in the very early stages of this development because (i) holding a real object and realizing the disadvantages missed on a computer screen is helpful; (ii) the lead time for a 3-D print is about one day compared to 1-2 weeks for a machined job; and (iii) the cost of the 3-D print is about 10 % compared to a machined job.

Removing gas around the capillary

As mentioned in the motivation section, having a volume of gas around the capillary creates the possibility of misfired discharges, that needed to be eliminated. The problem was avoided by designing the new housing differently in two ways: (i) the design was open, i.e. the sapphire blocks were open to the vacuum which removed any cavities in the housing where gas might have accumulated; (ii) using o-rings at the intersection between gas-slot and gas line. The o-rings were extra soft in order to allow them to seal well, but were also heat resistant, so they could sustain the heat endured by prolonged operation. Because of the two pronged approach to the problem, the waveguide was safe from misfiring: even if an o-ring leaked — an eventuality which never happened in our experiments — because of the open design, the escaping gas expanded into the vacuum and not in a confined space inside the housing. The possibility of misfiring the discharge was therefore completely removed. Because the o-rings were different from previously used ones, no glue was necessary.

Miniaturisation

An example 3-D view of the capillary housing, designed with the software AutoCAD, is given in Fig.4.11, where the assembled 33 mm short capillary holder with all its components is shown.

The holder is flanked by the electrodes — shown in copper colour — and the electrode holder, with the high voltage pin, is touching the electrodes. The electrode holder dimension along the laser axis was 15 mm. The total length of the housing along the laser axis was $33\,\text{mm} + 2 \times 15\,\text{mm} = 63\,\text{mm}$, approximately half the size of the design used between 2007 and 2010[2].

Fig. 4.12 shows outlines of both housings in a view along the laser axis (left) as well as from the top (right). In the plane perpendicular to the laser axis, the electrode holder extended 55 mm over the capillary entrance point. While this is 10 mm longer than in the old design — which had a circular design and a diameter of 90 mm — the extension only intruded on one side, while two[3] of the sides had an overhang of only 15 mm. This was

[2]Another design constructed in this effort reduced the length of the assembled holder to only 43 mm along the laser axis, which is an even greater reduction in that dimension. However since no plasma mirror or second waveguide was used in the experiment it was decided to increase the electrode holder by 10 mm to ensure its durability during the experiment.

[3]The forth direction away from the capillary entrance was blocked completely by the 5-axis stage which

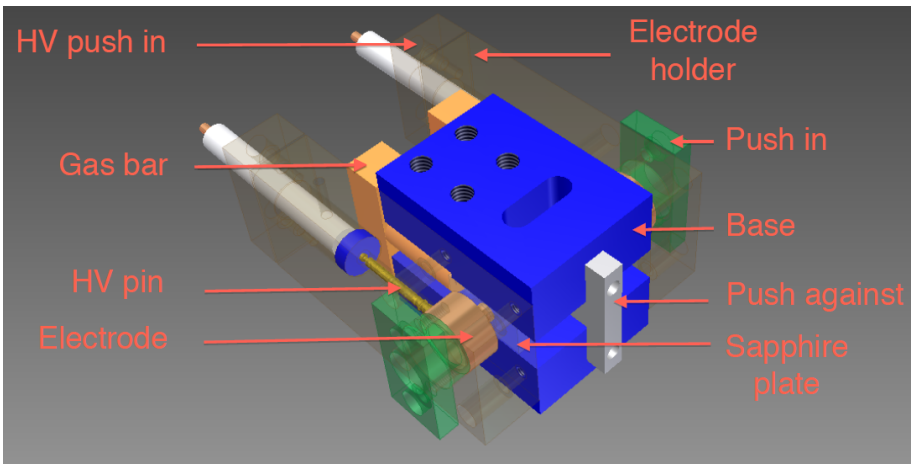

Figure 4.11: A 3-D view of the assembled 33 mm long capillary holder with all its components. The image was produced using the program AutoCAD.

a reduction of 67 %. This was one of the crucial points of the design, since it offered the possibility of introducing a plasma mirror close to the capillary entrance. This was further helped by the fact that — along the laser axis — the capillary entrance came 15 mm after the housing started. This distance was much longer (35 mm) in the older design.

The open design with o-rings around the gas line had another benefit: in previous designs, the first gas slot pointed upwards while the second gas slot pointed downwards (or vice versa). This mirrored design around the middle point of the capillary had to be done, in order to avoid discharges across the top of the sapphire blocks. Because there was no gas around the sapphire blocks in the new design, the gas slots could now be placed on one side of the capillary. This ensured that the gas lines, to both gas slots, could both be placed on the side of the electrode holder and hence intruding in an already blocked space. This left the opposite side completely free of gas lines, making it easy, for example, to translate the capillary housing out of the line of the laser beam. It is important to note, that the two individual gas lines, feeding into the two individual gas-slots, need to be at least ≥ 100 mm long, before linking up into a joint gas supply line connected to the gas bottle. This is to ensure, that no discharge occurs from (i) the HV electrode, (ii) through the closest gas slot, (iii) into the gas line, (iv) into the second gas line and gas slot, and finally onto the other electrode.

The new capillary holder was designed around the sapphire block space requirements. The sapphire blocks, making up the capillary, sit on a base, which has the same length as the sapphire blocks along the laser axis, and is custom made to each capillary length. All other parts of the housing are common and can be used for all capillaries, reducing the cost and time taken to manufacture the components. In the previous design, all but three parts were designed for a special length capillary.

Several small improvements were performed. (i) The HV pins were designed with springs which could be placed between the electrode holder and the HV pin. This was to ensure that the contact between the HV pin and the electrode was not lost due to small movement of the screws holding the HV pin holder in place. (ii) The connection between the HV pin

moved the capillary in the correct position.

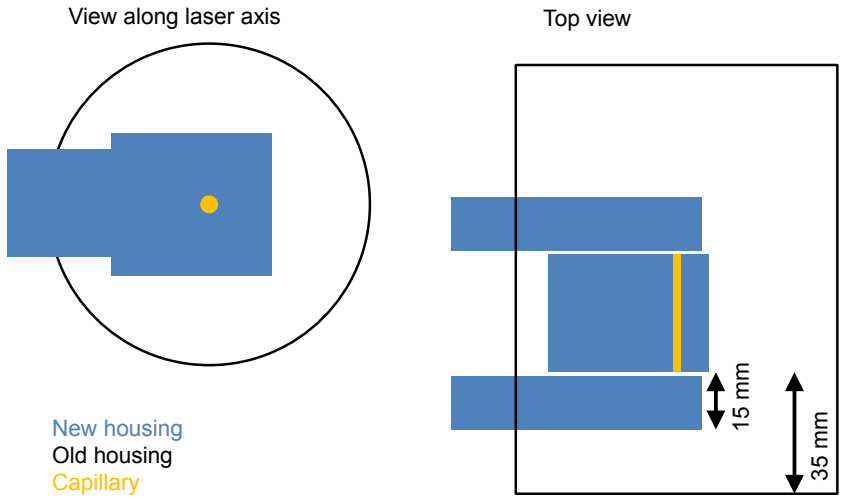

Figure 4.12: (Left) A view of the outlines of the old and new housing along the laser axis. (Right) The two housing outlines as seen from top.

and the cable delivering the current was not any longer soldered, but connected with a bolt and nut. This was done, because the old design would occasionally fail during experiments. (iii) Small items like gas connectors, converters, and o-rings where purchased from suppliers rather then self-designed in order to ensure quick and cheaper replacement in case of breakage. While that meant that the remaining self-made items had to be designed around already existing parts — a minor disadvantage — it also ensured, that the bought parts were already tested by the supplier. (iv) The metal screws were all replaced by nylon screws to eliminate any possibility of the discharging jumping across the housing. For higher temperature operation such as a glow discharge addition, the author recommends ceramic screws. (vi) The sapphire blocks were aligned to be capillaries weeks before the experiment and bound together by "Permabond superglue". This avoided screws, which used to both align the capillary and hold it in place.

4.2.3 Photographs and performance

Fig. 4.13 displays photographs of the new housing. These figures show the housing of a 33 mm capillary. The items made of perspex were ordered from a plastic design specialist while the copper items — and the sapphire capillary itself — were machined by the author.

The new housing performed very well during the Astra-Gemini experiment described in chapters 5 and 6. No disadvantages compared with the old housing were found, and many advantages were noted. These include the smaller mount — the housing is now very easy to move out of the laser beam — and it looks a bit “cooler". But more importantly, the changes set out to improve the housing and remove flaws — described in §4.2.2 — were all realised successfully.

(a) (b) (c) (d) (e) (f) (g) (h)

Figure 4.13: Photographs of the new housing on top of a Thorlab kinematic magnetic base.

Chapter 5

Astra-Gemini experimental set-up and analysis methods

5.1 Motivation

From the start of June 2011 to the beginning of November 2011, experiments were performed using the Astra-Gemini laser facility at the Rutherford Appleton Laboratory. The purpose of these experiments were to: (i) produce GeV scale electron beams; (ii) characterize the produced electron beams and transmitted laser light; and (iii) use these beams to create and detect radiation within the water window by passing them through an undulator. Complications with the laser and radiation safety shrank the proposed four weeks of beam time to a total of two usable days of data taking and, as a consequence, only the first two goals were achieved.

This chapter discusses the experimental set-up in §5.2 and the methods of the analysis in 5.3. The results from the experiment will be presented in chapter 6.

5.2 Experimental set-up

The Astra-Gemini laser is a dual laser beam Ti:sapphire laser system and has been described in detail elsewhere [104]. The two beams, labeled North and South, are compressed in separate compressors. Due to problems with the South compressor, which produced an asymmetric focal spot, and because of the significantly higher energy in the South beam compared to the North beam, the experiments were performed with the amplified South beam being compressed in the North compressor. This required the uncompressed beam to propagate through $\approx 1\,\mathrm{m}$ of air which could not be fully shielded against air currents, and this may have increased the shot-to-shot jitter in the on-target beam pointing. Pointing stabilisation systems such as those described by Genoud et al. [105] could have reduced this jitter. A stabilisation system is planned for the Astra-Gemini laser, but it was not ready to be used during the experiment. The experimental layout after the laser compressor is outlined in Fig. 5.1.

The description of the experimental set-up is divided in the following way: Astra-Gemini

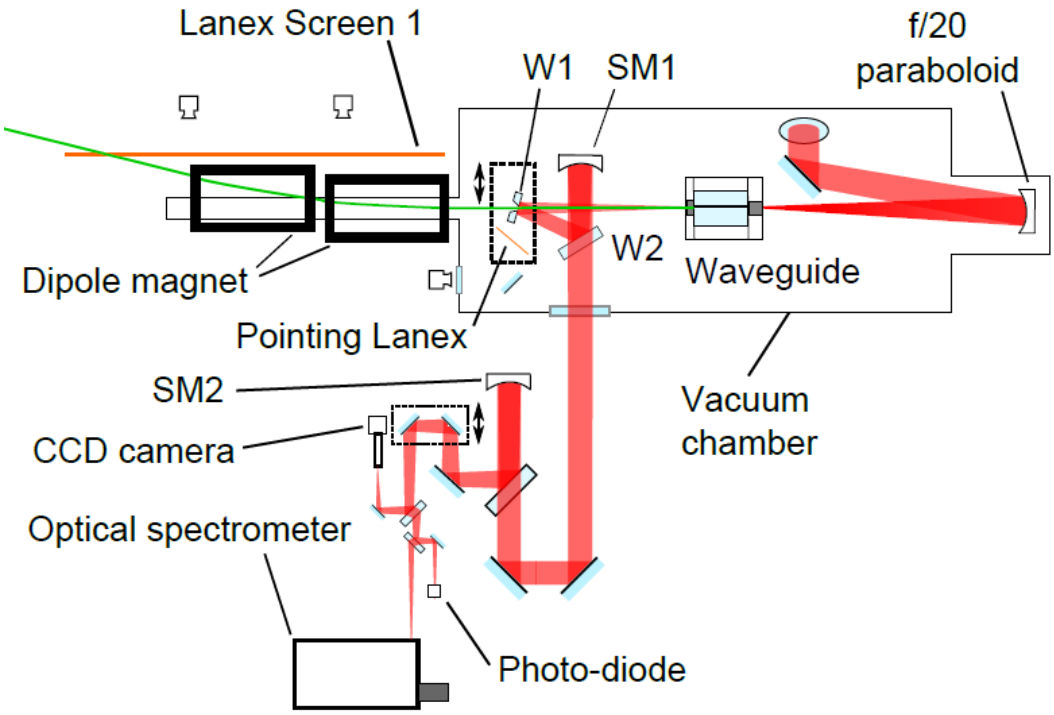

Figure 5.1: Schematic diagram of the experimental set-up employed in the experiments undertaken with the Astra-Gemini laser.

laser (5.2.1), waveguide (5.2.2), transmitted laser light diagnostics (5.2.3), and electron diagnostics (5.2.4). The software to acquire data was written by Dr. Nicolas Bourgeois and will not be discussed in this thesis.

5.2.1 The Astra-Gemini laser

For these experiments, the Astra-Gemini laser system delivered linearly-polarised pulses with a FWHM duration of $\tau = (55.3 \pm 1)$ fs. An off-axis paraboloid of f = 3 m focal length used at f/20 focused the laser pulses of 150 mm diameter to the entrance plane of the capillary waveguide. A soft aperture was placed in the beam, prior to the final laser amplifier to improve the focal spot quality, which reduced the beam diameter to 75 mm. The aperture increased the fraction of the energy contained within the half-peak-intensity contour of the focal spot and a detailed analysis of the laser spot is described in §5.3.1.

5.2.2 The waveguide

For these experiments the capillary discharge waveguide employed 33 mm long, 300 μm diameter capillaries laser-machined into sapphire blocks [102]. An image of the capillary and its support structure is shown in Fig. 5.2; a more detailed discussion of the housing was presented in chapter 4. The capillary was filled with hydrogen gas via two gas slots of 650 μm diameter located 4 mm from each end of the capillary. The plasma channel was formed by

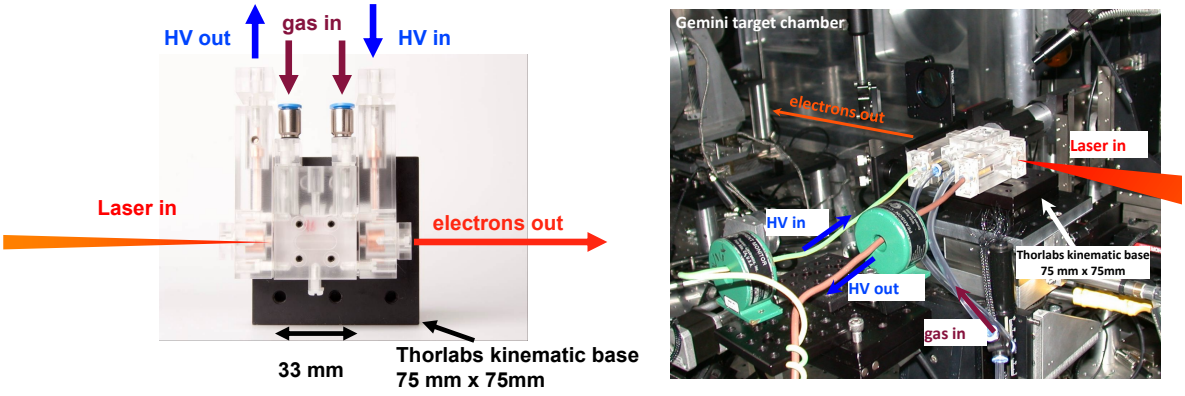

(a) (b)

Figure 5.2: (a) Annotated photograph of the waveguide and its housing on top of a Thorlab kinematic magnetic base. (b) Annotated photograph of the waveguide inside the target vacuum chamber of the target area. The gas and current flow in the gas supply lines and HV cables are indicated by arrows. The direction of laser and electron are also indicated.

a discharge pulse with a peak current of 500 A and 200 ns half period. The axial plasma density n_e at the centre of the capillary was determined from the scaling laws [79] deduced from interferometric measurements undertaken by a previous member of the group, Dr. Anthony Gonsalves, and was varied between $0.3 \times 10^{18}\,\mathrm{cm}^{-3} \leq n_e \leq 3 \times 10^{18}\,\mathrm{cm}^{-3}$.

5.2.3 Transmitted laser diagnostics

As shown in Fig. 5.1, a 102.6 mm diameter wedge ($W1$), in which a 20 mm diameter hole had been drilled at 45° to the normal, was placed approximately 1.6 m from the exit of the capillary and oriented at 45° to the propagation axis of the laser. Laser light transmitted through the capillary, was reflected from the front surface of the wedge onto a second wedge ($W2$) of 254 mm diameter and then to a spherical mirror ($SM1$) of focal length 2540 mm, arranged so as to retro-reflect and collimate the beam. The collimated beam passed through $W2$ and out of the vacuum chamber, and was refocused using a combination of a wedge and spherical mirror ($SM2$) equivalent to that used in the chamber to collimate the beam. Several diagnostics measured the properties of the transmitted laser radiation: (i) a CCD camera to image the transverse intensity profile of the laser in either the entrance or exit plane of the capillary (the object plane being determined by the position of $SM1$); (ii) a photodiode to measure the transmitted laser energy; (iii) an optical spectrometer to measure the spectrum of the transmitted laser light; and (iv) a GRENOUILLE to measure the temporal profile of the pulse.

Because space was limited on the optical table, the GRENOUILLE was placed on a different level and its beam path is shown in Fig. 5.3. The beam path was as follows: laser light reflected from $W1$ was intersected by a pick-off mirror (PM). A lens (L) made of fused silica was positioned between the mirrors $O1$ and $O2$ and focused the diverging beam. Between optics $O2$ and $O3$, the beam traversed upwards and a fused silica window (Wi) separated

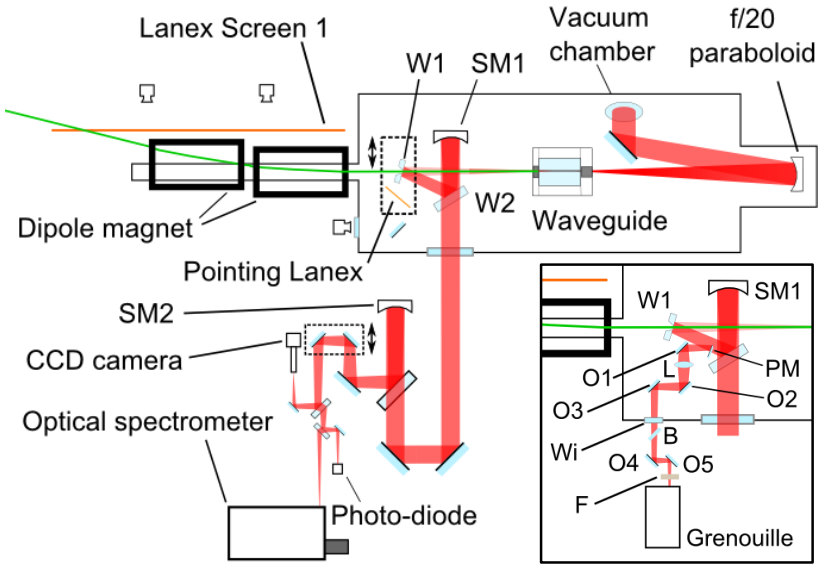

Figure 5.3: Schematic diagram of the experimental set-up. The insert shows in detail the optical layout of the optical components used to pick-off part of the transmitted laser beam and transport it to the GRENOUILLE. Note that the GRENOUILLE was located above the optical spectrometer and the pick-off beam was deflected vertically between $O2$ and $O3$. Some devices are removed in the insert in order to see the beam path of the GRENOUILLE clearly.

vacuum from air and allowed the beam to exit the vacuum chamber. A beam spitter (B) was also traversed by the beam before the beam entered the GRENOUILLE, which was protected by a filter wheel (F).

5.2.4 Electron diagnostics

Electrons accelerated within the plasma channel passed through the hole in $W1$ and entered the electron spectrometer, which comprised two permanent dipole magnets dispersing the electron beam. Each dipole magnet produced an average field of 0.78 T in a region 0.4 m (parallel to the laser axis) by 0.15 m (horizontal) by 0.04 m (vertical). The dipole magnets were separated by 0.05 m in the direction parallel to the laser axis; the second dipole was offset in the horizontal plane by 0.05 m to increase the path of high-energy electrons in the magnetic field. A field map of the magnetic field of one of the magnets is shown in Fig. 5.4. The field map was measured by a Hall effect probe in 2D within a 0.2 m × 0.075 m wide area, and the rest of the magnetic field was deduced from it. The deflected electron beams were detected by a Lanex screen of 1 m length, the phosphorescence from which was imaged by a pair of CCD cameras. These Greypoint Flea2 cameras were placed below the beam line to avoid radiation damage. They were equipped with wide-angle objectives in order to be placed close to the Lanex screen in order to maximize the light detection output, but also to limit the number of cameras to 2. Laser light and ambient light from the target area was prevented from entering the cameras objectives by bandpass interference filters with

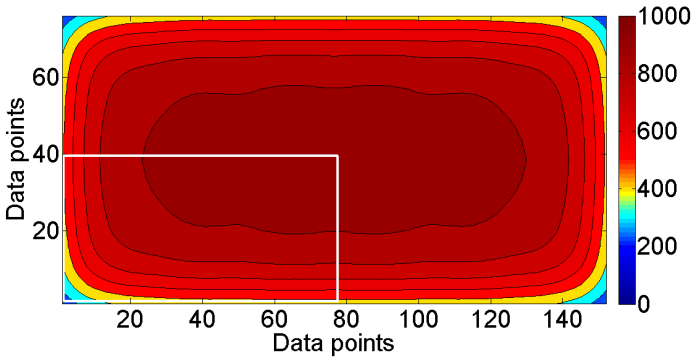

Figure 5.4: The magnetic field map of the first dipole magnet in units of mT. Only one section — indicated by the white line — was measured by a Hall effect probe in Munich and the rest of the magnetic field was deduced from it. Since the specification of the two magnets were the same, the magnetic field of the second magnet was not measured in detail. During the experimental set-up, several data points were taken within the second magnets field and they were within 2 % of the equivalent data point taken for the first magnet.

a centre wavelength of 550 nm and a bandwidth of 50 nm. All Lanex screens used in this experiment were Kodak Lanex Regular screens, which were introduced in chapter 3, where their linearity to increasing charge density was discussed.

As illustrated in Fig. 5.5, two dual-screen systems were incorporated to overcome potential errors in the measurement of the electron energy arising from variations in the pointing of the generated electron beams. In the first method, shown in Fig. 5.5 (a), $W1$ could be replaced by a thin Lanex screen (the “Pointing" Lanex). In Fig. 5.6, the set-up is shown including the wedge with the hole ($W1$). The “Pointing" Lanex comprised a Lanex screen (Kodak, Intensifying Screen Regular) oriented with its back facing the incident electron beam and covered by a 11 μm thick Al foil to block the laser light. Phosphorescence from the front of the “Pointing" Lanex was imaged by a CCD camera. Since the electron bunch is known to originate within a few μm of the centre of the exit plane of the capillary, the measurement of the position of the electron bunch in the plane of the “Pointing" Lanex yields the position and propagation vector of the beam as it enters the electron spectrometer. From this information, and the field map of the dipole magnets, the energy calibration of the spectrometer can be calculated for each laser shot.

Fig. 5.5 (b) shows the alternative arrangement for beam-pointing correction, in which the electron bunch position and propagation vector at the entrance of the spectrometer is deduced from the image of the dispersed electron beam recorded on two screens located *after* the dipole magnets [106, 107]. This method also yields all the information needed to deduce the position and propagation vector of the electron bunch as it enters the magnetic field, although different procedures are required for mono-energetic and broad-band electron spectra. For a mono-energetic beam, reconstruction of the incident beam path proceeds as follows. In this case, the beam produces a distinct spot on each screen, and since the beam trajectory in this field-free region is a straight line, the position and propagation vector of the beam as it leaves the magnetic field may be deduced. From this information, the trajectory through the magnetic field may be calculated for a given electron energy, and hence the apparent position and propagation vector of the electron beam in the exit plane

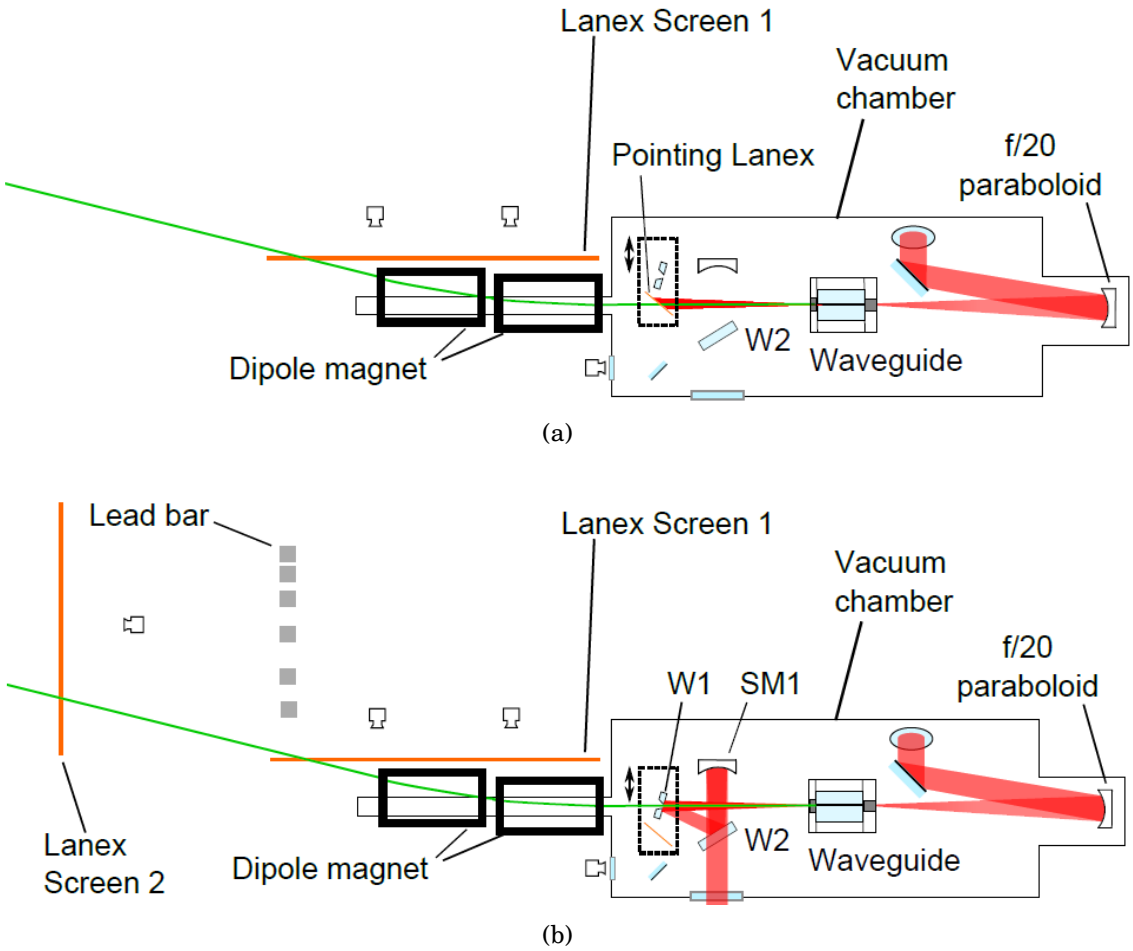

Figure 5.5: Sketch of the experimental set-ups of the electron spectrometer to correct for off-axis electron beam propagation using: (a) “Pointing" Lanex method; (b) the method using two screens behind the electron spectrometer.

of the capillary can be found. A retrieval algorithm then adjusts the energy of the electron beam until the position of the electron beam in the exit plane of the capillary is closest to the centre of the capillary; this yields the energy of the beam and the energy calibration of the spectrometer for that shot.

This approach cannot be used with broad-band electron beams since, in general, the energy spectra have no distinguishing features. To overcome this, lead bars were placed between the two Lanex screens in order to imprint holes in the energy spectrum recorded by the second Lanex screen [62] . The known locations of the lead bars and the measured positions of the spectral holes could then be used to calibrate the spectrometer using the same algorithm used for mono-energetic electron beams. Note that the (corrected) energy spectrum recorded by Lanex Screen 1 is unaffected by the lead bars.

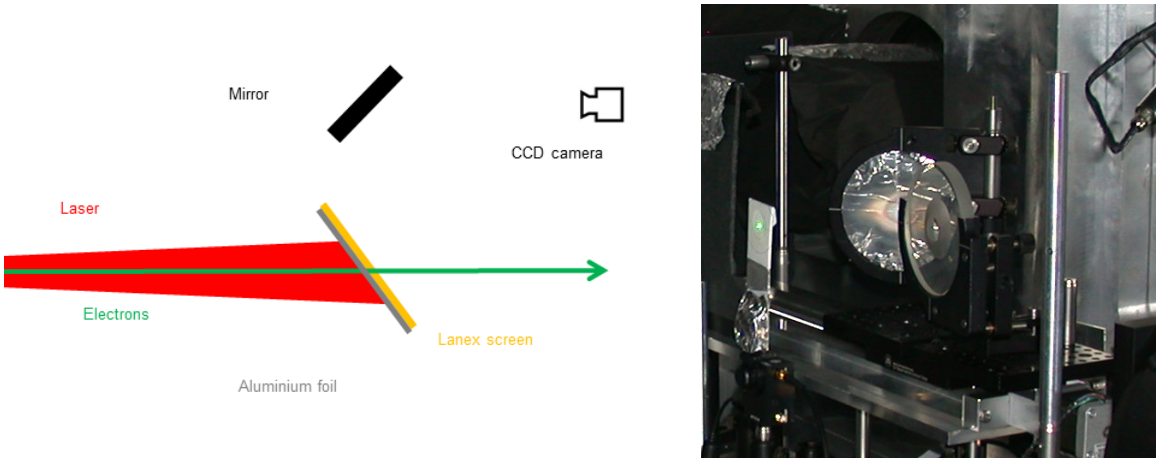

(a) (b)

Figure 5.6: (a) The set-up of the “Pointing" Lanex seen from the top with electron beam (green) and laser light (red) schematically shown. (b) The “Pointing" Lanex inside the Astra-Gemini target chamber. The wedge with a hole ($W1$) is also visible in front of the “Pointing" Lanex as well as an alignment card, which is illuminated by a green alignment laser.

5.3 Analysis methods

This section describes the methods of analysis and is divided in three sections: the analysis methods for the laser data are discussed in §5.3.1 incorporating the analysis of the quality of the focal spot and the laser beam pointing; §5.3.2 discusses the analysis methods for the transmitted laser data, which comprise the transmitted laser energy, the optical spectrum of the radiation and its temporal pulse length; finally, §5.3.3 discusses the analysis of the electron beam data which comprises sections on electron beam pointing, electron energy determination and correction and charge calibration.

5.3.1 Focal spot data

The transverse position and size of the Astra Gemini laser could be determined by an 8 bit Stingray F033 CCD camera placed within the target chamber. The CCD camera was moved into a position to image the focus of the laser beam when the waveguide was not in use. The percentage of laser energy within the lowest-order Gaussian mode is worth knowing because it is the energy within the FWHM of the focal spot that contributes to driving the plasma wave [108]. It is, therefore, important to gain the highest possible percentage of laser energy within the lowest-order Gaussian mode. The methods to determine the laser spot size, its quality and position are described in the following paragraphs.

Focal spot quality

A lowest-order Gaussian beam profile contains 50 % of its energy within the half-peak-intensity contour of the focal spot. The Astra-Gemini laser often exhibited a percentage of laser energy smaller than 30 % within the half-peak-intensity contour owing to the fact that the Astra-Gemini beam contained significant proportion of energy in higher-order trans-

verse modes. To improve the laser spot quality, a soft aperture was placed in the beam path in front of the final laser amplifier. This aperture reduced the laser energy by roughly one half, but the improved laser spot quality made this procedure worthwhile. Fig. 5.7 shows images of the focal spot with and without the aperture in place and shows that without the aperture aberrations in the focal spot were worse. In this example, the fraction of energy contained within the half-peak-intensity contour of the focal spot increased from 29 % without the aperture to 38 % with the aperture. One can also see, as expected, that the reduced diameter beam forms a larger focal spot.

To determine the percentage of laser energy within the half-peak-intensity contour, the following steps were taken: (i) the background level was determined by averaging the border pixel values of the original image and subtracting it from each pixel. Fig. 5.8 (a) shows the raw image with the background region indicated by two white dashed lines. (ii) The position and value of the peak pixel was determined. A square part of the image with borders of 50 pixel left, right, below and above the peak pixel was cut out for further analysis. Fig. 5.8 (b) shows the background subtracted image with the square part indicated by a white dashed line. (iii) Each pixel within the square image was analysed to be either above, or equal or below the half-peak-intensity value. (iv) The sum of the intensity values above the half-peak-intensity value was compared to the total intensity present in the square image and determined the percentage of laser energy within the full width half maximum of the laser spot.

Focal spot size

The FWHM focal spot size — defined as $W_0 = \sqrt{2}\sigma$, where σ is the radius of the laser beam at which the intensity in the laser pulse has dropped to $1/e$ of its peak value (§2.4.1)

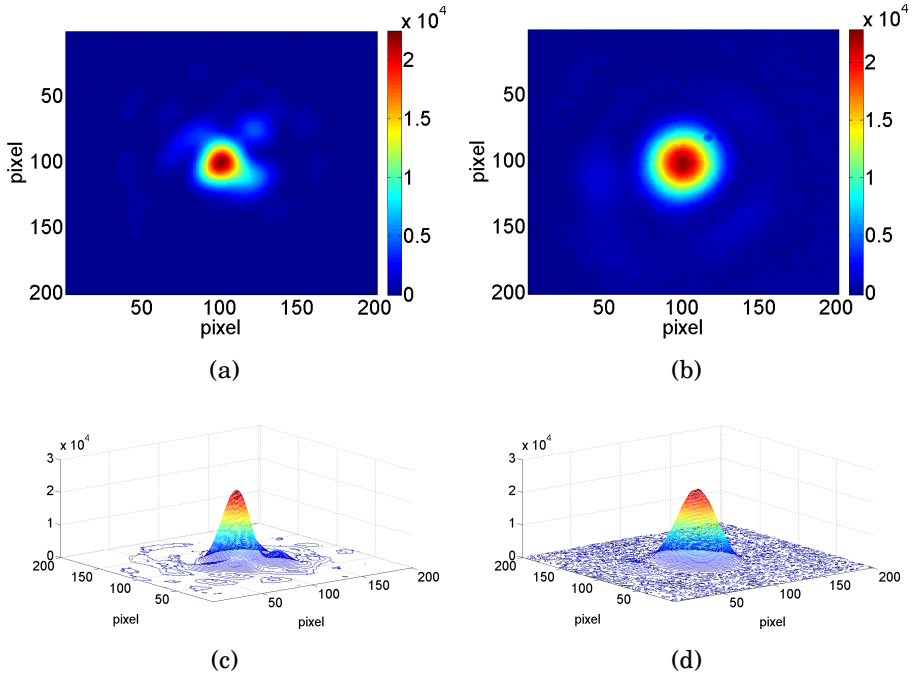

Figure 5.7: The laser spot recorded at focus without (a, c) and with (b, d) a soft aperture placed in the beam prior to the final amplifier.

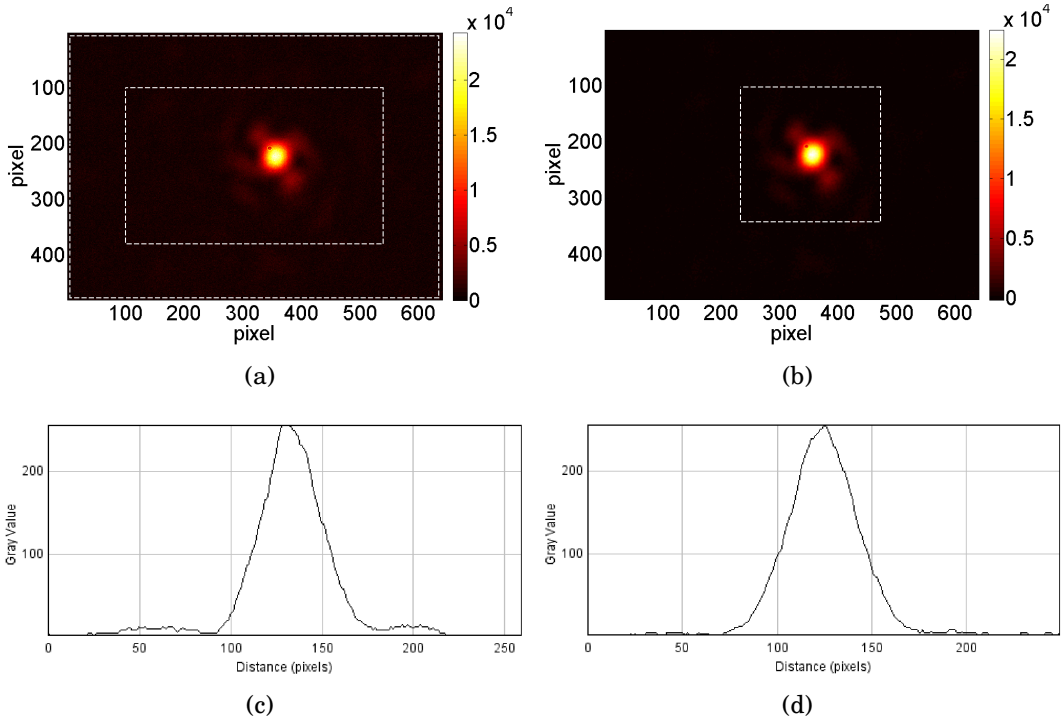

Figure 5.8: (a) Raw image of the laser focus obtained with the apodizer in position. The background region along the four edges of the image is indicated by white dashed lines. (b) The same image with the background subtraction applied; the region used to determine the percentage of signal above the half-peak-intensity is within the square region indicated by a white dashed line. The horizontal (c) and vertical (d) 1-D line-out profiles for the image shown in (b) are presented.

— was determined by taking horizontal and vertical 1-D line-outs across the background-subtracted focal spot image. The half-peak-intensity widths were 41.5 pixel in the horizontal direction and 42.1 pixel in vertical direction. Two calibrations were performed for the conversion from pixel to micrometre.

First, the pixel size of the Stingray F033 camera is specified to be 9.9 μm by 9.9 μm and the microscope objective was used under 10 fold magnification. This results in a spot size in the horizontal direction of $W_{0,H} = 41.5/10 \times 9.9\,\mu\text{m} = 41.1\,\mu\text{m}$ and $W_{0,V} = 42.1/10 \times 9.9\,\mu\text{m} = 41.7\,\mu\text{m}$ in the vertical direction, which results in an averaged spot size of $W_{0,1} = (41.4 \pm 1.1)\,\mu\text{m}$. Second, an airforce target [109] was used to calibrate the camera which resulted in a spot size measurement of $W_{0,2} = \frac{15.625\,\mu\text{m}}{16} \times \frac{41.5+42.1}{2} = (40.8 \pm 0.4)\,\mu\text{m}$[1]. Considering both results, this results in an averaged FWHM focal spot size of $W_0 = (W_{0,1} + W_{0,2})/2 = (41.1 \pm 0.9)\,\mu\text{m}$ with the error determined from the statistical error of both sub-results.

Focal spot pointing and drift

A data set of the focal spot images at low power was taken over a period of ≈ 1 hour several times during the experiment at a repetition rate of 0.05 Hz. The data set taken closest to when the electron data was collected is shown in Fig. 5.9 (a). The figure shows

[1]The camera imaged the first element of group 6 onto 16 pixel. This element contains 64 line pairs per millimetre which is equivalent to 15.625 μm per line pair.

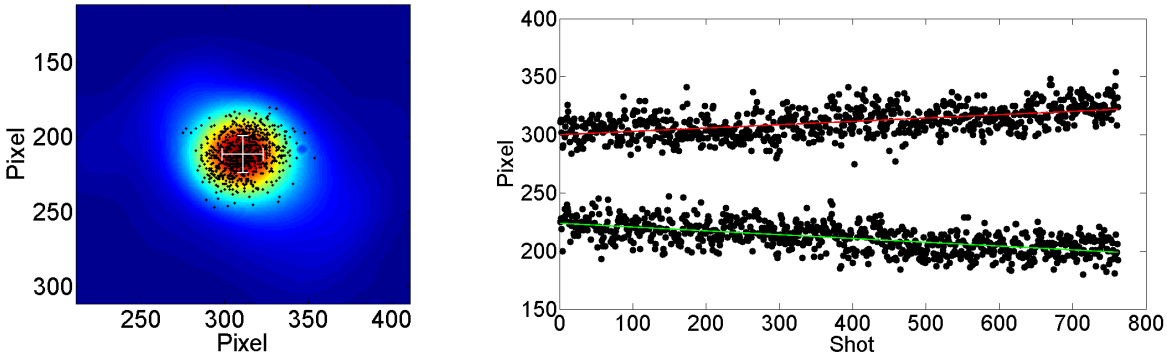

(a) (b)

Figure 5.9: Shot-to-shot variation of the position of the laser focal spot. (a) Positions of the peak intensity of each laser shot, superimposed over the transverse intensity profile of the sum of all the shots. The intensity peak of each shot is indicated (black dots). The white error bars indicate the standard deviation of the peak position. The focal spot of each image was moved towards the centre of the image before the sum was applied. The Stingray F033 camera had a pixel size of 10 μm and was used with a 10-fold magnification microscope objective. (b) Variation of the horizontal (top) and vertical (bottom) positions of the intensity peak as a function of shot number. Also shown are linear fits to the data, from which the drift rate was deduced.

the sum of the laser spot images and laser focus position, its pointing and drift. The rms variation of the shot-to-shot jitter in the transverse position of the input laser focus was measured to be 60% of the laser spot size or $\pm 24\,\mu$m. The long term drift of the peak position was 25 μm over a period of one hour. While the drift was relatively small in comparison with the laser spot size, the large shot-to-shot jitter ultimately forced us to use a capillary with a diameter of 300 μm, rather than a capillary with a diameter of 200 μm, which was originally planned.

5.3.2 Transmitted laser light

This section describes the methods used to determine the amount of transmitted laser energy via the photo-diode, its optical spectrum using the optical spectrometer, and its pulse length using a GRENOUILLE.

Transmitted laser energy

The laser light transmitted through the capillary was focused onto a photo-diode — called exit photo-diode—, which enabled the laser energy transmission of the plasma channel to be determined. The signal from the photo-diode was compared with a similar photo-diode — called input photo-diode — which was inserted earlier in the laser system beam path. The input laser energy on-target, calculated using the input photo-diode, was provided as part of the in-built diagnostics of the Astra-Gemini laser. An example trace of the signal from the exit photo-diode is shown in Fig. 5.10 (a). The signal from the exit photo-diode was captured by an oscilloscope and the value taken from the mean of the signal in a 200 μs window just after the measured peak was used. The energy transmission of the

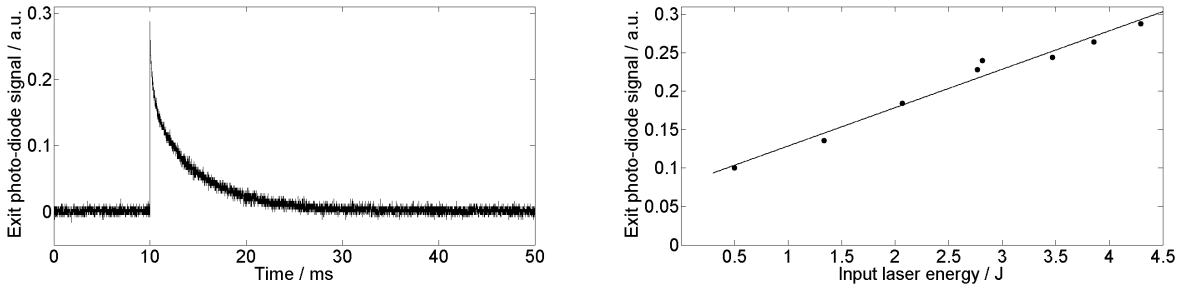

(a) (b)

Figure 5.10: (a) Example trace from the exit photo-diode that recorded the laser energy transmitted through the capillary. (b) The corresponding calibration curve used to calculate the transmission is shown.

capillary was calibrated as follows. First, with the waveguide removed, the signal recorded by the input photo-diode and the signal of the exit photo-diode were recorded as the laser pulse energy was adjusted by means of a half-wave plate. A calibration curve through these data was then fitted, as shown in Fig. 5.10 (b). This curve allows the exit photo-diode signal corresponding to 100 % transmission to be deduced for a given input photo-diode reading. Hence — with the capillary in place — the energy transmission is given by the ratio of the signal measured by the exit photo-diode to that corresponding to 100 % transmission. In terms of equations, this can be expressed as:

$$E_{\mathrm{i}}^{\mathrm{cal}} \cdot K = E_{\mathrm{m}}^{\mathrm{cal}}, \tag{5.1}$$

where $E_{\mathrm{i}}^{\mathrm{cal}}$ is the initial energy from calibration, K is a constant accounting for a loss of energy in the delivery system from laser room to interaction area, and $E_{\mathrm{m}}^{\mathrm{cal}}$ is the measured energy from calibration. The measured energy during experiments, E_{m}, is then equal to the input energy, E_{i}, times the factor K and the transmission factor T

$$E_{\mathrm{m}} = E_{\mathrm{i}} \cdot K \cdot T, \tag{5.2}$$

and T can be deduced from known quantities to be

$$T = \frac{E_{\mathrm{m}}}{E_{\mathrm{i}} \cdot K}. \tag{5.3}$$

Optical spectrometer data

Laser light transmitted through the capillary was focused onto the slit of an optical spectrometer. The spectrogram was recorded by a 16-bit Andor CCD camera from which the background was subtracted. The calibration of the wavelength and the sensitivity of the camera was performed before the experiment. It showed that the spectrometer was well calibrated and only needed correcting of order one nanometer. This minimal correction was thanks to another group using and calibrating the spectrometer just before the experiment of our group commenced. The white light correction was done using a Bentham 605 white light source and Fig. 5.11 shows the raw spectrum data for the white light calibration (a), the calibration curve (b), an uncorrected (black) and corrected example spectrum (blue) of the vacuum laser pulse (c).

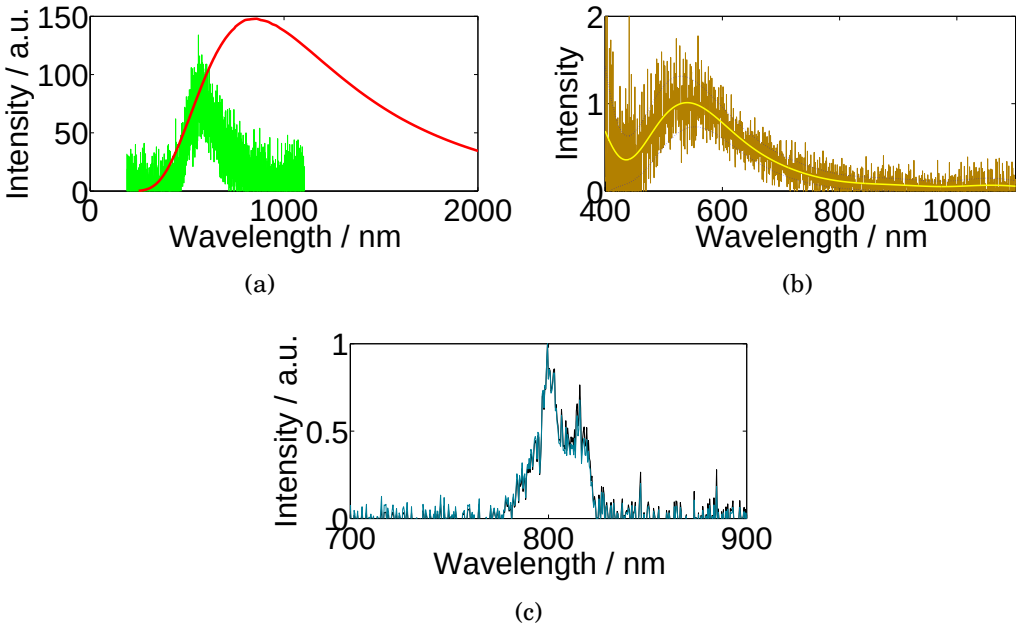

Figure 5.11: White light correction for optical spectrometer data. (a) The raw spectrum data of the white light calibration (green) as well as the calibration curve (red) for the Bentham lamp. (b) Calibration curve (yellow) and error estimate (blue). (c) The uncorrected (blue) and corrected (black) spectrum for a vacuum laser pulse.

Temporal laser pulse characterization

Key properties of the laser pulse are its temporal envelope and phase, or their equivalent in the spectral domain. To measure a period of time, a unit of time is required, which is shorter than the period being measured. Previous techniques to measure the temporal length of a laser pulse used an autocorrelation, which required splitting the pulse into two. The two beams can then be focused into a second harmonic generation (SHG) crystal, to create a non-linear signal, which is measured. This measurement is done with an array of time delays between the two pulses and enables the temporal pulse shape to be measured. By adding a spectral measurement to the time information, as was first suggested by Trebino and Kane [110, 111], the complete information, i.e. the pulse shape as well as the phase information as a function of time and frequency, can be measured. This measurement results in a spectrogram, referred to as a FROG[2] trace.

The complex optical set-up — due to the splitting and recombining of the laser pulses — is much simplified by the set-up of the GRENOUILLE[3] [112]. It replaces the beam splitters and delay lines with a single piece of optics, a Fresnel biprism, which splits the laser pulse into two beam-lets and crosses them at an angle [113] in a thick SHG crystal. The thick SHG crystal replaces the spectrometer by emitting different frequencies under different angles, which allows the detection along one of the axis of a CCD camera, e.g. the vertical axis. The horizontal axis of the CCD chip is used for the temporal measurement. An example FROG trace taken with the GRENOUILLE is shown in Fig. 5.12.

[2]The acronym FROG stands for Frequency Resolved Optical Gating.

[3]The acronym GRENOUILLE stands for GRating-Eliminated No-nonsense Observation of Ultrafast Incident Laser Light E-fields and is the French word for the English word *frog*.

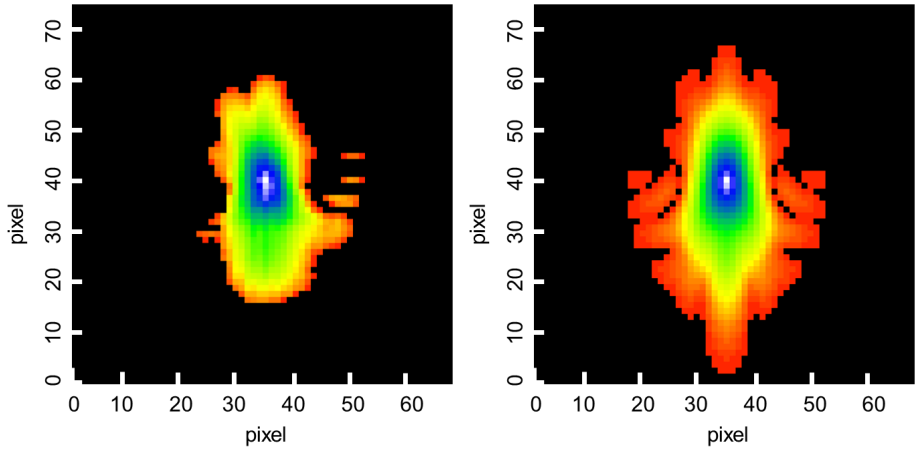

Figure 5.12: (a) Original FROG data taken during the experiment. (b) FROG trace reconstructed by FROG3 [114]. For both images, the horizontal axis is representative of time — although at this time during the analysis it is unknown in which direction time is progressing — and the vertical axis is representative of frequency.

To measure the temporal envelope and phase during the experiment presented here, a GRENOUILLE [112] with a resolution of 20 fs was used. A similar instrument, with a resolution of 10 fs, unfortunately broke during the experiment and its data could not be used. The GRENOUILLE data were analysed with the FROG3 software [114]. The algorithm grids the measured FROG trace and makes a first guess for amplitude and phase. It then compares its guess to the experimental FROG trace. The values at each point of the grid are varied until the error between the experimental and retrieved FROG trace are below 2 %, with the error defined as the square root of the sum of the squared differences in each pixel. Only data, for which a similar spectrum to the optical spectrum measured by the optical spectrometer was reconstructed independently, were used for the analysis.

It is important to note, that laser light, which was analysed for its temporal shape, was a small part of the whole laser beam profile, defined by the size of the pick-off mirror (Fig. 5.3), which reflected the light into the GRENOUILLE. Hence the temporal measurement can only reveal information about the temporal shape and phase of the pulse in this small part of the beam. Variation in the beam profile of frequency and pulse front tilt, cannot be accounted for. However, the staff scientists at the Astra-Gemini laser facility reduced pulse front tilt (PFT) before the experiment to below 3 fs, measured across the diameter of the beam of 150 mm. This suggests, that the measurement in regard to PFT is valid. Future experiment should rotate the position at which the pick-off mirror is inserted into the beam profile to eliminate the uncertainty of other variations across the laser pulse profile.

In an ideal world, the laser pulse would not traverse any material before entering the GRENOUILLE, because material dispersion would be incorporated into the GRENOUILLE measurement. However, the experiment required that the beam passed through 4 fused silica optics: (i) a lens (1.5 mm thick) to collimate the beam after it was picked-of by a small mirror; (ii) a window (1.5 mm thick) separating the vacuum chamber from air; (iii) a beam splitter (2.1 mm thick) used to divert some of the laser beam towards the 10 fs resolution

GRENOUILLE; and (iv) ND filters (0.1 mm thick) used to avoid saturation, placed 1 mm off the entrance of the GRENOUILLE.

The extra phase, introduced by these optics, needs to be corrected for. The Sellmeier equation [115] allows us to calculate the refractive index of the material, $n_{\mathrm{m}}(\omega)$, for each frequency and the phase shift introduced by an optic element can be written as

$$\Phi_{\mathrm{m}}(\omega) = \frac{\omega}{c} n_{\mathrm{m}}(\omega) \times l_{\mathrm{m}} \tag{5.4}$$

where l_{m} is the length of the optic the beam traverses. The additional phase the laser pulse picks up traversing the lens (L), window (Wi), beam splitter (B), filter (F) and 1 m of air is the sum of the phase shifts and can be written as

$$\Phi_{\mathrm{opt}}(\omega) = \Phi_L(\omega) + \Phi_{Wi}(\omega) + \Phi_B(\omega) + \Phi_F(\omega) + \Phi_{\mathrm{Air}}(\omega). \tag{5.5}$$

The phase the optics introduce is known to be positive. What is not known, however, is the sign of the measured phase, $\Phi_{\mathrm{measured}}(\omega)$. Hence the true phase $\Phi_{\mathrm{true}}(\omega)$ is either:

$$\Phi^{+}_{\mathrm{true}}(\omega) = \Phi_{\mathrm{measured}}(\omega) - \Phi_{\mathrm{opt}}(\omega) \tag{5.6}$$

or,

$$\begin{aligned} \Phi^{-}_{\mathrm{true}}(\omega) &= -\Phi_{\mathrm{measured}}(\omega) - \Phi_{\mathrm{opt}}(\omega) \\ &= -(\Phi_{\mathrm{measured}}(\omega) + \Phi_{\mathrm{opt}}(\omega)). \end{aligned} \tag{5.7}$$

An equivalent statement is that the sign of the spectral phase is not known and both possibilities have to be accounted for in the analysis.

The complex amplitude of each frequency multiplied by the corrected phase, $A(\omega) \times e^{-i\Phi_{\mathrm{true}}(\omega)}$, multiplied by $e^{-i\omega_0 t}$ results in the electric field and can then be Fourier transformed from frequency space into time

$$E(t) = \kappa \int_{-\infty}^{\infty} A(\omega) \times e^{-i\Phi_{\mathrm{true}}(\omega)} e^{-2\pi i \omega t} \mathrm{d}\omega \tag{5.8}$$

where κ is a constant. This reveals the corrected, temporal, complex amplitude $A(t) \times e^{-i\Phi_{\mathrm{true}}(t)}$ and hence the temporal intensity $I(t) = (A(t) \times e^{-i\Phi_{\mathrm{true}}(t)})^2 = A(t)^2$ can be deduced.

In Fig. 5.13, several steps in the process of correcting the phase are shown. In Fig. 5.13 (a), the retrieved spectral intensity (blue) and amplitude (cyan), and, in Fig. 5.13 (b), the retrieved spectral phase (blue) are shown. In Fig. 5.13 (c), the retrieved spectral phase is shown again (blue) with the additional phase pick-up from the lens, the window, and the beam splitter shown in red (large correction). The phase correction resulting from the pass through the filter and air is also shown in red (small correction). The corrected phase $\Phi^{-}_{\mathrm{true}}(\omega)$ due to these materials is shown in black. The other possible solution of the corrected phase, $\Phi^{+}_{\mathrm{true}}(\omega)$, is not shown. In Fig. 5.13 (d), the corrected (blue) and uncorrected (green) temporal intensities are shown. After making these phase corrections, the FWHM duration of the pulse intensity profile was found to be reduced from 75.3 fs determined by the raw GRENOUILLE measurement, to (55.3 ± 1) fs, where the error is the statistical error. The corrected value is in good agreement with an independent measurement made in the

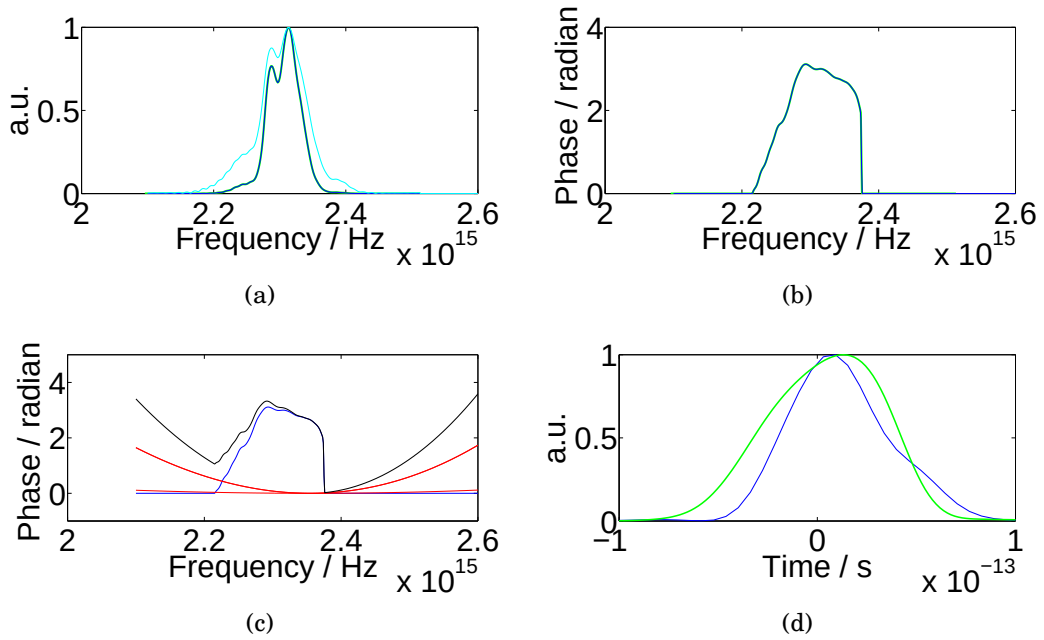

Figure 5.13: The correction process of the temporal phase of a vacuum pulse is shown. (a) The retrieved spectral intensity (blue) and amplitude (cyan). (b) The retrieved spectral phase (blue). (c) The retrieved spectral phase is shown again (blue) with the phase correction for the lens, the window, and the beam splitter shown in red (large correction). The phase correction for the filter and air is also shown in red (small correction). The beam phase after correcting for all the effect of these materials is shown in black. (d) The corrected (blue) and uncorrected (green) temporal intensities are shown.

laser area by the CLF laser engineers of $53-55\,\mathrm{fs}$. The other possible solution of the corrected pulse length — determined from $\Phi^{+}_{\mathrm{true}}(\omega)$ — resulted in a much longer pulse length measurement of $\tau > 85\,\mathrm{fs}$.

The ambiguity in the sign of the phase is easily removed in the case of the vacuum pulse because the pulse was independently measured to be $\tau \approx 53-55\,\mathrm{fs}$. Because it is independently measured, and hence the “correct" result is known before starting the analysis, the correct phase subtraction can be applied and hence the correct Wigner transform can be plotted. However, for pulses which were exposed to plasma, it is not known if the phase correction needs to be added or subtracted. This ambiguity was overcome using the idea described by Schreiber et al. [31]: by having placed material of known dispersion into the beam, the two possibilities could be distinguished by demanding that the Wigner transform of the laser pulse did not change significantly when the parameters of the experiment were changed slightly. For example, if the previous pulse exhibited positive chirp and changes in density were small, the pulse should still exhibit a positive chirp and the shape of the Wigner transform should not change drastically. The Wigner transform from the pulse exposed to plasma — either analysed with a (a) negative or (b) positive phase shift — which shows the smallest change compared to the vacuum pulse, is taken as the true result and the direction of time is determined.

5.3.3 Electron beam data

This section describes the methods used to analyse the electron beam data. First, the way in which the electron beam pointing and divergence are calculated is described, followed by a detailed description of the electron energy determination and correction, followed by a description of the definition of peak and maximum energy. Lastly, the method of the charge calibration is described.

Electron beam pointing

The “Pointing" Lanex screen was used to obtain information about electron beam pointing and divergence. As a reminder, either the "Pointing" Lanex or the wedge with a hole ($W1$) were in the beam path and, hence, only information about either the electron beam position or information about the transmitted laser light was possible, but not both simultaneously.

The white Lanex surface of the "Pointing" Lanex was marked with a black target cross which was aligned to the laser beam axis. This cross was visible on the CCD images and was

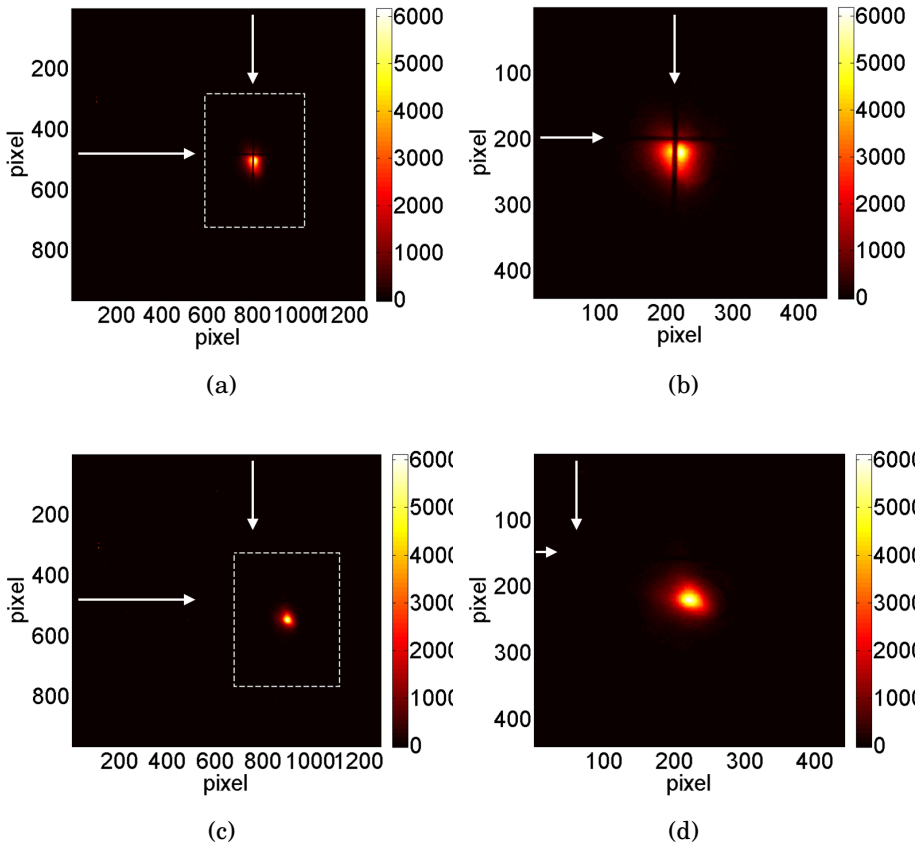

Figure 5.14: (a) CCD images from the “Pointing" Lanex showing an electron beam close to the design axis (indicated by a cross on the Lanex surface) with a close up shown in (b). (c) An electron beam further away from the design axis with its close-up shown in (d). The white arrows indicate the position of the cross which was positioned on the design axis of the laser beam.

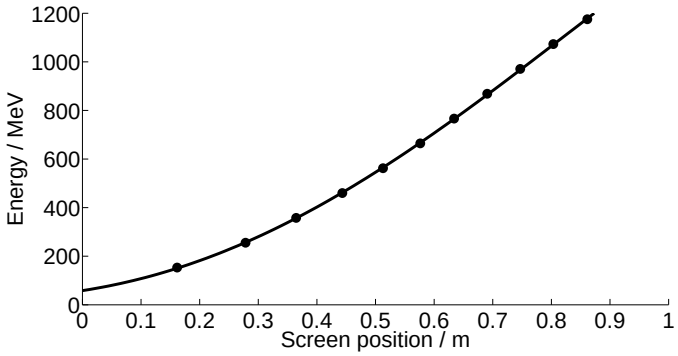

Figure 5.15: The data points (solid) and the fit (line) of the calibration curve for Lanex Screen 1 are shown.

used to determine the relative position of the electron beam intensity peak in the horizontal and vertical dimensions. Fig. 5.14 shows images of electron beams imaged on the "Pointing" Lanex. The top row shows an electron beam with a trajectory close to the design axis while the bottom row of Fig. 5.14 shows an electron beam with much greater off-axis pointing. The horizontal distance between the position of the cross and the position of the intensity peak of the electron beam, named p^{H}_{peak}, was translated into an absolute distance in unit of metre by the linear transformation $k_{m/p} \times p^{H}_{peak}$ where $k_{m/p} = 1.08 \times 10^{-4}$ m/pixel is the conversion factor from number of pixel to unit metre. The pointing result P^{H}_{mrad} in mrad was calculated using the following formula:

$$P^{H}_{mrad} = \arctan\left(\frac{k_{m/p} \times p^{H}_{peak}}{D}\right), \tag{5.9}$$

where $D = 1.559\,m$ is the distance between the exit of the capillary to the "Pointing" Lanex screen. The vertical pointing results were determined by an analogous procedure.

Electron beam divergence

The full-width half-maximum (FWHM) divergence of each electron beam was found by analyzing the shape of the electron beam intensity profile. The 2-D image was projected onto the horizontal axis to create a 1-D line-out. The full-width at half-maximum (FWHM) in pixels, Δp^{H}_{FWHM}, was converted into a divergence by:

$$\Theta^{H}_{radians} = 2 \times \arctan\left(\frac{1}{2}\frac{k_{m/p} \times \Delta p^{H}_{FWHM}}{D}\right). \tag{5.10}$$

The divergence in the vertical plane was deduced by an analogous procedure.

Electron energy determination and correction

A typical calibration curve of Lanex Screen 1 is shown in Fig. 5.15. The calibration curves were calculated with a MATLAB routine, taking into account the relative positions of the end of the capillary, the “Pointing" Lanex, the two dipole magnets, and the Lanex screen. The example calibration curve shown here, was produced for an electron beam of 500 MeV of energy and 3.1 mrad of beam pointing.

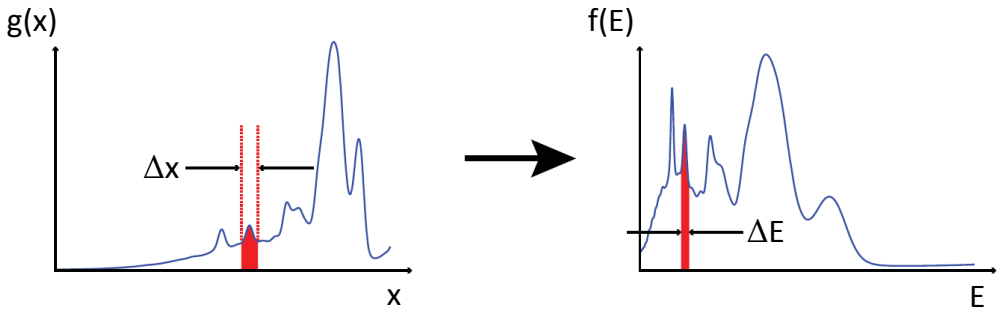

Figure 5.16: Schematic diagram of an arbitrary distribution showing how an electron distribution $g(x)$ in space is distorted as a function of energy $f(E)$.

This conversion from pixel value of the CCD camera to energy value of each pixel is performed in three steps: (i) transformation of the pixel value into the position x along the Lanex screen measured in metres, (ii) conversion of the distance x into electron energy using a polynomial, and, finally, (iii) weighting of the signal level in each energy bin. These steps are outlined below in detail.

The first and last pixel of the CCD camera along the horizontal axis, p_{min} and p_{max}, correspond to values in units of metre on Lanex Screen 1, $x^{\mathrm{L}}_{\mathrm{min}}$ and $x^{\mathrm{L}}_{\mathrm{max}}$. The field of view ($x^{\mathrm{L}}_{\mathrm{FOV}}$) is determined by subtracting the latter from the former. To translate each pixel value (p) into an absolute position on the screen in units of metre (x), the following transformation was performed:

$$x = p \times \frac{x^{\mathrm{L}}_{\mathrm{FOV}}}{p_{\mathrm{max}} - p_{\mathrm{max}}} + x^{\mathrm{L}}_{\mathrm{min}}. \tag{5.11}$$

A fourth-order polynomial of the form

$$E = \sum_{i=1}^{4} c_i x^i \tag{5.12}$$

was fitted to the spectrometer calibration curve to allow conversion of position x to the electron energy of that position.

After determining the absolute energy axis, the electron distribution measured in the space domain $g(x)$ must be re-weighted. This is required because the data recorded at even intervals in the space domain on Lanex Screen 1 are not mapped to even intervals in the energy domain. A distribution $f(E)$ has to be calculated in such a way, that the total electron count, integrated over the energy range ΔE corresponding to the interval in space Δx, is conserved. This is shown figuratively in Fig. 5.16. This condition requires that the sum over the spectrum in space equals the sum over the spectrum in energy

$$\int_{x_0}^{x_1} g(x)\,\mathrm{d}x = \int_{E_0}^{E_1} f(E)\,\mathrm{d}E, \tag{5.13}$$

and, hence,

$$f(E) = g(x)\left|\frac{\mathrm{d}x}{\mathrm{d}E}\right|. \tag{5.14}$$

Using equation (5.12), $dE/dx = 4c_4x^3 + 3c_3x^2 + 2c_2x + c_1$, and applying the scaling factor to each point of the spectrum yields the properly weighted electron distribution.

Fig. 5.17 shows an example using real data for the correction of the raw spectrum. In the left column (a, c, e, g, i), the low-energy camera image is described and, in the right-hand side (b, d, f, h, j), the high-energy camera image is described. For a good comparison of the two sides, in this example figure the high-energy CCD image was replaced with the low-energy CCD image to illustrate the different effect of the calibration curve on the low and high-energy part of the spectrum. The raw image from the CCD camera is shown in the top row (a, b), the intensity summed in the non-dispersed direction is shown in the second row as a function of pixel number (c, d), and the same distribution against position x using Eq. (5.11) is shown in the third row (e, f). The fourth row displays the spectrum as a function of energy using Eq. (5.12) (blue) as well as the re-weighted spectrum using Eq. (5.14) (green) (g, h). Note that the full-width at half-maximum value of the peak in the second row, which is 176 pixel wide on both cameras (c, d), corresponds to a width of 72 MeV along the low-energy screen (g), but an increased width of 132 MeV on the high-energy screen (h). Visually, this is better emphasized in the fifth row, in which the energy axis has the same limits for both screens (i, j). The reason is the non-linear behaviour of the polynomial (Fig. 5.15) in the low-energy region and the almost perfectly linear behaviour above 400 MeV. This almost perfectly linear behaviour of the polynomial for higher energies is the reason that the shape of the spectrum as a function of space (Fig. 5.17 (f)) is very similar to the shape of the spectrum as a function of energy (Fig. 5.17, (h) and (j)).

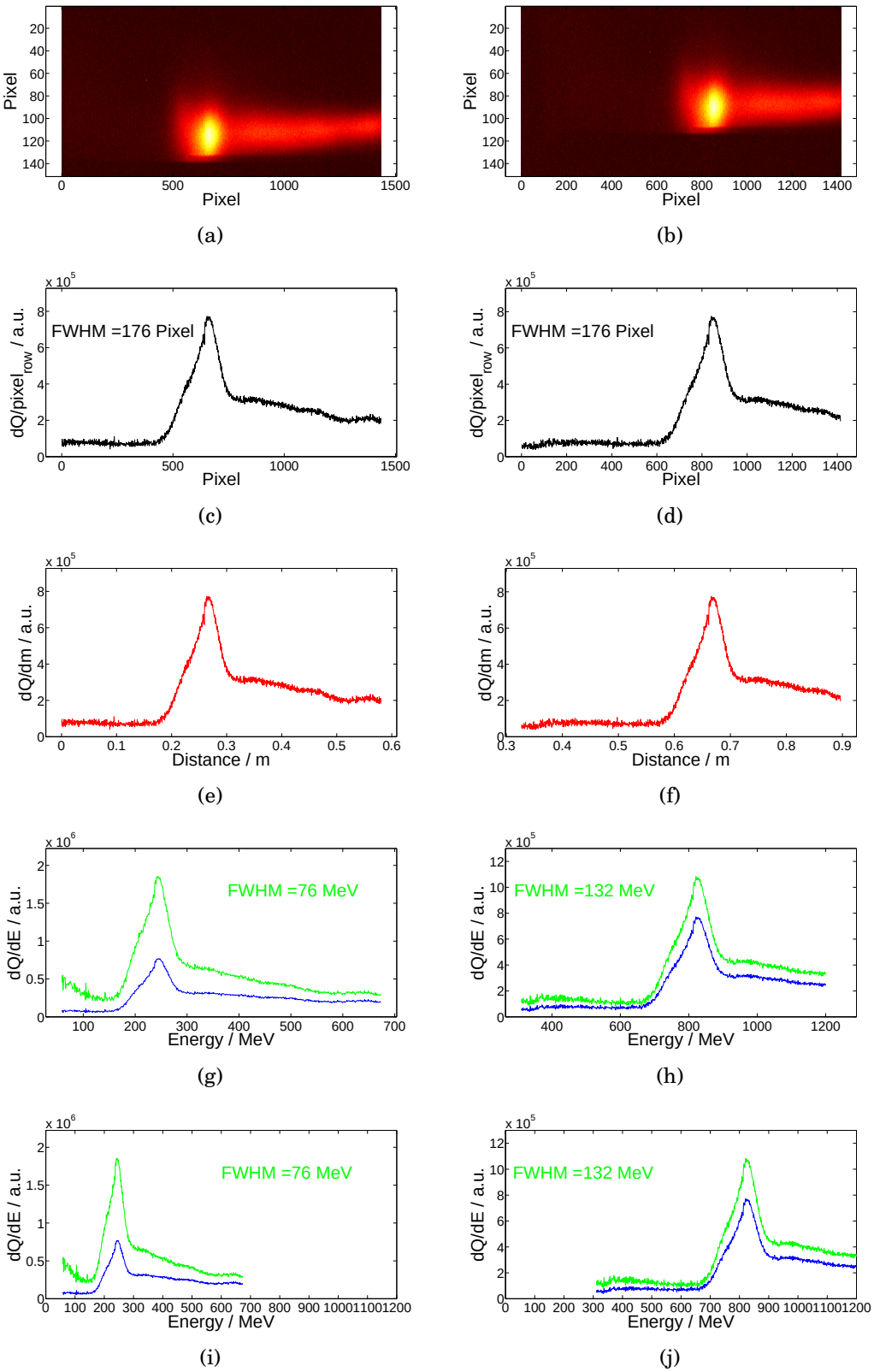

Figure 5.17: Conversion from pixel to energy for low (left column) and high (right column) energy camera. (a, b) The raw CCD image is shown. (c, d) The intensity summed in the non-dispersed direction as a function of pixel. (e, f) The same intensity distribution as a function of distance. (g, h) The distribution is shown as a function of energy un-weighted (blue) and re-weighted (green). (i, j) The same distribution as in row four with both column having the same axis limits.

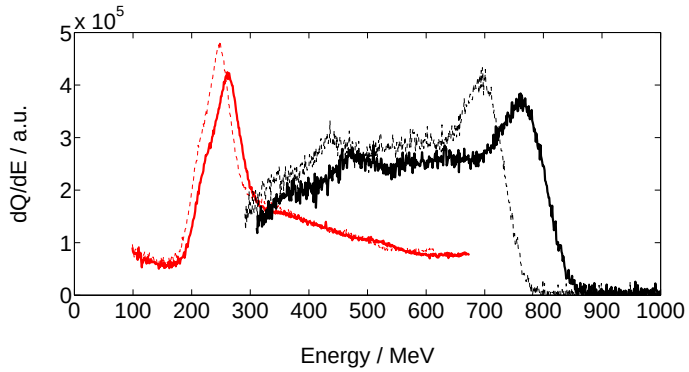

Figure 5.18: Examples of electron energy spectra recorded before (dashed) and after (solid) correction for off-axis propagation of the electron beam by the “Pointing" Lanex (black) and two-screen (red) methods on two separate shots.

An example of the energy correction determined by the “Pointing" Lanex method is shown in Fig. 5.18 (black lines). It can be seen that, in this case, correcting for the off-axis propagation of the electron beam increases the energy of the peak in the electron spectrum from 696 MeV to 765 MeV, an increase of 10 %. For other shots, the correction of the energy spectrum reduced the electron energies: for those shots yielding a positive energy correction, the average increase was 6.4 %; for those shots with a negative correction, the average decrease was 2.5 %. We note that this method was very easy to implement and, at least for these highly relativistic electron beams, scattering of the electron beam by the “Pointing" Lanex did not appreciably degrade the recorded energy spectrum on Lanex Screen 1.

Fig. 5.18 also shows an example of energy correction using the two-screen method (red lines); in this case the correction increases the energy of the peak by 7 % to 266 MeV. It is worth noting that for this method it was found that the total beam charge had to be above 20 pC in order for the spectrum recorded by Lanex Screen 2 to be measurable. Further, if the electron beam propagated at large angles to the system axis, it missed the second Lanex screen, preventing correction of the energy spectrum. We also point out that the two-screen method requires significant additional space — in our case approximately $1 \times 1\,\mathrm{m}^2$ — behind the dipole magnets, and hence overall this method is less convenient. On the other hand, for on-axis photon detection the two-screen method is necessary since otherwise the “Pointing" Lanex would block the radiation to be detected.

Treatment of background and X-ray hits

Background images for the low-energy camera and the high-energy camera were taken every day before data was taken. The background image was subtracted from the data image to produce the background subtracted image. Isolated maximum-value pixels — most likely from X-ray hits or broken pixels — were excluded from the images.

Definition of peak and maximum energy

The peak energy value was taken from the maximum value of the 2-D line-out of the Lanex spectrum. The maximum energy of the electron distribution was defined as the 2-D line-out signal falling to 25 % of its peak value, which was always well above background levels.

Electron beam charge calibration

The beam charge was calibrated using BAS-IP MS image plates made by FUJIFILM. The charge calibration was performed by exposing both Lanex Screen 1 as well as the image plate simultaneously to one electron beam. After this single exposure, the image plate was removed from the experimental area and analysed by an image plate reader. This procedure was repeated twice on a separate day, to create three independent charge calibrations.

The signal from the Lanex screen (N_{L}) was calibrated using the PSL reading from the image plate analysis. The three calibrations were consistent with each other and resulted in a charge reading of:

$$Q = N_{\mathrm{L}} \times 6.4^{-8}\mathrm{pC}. \tag{5.15}$$

A detailed description of how the image plates were calibrated is presented in chapter 3.

Chapter 6

Results from Astra-Gemini experiment

In this chapter, the results of the Astra-Gemini experiment are presented. The experimental setup and methods of data analysis for this experiment were described in chapter 5. The results presented here yielded two sets of data. The first was taken at a constant axial plasma density, to study the reproducibility of typical electron beams, and record values for beam pointing and divergence of the produced electron beams. In the second set of data, taken on a later day, the plasma density was varied from the very lowest density yet to produce accelerated electrons, up to the usual, higher plasma densities of previous experiments. This was done, to study the behavior of electron beam energy as a function of plasma density.

In §6.1, the parameters of the laser pulses and waveguide used for the results presented are discussed, before the properties of the accelerated electron beams are presented in detail in §6.2. The results for the temporal compression of the laser pulse due to plasma interaction are discussed in §6.3. Results are compared with simulations in §6.4 before the conclusions end the chapter.

6.1 Laser and waveguide parameters

The soft aperture, described in the previous chapter, was used for all the data presented in this chapter. The laser pulse energies, peak powers and intensities stated are the estimated on-target energy contained within the lowest-order Gaussian mode. With the aperture in place, the laser energy measurement after the compressor for the first data set was 4.2 J. Measurements of the laser spot quality recorded on that day showed, that only 38 % of that energy was contained within the half-peak contour of the laser spot. Of the 4.2 J incident on the target, therefore, only approximately $(0.38/0.5) \times 4.2\,\mathrm{J} = 3.2\,\mathrm{J}$ can be estimated to be contained within the lowest-order Gaussian mode. The transverse intensity profile of the focal spot was measured to have a full-width at half maximum (FWHM) of 41 μm at the entrance of the capillary. The temporal profile of the incident laser pulse was characterized with a GRENOUILLE [112] from which the full-width at half-maximum duration of the pulses were determined to be $\tau = (55.3 \pm 1)\,\mathrm{fs}$. Assuming an effective laser pulse energy of 3.2 J, the maximum incident peak power and focal intensity were $P = 55\,\mathrm{TW}$ and $I = 2.9 \times 10^{18}\,\mathrm{Wcm}^{-2}$, respectively. These laser pulse parameters, and the equivalent parameters

Table 6.1: Summary of the laser and waveguide parameters for both data sets.

		Data set 1	Data set 2
Laser beam parameters	Derivation		
Laser energy E / J	energy within FWHM	3.2	3.6
Focal spot W_0 / μm	FWHM	41	41
Temporal pulse length τ / fs	FWHM	55	55
Power P / TW	$0.94 \cdot E/\tau$	55	62
Intensity I / $10^{18}\,\mathrm{Wcm^{-2}}$	$2 \cdot P/0.84 \cdot W_0^{FWHM}$	2.9	3.2
Capillary parameters			
Length / mm		33	33
Diameter / μm		300	300
Axial plasma density (n_e) / $10^{18}\,\mathrm{cm^{-3}}$	scaling law [79]	2.2	0.3 - 3

for the second data set, are summarized in Table 6.1. The parameters of the capillary waveguide and plasma densities are also presented in the bottom half of the table.

6.2 Electron beam generation

As mentioned earlier, the experiment yielded two sets of data. The first was taken at a constant axial plasma density to produce typical electron beam spectra (§6.2.1), to record beam pointing and divergence (§6.2.2), and to find out how reproducible the produced electron beams were (§6.2.3). In the second set of data, the plasma density was varied over one order of magnitude to present the maximum electron energy as a function of the axial plasma density, and to compare it to theoretical models (§6.2.4, and §6.2.5). Finally, injections and acceleration at the lowest recorded axial plasma density will be discussed in §6.2.6.

6.2.1 Typical electron beam spectra

Electron energy spectra were recorded for a wide range of values of the axial plasma density, the laser energy, and the delay τ_D between the onset of the discharge and the arrival of the laser. From this initial survey, the optimum conditions for electron beam generation were found to be: an axial plasma density of $2.2 \times 10^{18}\,\mathrm{cm^{-3}}$ and the laser pulse timed to arrive at the plasma channel within (10.1 ± 2.8) ns of the peak of the discharge current. The laser parameter for data presented in §6.2.1 - §6.2.3 are summarized under the data set 1 section of Table 6.1.

Fig. 6.1 presents a typical electron energy spectrum recorded for these conditions, showing two distinct peaks at 512 MeV and 826 MeV. Double-peaked spectra of this type were observed on most shots. The mean peak energies and mean charges of these beams were obtained by fitting a double Gaussian distribution to all measured spectra with two peaks, and were found to be: for the lower-energy peaks, (511 ± 77) MeV and (9.2 ± 3.4) pC; for the higher-energy peak, (768 ± 56) MeV and (10.5 ± 3.6) pC. Dual-peak spectra of this form could arise either by trapping of electrons in two "buckets" of the plasma wave at different points

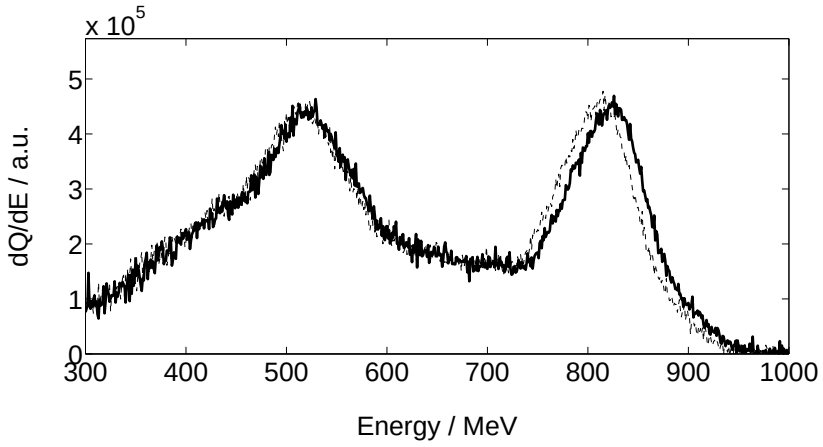

Figure 6.1: A typical electron spectrum recorded on Lanex Screen 1 which recorded electron energies $\geq 300\,\mathrm{MeV}$. The uncorrected spectrum (dashed) is corrected (solid) for off-axis electron beam pointing, but not for variations of the energy or pointing of the incident laser pulse. For this shot, the axial plasma density was set to $2.2 \times 10^{18}\,\mathrm{cm}^{-3}$, the laser pulse energy was 3.2 J, the maximum incident peak power and focal intensity were $P = 55\,\mathrm{TW}$ and $I = 2.9 \times 10^{18}\,\mathrm{Wcm}^{-2}$, respectively, and the laser was timed to arrive within $(10.1 \pm 2.8)\,\mathrm{ns}$ of the peak of the discharge current.

along the length of the plasma channel, or, by hybrid acceleration of the type considered by Hidding et al. [116], in which the first electron bunch drives its own wakefield, which can then accelerate a trailing electron bunch to a higher energy than the first bunch. Particle-in-cell simulations, which are more extensive than those presented in this thesis, should shed light on which of these mechanisms was responsible.

6.2.2 Beam pointing and divergence

Fig. 6.2 (a) shows the shot-to-shot variation of the position of 36 consecutive electron beams[1] indicated by black dots, as recorded by the “Pointing" Lanex. The positions are superimposed over the sum of the 36 CCD images, and the white error bars indicate the standard deviation of the peak position in the horizontal and vertical dimension. Fig. 6.2 (b) shows the drift of the peak position as a function of laser shot.

For the above mentioned laser and plasma conditions, the root-mean-square (RMS) variation of the beam pointing recorded by the “Pointing" Lanex was found to be 3.1 mrad; this is similar to previous experiments employing capillary discharges [1], steady-state-flow gas cells [28], and gas-jet targets [22], but large compared to the value of 0.57 mrad obtained with an intra-waveguide gas jet to control the electron injection [57]. Table 6.2 summarises some typical values that have been reported for the divergence and shot-to-shot pointing jitter.

The divergence of the electron beams could be measured in both the vertical and horizontal directions by the “Pointing" Lanex, and for the vertical direction by Lanex Screen 1 of the electron spectrometer. For the vertical direction, the two measurements were found

[1] These 36 shots are the same shots as described in §6.2.3.

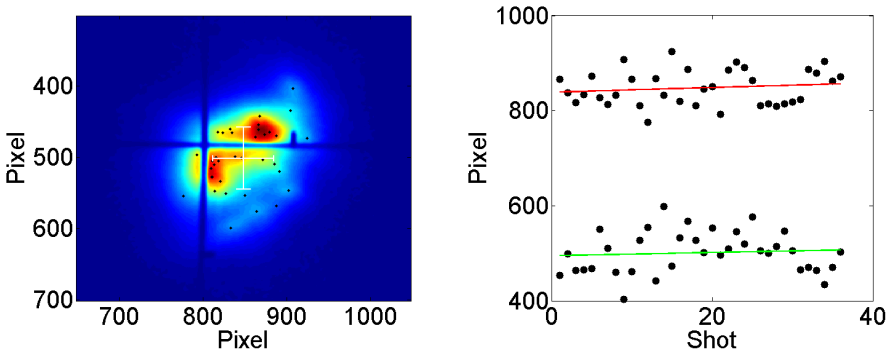

(a) (b)

Figure 6.2: Shot-to-shot variation of the position of the electron beam, as recorded by the “Pointing" Lanex. (a) The positions of the peak intensity of each electron beam is shown (black dots), superimposed over the transverse intensity profile of the sum of all the shots. The white error bars indicate the standard deviation of the peak position. (b) The variation of the horizontal (top) and vertical (bottom) positions of the intensity peak as a function of shot number is shown.

to be in agreement. The divergences measured by the “Pointing" Lanex were $\sigma_H = 3.6\,\text{mrad}$ and $\sigma_V = 3.4\,\text{mrad}$ for the horizontal and vertical planes, respectively, at a plasma density of $n_e = 2.2 \times 10^{18}\,\text{cm}^{-3}$. Note that the laser was polarized in the horizontal direction; previous work has shown [117] that the divergence of the electron beam can be larger in the direction

Authors	Method	Energy MeV	FWHM divergence mrad	RMS pointing mrad
This work	◎ S	991	3.5	3.1
Leemans et al. [17]	◎ S	1000	1.6 ∗	-
Kneip et al. [22]	⩒ S	800	3.6 ⋆	4.0
Ibbotson et al. [1]	◎ S	540	3.9 (h), 5.4 (v) ⋆	4.6 (h), 2.4 (v)
Gonsalves et al. [57]	◎⩒ D	341	2.5	0.6
Osterhoff et al. [28]	⊡ S	200	2.1	1.4
Pak et al. [27]	⩒ S	92	6.0 (h), 12.6 (v) †	-
Rechatin et al. [54]	⩒ C	72	5.0	-
Schmid et al. [58]	⩒ D	19	7.3	-

Key:

⩒	gas jet	S	self-injection
⊡	gas cell	C	colliding-pulse injection
◎	discharge capillary waveguide	D	density-ramp injection
∗	rms result	⋆	$1/e$ full-width result
†	$1/\sqrt{e}$ full-width result		

Table 6.2: Summary of LWFA divergence and beam pointing results for some selected papers. The referenced papers are displayed in order of decreasing electron energy. For single shot results and where pointing results were not reported, a dash is displayed.

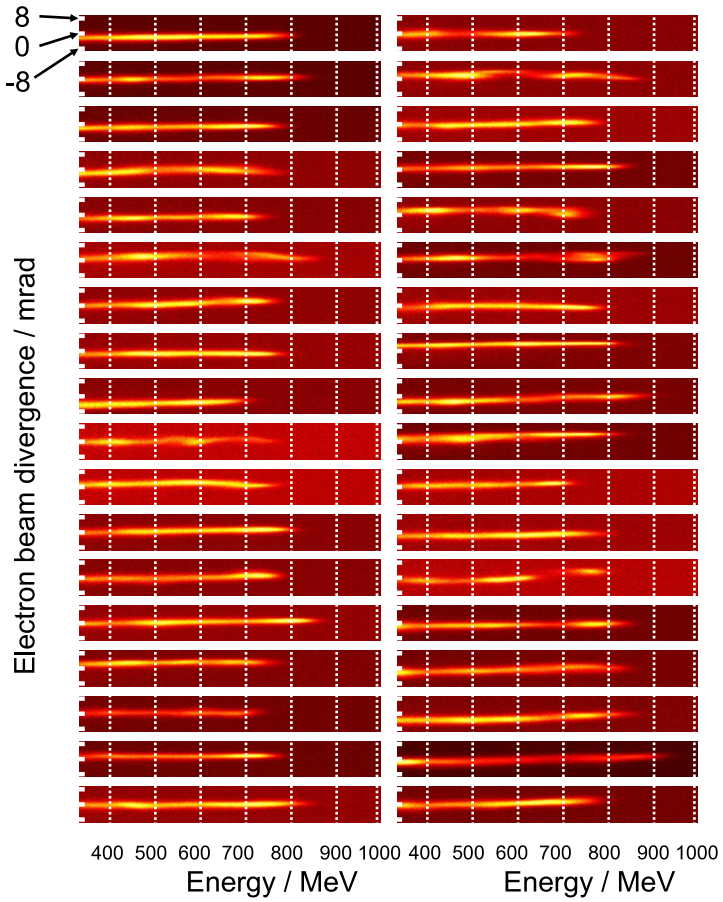

Figure 6.3: Electron spectra recorded on Lanex Screen 1 for 36 consecutive shots are shown. Consecutive shots are displayed from top to bottom with the left column displaying the first shot. These images were corrected for variations of the electron beam pointing but not for variations of the energy or pointing of the incident laser pulse. For these shots, the axial plasma density was set to $2.2 \times 10^{18}\,\mathrm{cm}^{-3}$, the laser pulse energy was 3.2 J, the maximum incident peak power and focal intensity were $P = 55\,\mathrm{TW}$ and $I = 2.9 \times 10^{18}\,\mathrm{Wcm}^{-2}$ respectively, and the laser was timed to arrive within $10.1 \pm 2.8\,\mathrm{ns}$ of the peak of the discharge current.

of the electric field of the driving laser as a result of interaction of the accelerating bunch with the tail of the laser pulse. For these conditions, the plasma wavelength λ_p is not large compared to the length of the *input* laser pulse, $c\tau = c \times 55\,\mathrm{fs} \approx 17\,\mu\mathrm{m}$, and hence it might be expected that the electron beams would have a larger divergence in the horizontal plane. That this is not observed, suggests, that the laser pulse duration decreases during the long laser-plasma interaction [31]; this conclusion is supported by the fact that, for this density, the duration of the *transmitted* laser pulse was measured to be 24 fs. A detailed study of temporal pulse compression is presented in §6.3.

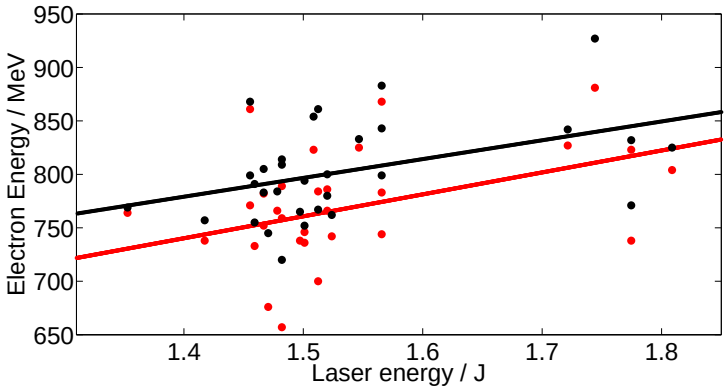

Figure 6.4: The maximum (black) and peak (red) electron energy as a function of the laser energy within the FWHM of the laser spot. The solid lines are linear fits to the data points. For 5 of the 36 laser shots, the laser control software reported an incorrect laser energy of 0 J; these data were excluded from the above figure.

6.2.3 Reproducibility

The reproducibility of the generated electron beams was studied by recording the electron energy spectra for 36 consecutive shots with the same timing and initial gas pressure. Fig. 6.3 shows images of the Lanex Screen 1 for these shots, illustrating that high-energy electron beams were generated on every laser shot with similar electron energy spectra. The spectra have been corrected for variations in the electron beam pointing using the “Pointing" Lanex method described in §5.2.4. However, the spectra have not been corrected for shot-to-shot jitter in the transverse position of the input laser focus, the RMS variation of which was measured to be 60 % of the laser spot size, or for the laser pulse energy, which had a RMS variation of 7.3 %. Fig. 6.4 shows the variation of the maximum and peak electron beam energy as a function of laser pulse energy for these 36 shots showing that, as expected, the electron beam energy increases with the laser pulse energy. A linear fit to the maximum energy data points yields $\mathrm{d}E_{\mathrm{electron}}/\mathrm{d}E_{\mathrm{laser}} = (176 \pm 47)\,\mathrm{MeV\,J^{-1}}$, and, therefore, from the measured standard deviation of the laser pulse energy, $\sigma_{E_{\mathrm{laser}}} = 0.29\,\mathrm{J}$, the variations in the maximum electron energy arising from the jitter of the laser energy is expected to be approximately $\sigma_{E_{\mathrm{laser}}}\mathrm{d}E_{\mathrm{electron}}/\mathrm{d}E_{\mathrm{laser}} = (50 \pm 14)\,\mathrm{MeV}$. This is comparable to the observed standard deviation of the maximum electron energy $\sigma_{E_{\mathrm{electron}}} = 46\,\mathrm{MeV}$. For the data shown in Fig. 6.3, the relative RMS of the total measured electron charge was $\sigma_Q/\langle Q\rangle = 35\,\%$. Variations in the pointing of the laser pulse will have caused additional variations in the energy spectra and charge of the accelerated bunches. It therefore seems likely, that the observed shot-to-shot variation of the properties of the electron bunches largely arises from shot-to-shot jitter in the laser parameters.

While previous experiments have achieved higher energies, and some have achieved higher reproducibility, it is worth noting, that the presented electron spectra of the 36 consecutive shots are the most reproducible assembly of electron beams at this high energy up to date. The higher control of electron production and reproducibility was achieved, in part, via a strong control over the laser, plasma and capillary parameters.

6.2.4 Electron energy scaling

A second set of data was taken to record the electron energy as a function of axial plasma density. This data set was taken on a different day than data presented previously in this chapter. In comparison to data set 1, data set 2 had several differences: (i) the laser energy, power, and intensity was 12.5%, 12.7%, and 10.3% higher, respectively; (ii) while the total laser energy was higher, the percentage of laser energy within the FWHM was 25% lower; (iii) the transmitted laser energy was 28% lower; and finally (iv) while the same capillary for the previous data set was used, the capillary was, therefore, not new, although no visible damage to the entrance and body of the capillary was observed prior to the start of the second data set. The combination of these four factors explain why the electron energy spectra are different for the two data sets, even though they had the same plasma conditions.

The maximum recorded energy ($W_{\rm max}^{\rm m}$) as a function of the axial plasma density $n_{\rm e}$ is shown in Fig. 6.5. For these shots, the laser pulse energy within the lowest-order mode was 3.6 J, the maximum incident peak power and focal intensity were $P = 62\,$TW and $I = 3.2\times10^{18}\,{\rm Wcm^{-2}}$, respectively, and the laser was timed to arrive at the peak of the discharge current. Acceleration is observed in three regimes [1,43] defined by the ratios of the peak power P of the driving laser pulse to the critical power for relativistic self-focusing, $P_{\rm c} = 17.4(\omega_0/\omega_{\rm p})^2$GW and the critical power for self-guiding, $P_{\rm c}^{\rm diff} = (1/8)(\omega_0/\omega_{\rm p})^{6/5}P_{\rm c}$. These regimes are: (i) at high plasma densities $P > P_{\rm c}^{\rm diff}$, so the plasma channel plays little role in guiding the laser pulses, (ii) a hybrid regime for which $P_{\rm c} < P < P_{\rm c}^{\rm diff}$, and lastly, (iii) a low-density regime in which $P < P_{\rm c}$ and, hence, only the plasma channel can guide the laser pulse.

The expected [43] electron energy after acceleration over one dephasing length, $W_{\rm max} = 2/3\ (m_{\rm e}c^2/e)\ a_0\ (\omega_0/\omega_{\rm p})^2$ is shown in Fig. 6.5 and assumes a value of a_0 corresponding to: (i) the initial input laser pulse energy (dotted, red curve) and (ii) relativistic focusing to the matched spot size $w_{\rm sf} = 2k_p^{-1}\sqrt{a_0}$ (solid, red curve), corresponding to $a_0 = a_{\rm sf} = 2(P/P_{\rm c})^{1/3}$. It can be seen that for $n_{\rm e} \gtrsim 7\times10^{17}\,{\rm cm^{-3}}$, the measured maximum electron energy lies between these two, red curves. The fact that the measured energies lie above those predicted for the input a_0 demonstrates that, in this regime self-focusing and pulse compression increase the peak vector potential above the input value. That they lie below the energies expected for $a_0 = a_{\rm sf}$ is consistent with coupling losses into the plasma channel and a loss of laser energy to the plasma wave. Also shown in Fig. 6.5 is the variation of $W_{\rm max}$ after the laser pulse energy is reduced by the measured energy transmission and allowing for relativistic self-focusing (solid, black curve). It can be seen that this simple correction to the expected maximum electron energy significantly improves the agreement with the measured data.

The variation of $W_{\rm max}^{\rm m}$ in Fig. 6.5 exhibits a clear optimum plasma density, $n_{\rm e}^{\rm opt} \approx 0.8\times10^{18}\,{\rm cm^{-3}}$, at which electrons with energies up to $991^{+30}_{-67}\,$MeV are observed. This optimum plasma density may be understood as follows: for high plasma densities the length of the plasma channel $L_{\rm c}$ is longer than the dephasing length, and, in this regime, $W_{\rm max}^{\rm m}$ will be attained by those electrons trapped in the plasma wave approximately one dephasing length from the capillary exit. Decreasing the plasma density from high values will increase the output electron energy (Eq.(2.33)), as observed, until the plasma density corresponds to $L_{\rm c} \approx L_{\rm d}$. As shown in Fig. 6.5 (vertical red line), this condition occurs for plasma densities close to $n_{\rm e}^{\rm opt}$ and the highest electron energies are obtained for slightly larger plasma densities, which makes sense, if at these densities, electron injection occurs a short distance after the

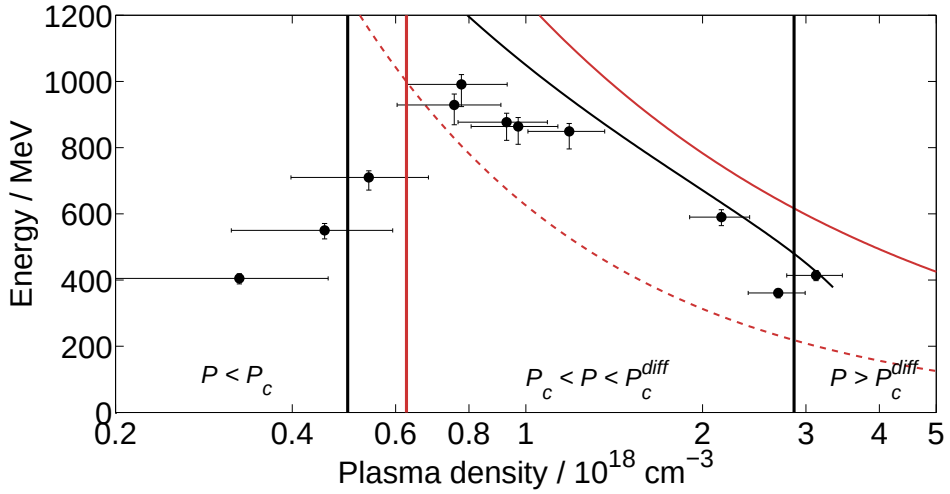

Figure 6.5: The maximum recorded electron energy ($W^{\mathrm{m}}_{\mathrm{max}}$) as a function of the axial plasma density. The density for which the dephasing length equals the capillary length is shown by the vertical red line (equation (2.28)). The three different regimes ($P > P_{\mathrm{c}}^{\mathrm{diff}}$ (equation (2.18)), $P_{\mathrm{c}} < P < P_{\mathrm{c}}^{\mathrm{diff}}$, and $P < P_{\mathrm{c}}$ (equation (2.16))) are separated by vertical solid black lines. The dashed red line (equation (2.34)) shows the expected electron energy after acceleration over one dephasing length, assuming a laser pulse with an energy of 3.6 J within the lowest-order mode; the solid red line is the energy gain assuming the laser self-focuses to the matched spot size in the bubble regime [43] (also (equation (2.34)). The solid black line represents the energy gain when the transmission of laser energy through the capillary is accounted for as well as self-focusing of the laser pulse (also equation (2.34)). For these data, the laser pulse energy within the lowest-order mode was 3.6 J, the maximum incident peak power and focal intensity were $P = 62\,\mathrm{TW}$ and $I = 3.2 \times 10^{18}\,\mathrm{Wcm}^{-2}$, respectively, and the laser was timed to arrive at the peak of the discharge current. The energy error bars result from the unknown pointing of the electron beam (the pointing-correction systems were not in place when these data were taken), which was assumed to be $\pm 3.1\,\mathrm{mrad}$, i.e. equal to that earlier measured with the “Pointing" Lanex. The pressure error bars result from the measurement error of the pressure which are of order millibar.

start of the plasma channel. As the plasma density decreases below the optimum value, both the accelerating electric field and the ratio of the capillary length to L_{d} will decrease, and as a result, the electron energy will decrease from that obtained when $L_{\mathrm{c}} \approx L_{\mathrm{d}}$.

6.2.5 Energy scaling at different laser parameters

In Fig. 6.6, $W^{\mathrm{m}}_{\mathrm{max}}$ as a function of the axial plasma density n_{e} from data set 2 (blue) is shown again, in addition to the data taken for data set 1 (black). There are only a few data points available for data set 1 that are concentrated on an axial plasma density around $2.2 \times 10^{18}\,\mathrm{cm}^{-3}$. The same theory curves were calculated in this graph for data set 1 as were shown in Fig. 6.5 for data set 2. Note that the lines are not identical to the theory lines from Fig. 6.5 because of the differences in the laser parameters for the two data sets. The variation of $W^{\mathrm{m}}_{\mathrm{max}}$ in Fig. 6.6 for data set 1 (black data points) does not exhibit a maximum

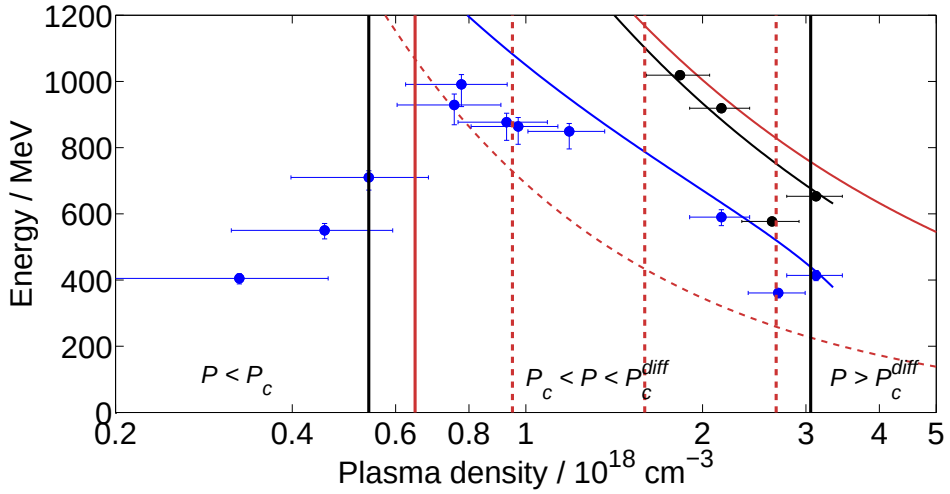

Figure 6.6: The maximum recorded electron energy as a function of the axial plasma density. The graphs shows the data points already shown in Fig. 6.5 (blue) and data points and theory lines for data set 1 (black data points and black and red theory lines). The density for which the dephasing length equals the capillary length is shown by the vertical red line, the density for which the dephasing length equals 5 mm is shown by the right most vertical red dashed line. The dashed line to the left of the 5 mm line, indicated the dephasing length equal to 10 mm, the left most dashed red line indicates the dephasing length of 20 mm. All theory lines were calculated with the formulas referenced in Fig. 6.5. For the data from data set 1, the laser pulse energy within the lowest-order mode was 3.2 J, the maximum incident peak power and focal intensity were $P = 55\,\mathrm{TW}$ and $I = 2.9 \times 10^{18}\,\mathrm{Wcm}^{-2}$, respectively, and the laser was timed to arrive at the peak of the discharge current. The energy was corrected for the electron beam pointing (the pointing-correction systems were in place when these data were taken) and the energy error bars result from the systematic error of the energy determination, which were small. The pressure error bars result from the measurement error of the pressure which are of order millibar.

as seen for data set 2 (blue data points). This results from the fact that the data was taken in a regime in which the capillary is much longer than the dephasing length, as discussed in §6.2.4. The density for which the dephasing length equals the capillary length is shown by the vertical red line and lies at much lower pressures than used during acquisition of data set 1. The dephasing length for pressures used lies between 5 mm and 10 mm, as indicated by the red dashed lines.

Fig. 6.6 also shows the maximum energy calculated for the cases of: no self-focusing (red, dashed), self-focusing to w_{sf} (red, solid), and a correction for the finite transmission of the plasma channel (black, solid). Considering self-focusing improves the agreement of the data with theory. Taking into account the finite transmission reduces the expected maximum energy by 8.5 % and improves the agreement with the data further, just as it did for data set 1.

6.2.6 Low density injection

Electron beams were generated for plasma densities as low as $3.25 \times 10^{17} \mathrm{cm}^{-3}$, as can be seen in Fig. 6.5, and the bunch charge measured at this plasma density was 5.1 pC. This is the lowest density at which electron injection and acceleration have been observed with electron energies of above 500 MeV. Analysis of experimental results by Mangles et al. [118,119] and theoretical calculations by Tsung et al. [120] and Lu et al. [43, 121] predict that the threshold for self-injection is $a_0 \geq 3$. Given the relatively low value of the normalised vector potential of the input pulse ($a_{0,\mathrm{in}} = 1.1$), it is apparent that self-injection could only occur in our experiment if the laser pulse experiences substantial self-focusing and pulse compression. However, at this low density, self-focusing only increases the normalized vector potential to $a_0 \approx 1.7$ and laser pulse compression was measured to be of the order of 10 %. An alternative analysis [108] of the threshold condition predicts that, for our conditions, the input laser pulse energy would have to exceed 190 J for self-injection to occur. Given this, it is clear that self-injection could not occur at the lowest plasma densities for which electron beams were observed, and instead another mechanism, such as ionisation injection [27, 60, 61], must play a role. Simulations are needed to explain which mechanisms is responsible for electron injection and the dynamics of acceleration over the long laser-plasma interaction lengths achieved in these experiments. Initial simulation results are presented in the next paragraph.

The mechanism for injection was investigated by using the simulation codes WAKE [122] and OSIRIS [123]. The simulations lead to the initial estimate, that electron injection is very likely due to ionisation injection, because: (i) at the simulated densities of $n_\mathrm{e} = 0.45 \times 10^{18} \mathrm{cm}^{-3}$ and $n_\mathrm{e} = 1.2 \times 10^{18} \mathrm{cm}^{-3}$, self-injection is not observed; and (ii) impurities in the gas supply line of either Nitrogen and Oxygen, or from Aluminium (from the sapphire capillary made of Al_2O_3), are seen to be ionised and accelerated. The reason why these impurities are only participially ionised, is, that the energy of the electrical discharge is not high enough to fully ionise these molecules, and only the peak of the laser pulse is high enough to ionise the inner shell electrons. Hence electrons born at the peak of the laser pulse are injected into the wake at the right phase and are accelerated as discussed in §2.5.4. These initial simulations have to be confirmed by more extensive, additional simulations.

It is worth noting, that, if, for the lowest density, the length of the plasma channel were properly matched to the dephasing length of 80 mm, electrons would be accelerated to energies significantly above 1 GeV.

6.3 Characterization of temporal laser pulse compression

During the taking of data set 2, the transmitted laser light was analysed by a GRENOUILLE. Electrons accelerated during the measurement had an average energy of 655 MeV and charges between 3-5 pC. Fig. 6.7 shows the transmission of the laser energy and the FWHM of the retrieved intensity profiles of the transmitted laser pulses as a function of the on-axis plasma density. It can be seen that the pulse duration decreases linearly with plasma density until it reaches the resolution of the GRENOUILLE. The linear decrease is in reason-

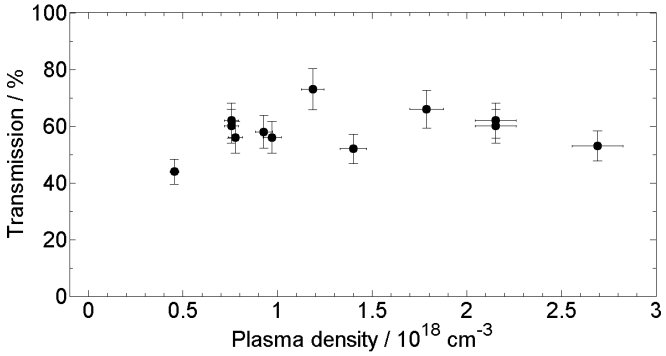

(a)

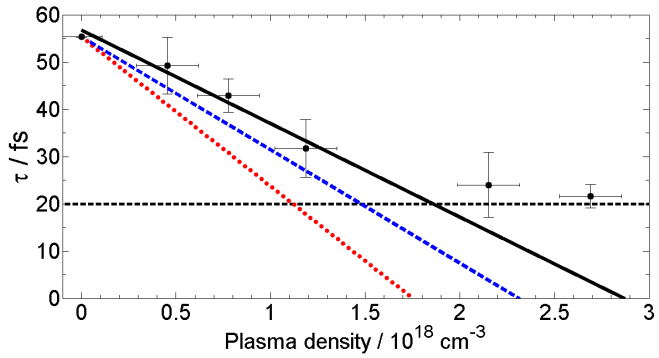

(b)

Figure 6.7: (a) The transmission of the laser energy as a function of plasma density. (b) The FWHM of the retrieved temporal intensity profiles of the transmitted laser pulses as a function of the on-axis plasma density. The horizontal black dotted line shows the resolution of the FROG; the model from [31], used in equation 2.19, is shown in for $x = 25\,\text{mm}$ (blue, short dash) — which is the distance between the gas slots inside the capillary — and $x = 33\,\text{mm}$ (red, long dash) — which is the length of the capillary — as well as a linear fit to the data (black, solid). The vertical error bars are the statistical error, and the pressure error bars result from the measurement error of the pressure which are of order millibar as well as the uncertainty of the on-axis density calculation.

able agreement with the simple model proposed by Schreiber et al. [31] (red and blue dashed lines), which states that the rear of the pulse propagates at a different speed compared to the front of the pulse (equation 2.19). The measured rate of compression is $(23 \pm 5)\,\text{fs}/10^{18}\,\text{cm}^{-3}$ whereas the model predicts a compression rate of $32\,\text{fs}/10^{18}\,\text{cm}^{-3}$.

Fig. 6.8 shows the temporal intensity profile for axial electron density $n_e = 0, 0.45, 0.78$, and $1.2 \times 10^{18}\,\text{cm}^{-3}$.These show clearly the evolution from the quasi-linear to the highly non-linear regime: at low densities the laser pulse exhibits compression at the rear of the pulse (at positive times), and little change to the front; the photons at the rear are being accelerated and the pulse compresses asymmetrically from the back. At the highest densities, significant steepening of the front of the pulse is observed; this is consistent with photon deceleration at the front of the laser pulse: due to the more substantial plasma wave excitation at higher densities, photons at the front loose significant energy and the pulse shortens from the front.

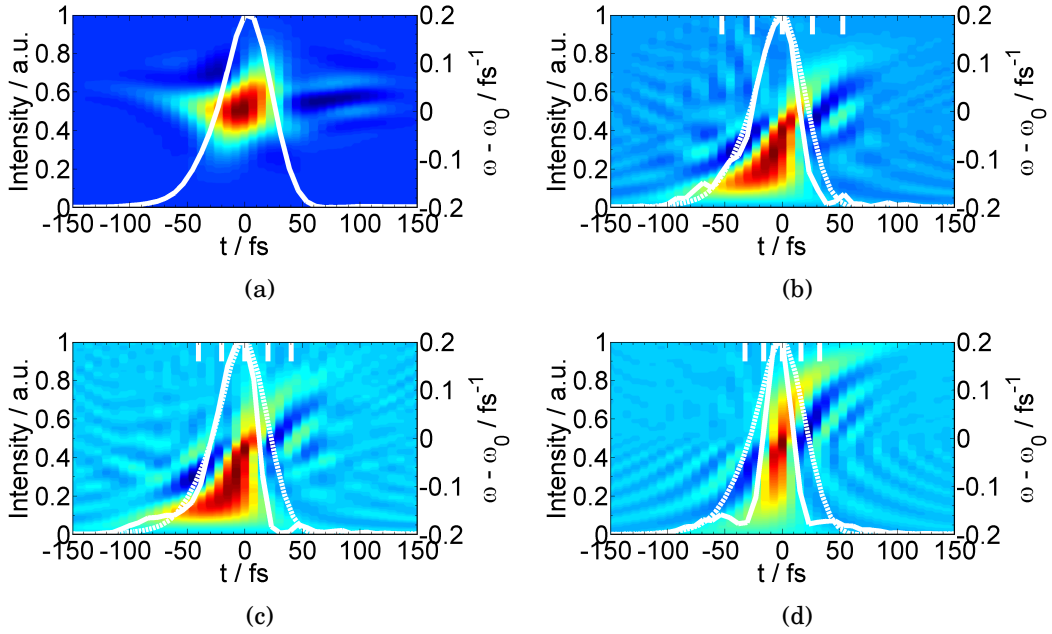

Figure 6.8: Retrieved temporal intensity profiles (white solid line) for the vacuum laser pulse (a), and for axial electron densities $n_e = 0.45 \times 10^{18}\,\mathrm{cm}^{-3}$ (b), $n_e = 0.78 \times 10^{18}\,\mathrm{cm}^{-3}$ (c), and $n_e = 1.2 \times 10^{18}\,\mathrm{cm}^{-3}$ (d). In each case the white, vertical lines indicate the plasma period and a white dashed line shows the vacuum pulse measurement. The Wigner transform is shown as the background.

For the conditions of these experiments there is little or no formation of pre- or post-pulses. That this is the case for the highest density investigated might be considered surprising since in that case the ratio of the input pulse length to the linear plasma wavelength, λ_p^0, is: $c\tau_0/\lambda_p^0 = 0.8$. However, for our conditions strong relativistic self-focusing and temporal compression substantially increase a_0 from its input value $a_0^{in} = 1.2$, thereby extending the nonlinear plasma wavelength $\lambda_p = \sqrt{a_0}\lambda_p^0$ sufficiently for the laser pulse to fit within half a plasma period.

The corresponding Wigner transforms of these pulses are shown in the background of Fig. 6.8. These show clearly that the temporal compression of the pulse is associated with an increase in the spectral width; as expected, this arises from significant red-shifting of the front of the pulse (negative times) together with some blue-shifting of the rear (positive times). At the highest density shown the spectral broadening remains large, but the frequency chirp is small, corresponding to transform-limited pulse of 31.7 ± 6.1 fs duration. For these conditions electron beams with a maximum energy of up to 991^{+30}_{-67} MeV and charges between 3-5 pC were observed [124, 125]. Fig. 6.9 shows the exact electron beam spectra from which the laser pulse has been analysed for Fig. 6.8 and Fig. 6.7 (b).

6.4 Simulations

To verify the pulse compression seen in the experiment, the simulation codes WAKE [122] was used. The preliminary, simulated, temporal intensity profiles is shown in Fig. 6.10 for

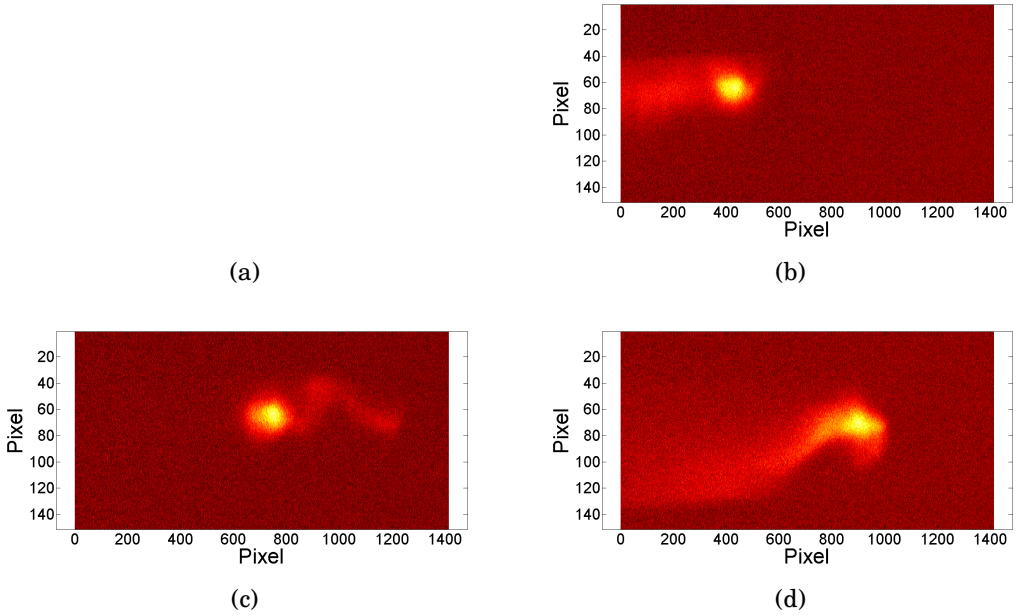

Figure 6.9: The actual electron beams from the pulse compression measurement. (a) The space for the vacuum shot is left empty. (b-d) The electron beam for axial electron densities $n_e = 0.45\,(\mathrm{b}), 0.78\,(\mathrm{c})\,\mathrm{and}\,1.2\,(\mathrm{d}) \times 10^{18}\,\mathrm{cm}^{-3}$, which correspond to Fig. 6.8 (b), (c), and (d), respectively and the equivalent data points in Fig. 6.7 (b).

the vacuum pulse (a) and the pulse at an axial electron densities of $n_e = 0.45 \times 10^{18}\,\mathrm{cm}^{-3}$ (b). The simulation results for $n_e > 0.45 \times 10^{18}\,\mathrm{cm}^{-3}$ were not finished at this time. Fig. 6.10 (a) and (b) confirm in part the measured data from Fig. 6.8 (a) and (b) with the front of the pulse seen to be red-shifted. However the blueshift at the back is not as pronounced in simulation as during the experiment. This must be further investigated by additional simulations.

6.5 Summary

Results from an experiment at the Astra-Gemini laser facility of the Rutherford Appleton Laboratory were presented. GeV-scale electron beams were generated in the gas-filled capillary discharge waveguide with good reproducibility. Beams of electrons with energies above 900 MeV, and with root-mean-square divergence of 3.5 mrad were presented for a plasma density of $2.2 \times 10^{18}\,\mathrm{cm}^{-3}$ and a peak input laser power of 55 TW. The variation of the maximum electron energy with the plasma density exhibited a clear maximum. The dephasing length for this density was found to be close to but slightly less than the length of the capillary. This is expected since the laser pulse intensifies before injecting electrons. The maximum energy as a function of density exhibited good agreement with models from Lu et al [43]. Electrons were accelerated in three different regimes corresponding to $P > P_c^{\mathrm{diff}}$, $P_c < P < P_c^{\mathrm{diff}}$, and $P < P_c$, which demonstrated that the waveguide works for plasma densi-

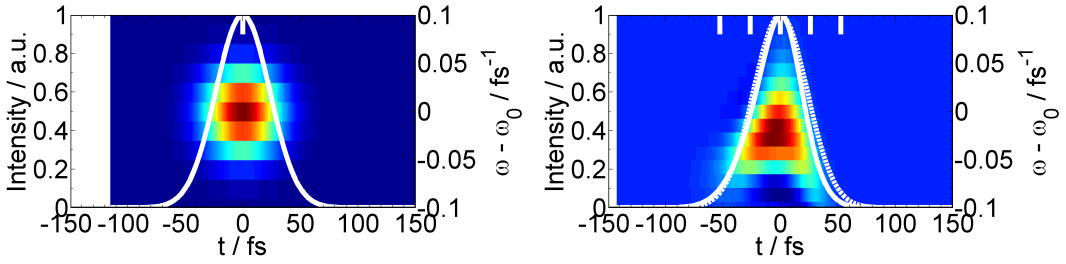

Figure 6.10: Simulated, temporal intensity profiles (white solid line) for the vacuum laser pulse (a), and for axial electron densities $n_e = 0.45 \times 10^{18}\,\mathrm{cm}^{-3}$ (b). The white, vertical lines indicate the plasma period and a white dashed line shows the vacuum pulse measurement. The Wigner transform is shown as the background.

ties in which gas-jets can not operate.

The experiment recorded the first observation of temporal pulse compression within a plasma channel with simultaneous electron acceleration to energies higher than 500 MeV. This measurement suggests that the pulse compresses linearly from the back as predicted by theory. In order to retrieve this information from the GRENOUILLE measurements, a methods by Schreiber et al. [31] was used. This method assumes that the Wigner transform does not change drastically when parameters of the experiments are changed slightly.

The energy spectra of 36 consecutive electron beams were found to be reasonably reproducible, with the observed variations attributable to the measured shot-to-shot jitter of the laser parameters. The laser energy within the first order Gaussian mode was only $< 30\,\%$ and an apodizer was used to improve this percentage to $38\,\%$.

Two methods for correcting the effect of beam pointing variations on the measured energy spectrum were used. While both methods resulted in the same energy correction, the “Pointing" Lanex was significantly easier to implement and the cost was an order of magnitude lower. The time spent to analyse the data was also lower and the “Pointing" Lanex did not degrade the recorded energy spectrum. The dual-peak spectra recorded with the electron spectrometer could arise either from trapping of electrons in two “buckets” or from a hybrid acceleration scheme in which the firstly injected electron bunch drives its own wakefield, which can inject and accelerate a trailing electron bunch. Particle-in-cell simulations are being undertaken to elucidate the details of the mechanisms responsible for the dual-beam spectra.

The results show that waveguides are a good way forward towards achieving reproducible, GeV-scale electron beams.

Chapter 7

Conclusion

This thesis discussed several experiments which aimed to improve the acceleration and characterisation of laser wakefield accelerated electrons. The findings of this thesis as well as suggested future work are summarized in this chapter.

7.1 Summary

In chapter 2, we introduced the principles behind laser plasma accelerators and their capabilities. The high accelerating gradients achievable in LWFA allow the electrons to be accelerated to the target energy over a distance that is as much as three orders of magnitude less than that required by a conventional accelerator. This has the potential to dramatically decrease the size and cost of accelerators which, in turn, could make them more available to scientists. Because of their smaller size, but also because they produce intrinsically short duration electron bunches, plasma accelerators are projected to be used in future light sources in which radiation is harnessed from the electrons. Radiation from electrons accelerated via laser plasma accelerators has already been demonstrated [126], but the quality of the electron bunches still needs to be improved.

In order to assess the quality of the accelerated electrons, detectors are used, which record parameters such as energy, divergence and pointing stability. To record, to improve, and to stabilise these parameters is crucial for their future use in applications such as light sources. In chapter 3, two such detectors were introduced. Prior to the experiment presented, the calibration of these detectors was not well understood. A scintillating screen, which emits photons when exposed to charged particles, was radiated with a conventionally accelerated electron beam of 505 MeV at the DAFNE beam test facility. The scintillating signal increased linearly with increasing charge density between $\rho = 2 \times 10^{-7}\,\mathrm{C/m^2}$ and $\rho = 10^{-5}\,\mathrm{C/m^2}$. Although expected — or at least hoped for — this linearity had not been demonstrated previously.

In combination with an image plate (IP) — a detector whose calibration does not depend on the individual optical set-up of the experiment — the charge of the electron beam can be deduced. An absolute calibration of the FUJIFILM BAS-IP MS image plate was performed at the DAFNE beam test facility. Prior to this calibration, no experimental results were published and the calibration of the beam charge using this technique were dependent on

simulations. The value used prior to our result, was produced by using the known response [87] to x-rays (not electrons) of a given energy, and using this IP response to simulate the IP response to 1-100 MeV electron beams. The IP sensitivity measurement of our experiment resulted in a value of $S_{MS} = (0.0487 \pm 0.0028)$ PSL. This absolute calibration revealed that the sensitivity of the IP was nearly 2.5 times higher than previously assumed.

The plasma accelerator used by our group since 2005 is the hydrogen-filled capillary discharge waveguide. The redevelopment of its electrical circuit was presented in chapter 4, in which the pulsed discharge circuit was combined with a glow discharge circuit. The combined discharge showed several improvements over the pulsed discharge, among them that the pulsed voltage as well as the electrical noise of the discharge was reduced. However, the combined circuit showed these improvements only in a limited pressure range, i.e. below 10 mbar and above 150 mbar. Previous experiments with the capillary discharge waveguide did not suffer from this limitation and it was, therefore, decided to keep operating the original electrical circuit design for the Astra-Gemini experiment and concentrate on improving the housing of the waveguide.

This housing had not been modified significantly since the capillary discharge waveguide was originally conceived in 2005. The improvements, presented in this thesis, removed the possibility of misfired discharges around the capillary, rather than inside it, by adapting two novel ideas. First, the gas was supplied via two gas pipes, sealed by o-rings, rather than using a reservoir inside the housing. The second idea was to adapt an open design housing, which allowed escaping gas to dissipate into the vacuum, rather than accumulate around the capillary. This eliminated misfired discharges completely. In addition, the housing was miniaturised significantly to be usable for future experiments in which two such capillary discharge waveguides might be employed in series.

The work undertaken to improve the capillary discharge waveguide was employed at an experiment performed at the Astra-Gemini laser facility located at the Rutherford Appleton Laboratory. This was the topic of chapter 5 and chapter 6. The energy spectra of the generated electron beams exhibited good shot-to-shot reproducibility, with the observed variations attributable to the measured shot-to-shot jitter of the laser parameters. Beams of electrons with a maximum energy of 991 MeV were observed. The root-mean-square divergence of the beams was 3.5 mrad, comparable to other self-injection based acceleration experiments. The electron beams were generated with an apodized laser beam with a peak input laser power of 55 TW and at a plasma density of $n_e = 2.2 \times 10^{18}\,\mathrm{cm}^{-3}$. Most spectra showed two beams being accelerated which could arise either from trapping of electrons in two “buckets” or by a hybrid acceleration scheme in which an electron bunch injected first, accelerates a second electron bunch in its wake. Particle-in-cell simulations are necessary to determine the details of the mechanisms responsible.

The variation of the maximum electron energy with the plasma density showed a maximum at $n_e \approx 0.8 \times 10^{18}\,\mathrm{cm}^{-3}$, with the dephasing length for this density being slightly less than the capillary length of 33 mm. The reason for this difference is that the laser pulse evolves within the first few millimeters of the capillary before electrons are injected and accelerated. Electrons were accelerated in three different regimes corresponding to $P > P_c^{\mathrm{diff}}$, $P_c < P < P_c^{\mathrm{diff}}$, and $P < P_c$, which demonstrates that the waveguide works well even in lower plasma densities than previously achieved. When the measured maximum energy was compared to the theoretically achievable energy described by the model of Lu et al. [43], the agreement was good only when the laser energy was reduced to the amount within the first

order Gaussian mode. This adjustment of energy to get agreement with the model and the laser pointing stability — and therefore electron pointing stability — being less than ideal, illustrates the fact, that a powerful laser is not the only thing an experimentalist desires. Rather than the power value alone, a clean focus, near Gaussian beams, and stable pointing are desirable for efficient electron acceleration.

Since laser beam pointing was expected to be high, two methods for correcting the effect of electron beam pointing variations on the measured energy spectrum were prepared. The use of lead bars and two Lanex screens behind the electron spectrometer was found to be useful and is suitable for experiments in which radiation is detected. This second method, however, was much easier to implement and analyze, and employed a Lanex screen in front of the electron spectrometer. This so-called “Pointing" Lanex did not degrade the recorded energy spectrum.

The experiment presented here also recorded the first observation of temporal compression of a laser pulse within a plasma channel with simultaneous electron acceleration to energies higher than 500 MeV. Because the direction of time of the temporal intensity measured with a GRENOUILLE is unknown, a suggestion by Schreiber et al. [31] was employed to determine it. The results show, that the pulse compressed linearly from the back, as predicted by theory, and the rate of compression with density is $23\,\mathrm{fs}/10^{18}\,\mathrm{cm}^{-3}$. The results were in reasonably agreement with presented simulations.

The results presented in this thesis prove that the capillary discharge waveguide with its new housing is well suited to achieve reproducible, GeV-scale electron beams. With the re-development of the housing, future staging experiments can now use two of these waveguides in series. Furthermore, the charge calibration of the image plates enables all future experiments using this technique to report correct charge values.

7.2 Future work

This section gives an overview of the issues that, from the author’s point of view, still need to be resolved.

The detector calibrations by the author were confirmed by other thesis work and publications [18, 83, 84]. However, all groups – including the author’s — employed electron bunches of durations which are 3-6 orders of magnitude longer than the duration of electron bunches produced via LWFA, which is of order femtoseconds. It would, therefore, be beneficial to calibrate the detectors at a facility such as SparX — which uses 70-200 fs short electron bunches — to see if the saturation of the detectors affects the detection of charge.

The results in chapter 6 of the maximum electron energy as a function of plasma density were compared with analytical models described by Lu et al. [43]. The agreement is good when the energy of the laser is adjusted to represent only the fraction contained within the first order Gaussian mode. While these models are widely used in LWFA experiments to estimate the expected maximum energy, further particle-in-cell simulations are needed to confirm in more detail the process responsible for the injection and the dual-peaked electron spectra observed in our experiment.

The laser engineers at the Astra-Gemini laser facility work extremely hard to provide

an intense, ultra-short laser pulse. Parameters outside their control, however, such as the vibration produced by a nearby neutron source called ISIS, diminish their work on laser pointing stability. The laser facility is used by many other experiments, among them gas-jet based laser wakefield accelerators. While for other experiments pointing stability is not as important (while still desired), a capillary with a diameter of $200-300\,\mu$m requires that the pointing stability of the laser pulse is high and that vibrations in the building are minimal. During the campaign at Astra-Gemini, electrons were produced during the time ISIS was on and off, but the highest energy electron beams with the best pointing stability were measured during days when ISIS was shut off. This shows that a pointing stabilisation system, such as the one employed at Lund [105], would be beneficial. A system similar to the one at Lund has recently been introduced at the Astra-Gemini target area and it will be crucial to future waveguide experiments.

Our experiment took place right after experiments by a group from Imperial College, London, led by Dr. Stuart Mangles and Professor Zulfikar Najmudin. The experiments operated a gas-jet to accelerate electrons with a laser beam, but most of the diagnostics were shared and the set-up was done together. The collaboration between the groups decreases time spent setting up equipment at the facility and encourages scientific discourse between the different groups. For that, and the fruitful conversation with members of the Imperial College group, the author is extremely thankful. This was not the first time a capillary experiment was performed after a gas-jet experiment, and it should not be the last time.

Bibliography

[1] T. P. A. Ibbotson, N. Bourgeois, T. P. Rowlands-Rees, L. S. Caballero, S. I. Bajlekov, P. A. Walker, S. Kneip, S. P. D. Mangles, S. R. Nagel, C. A. J. Palmer, N. Delerue, G. Doucas, D. Urner, O. Chekhlov, R. J. Clarke, E. Divall, K. Ertel, P. S. Foster, S. J. Hawkes, C. J. Hooker, B. Parry, P. P. Rajeev, M. J. V. Streeter, and S. M. Hooker. 'Laser-wakefield acceleration of electron beams in a low density plasma channel.' *Phys. Rev. ST Accel. Beams*, **13(3)**:031301, Mar 2010. doi:10.1103/PhysRevSTAB.13.031301.

[2] T P A Ibbotson, N Bourgeois, T P Rowlands-Rees, L S Caballero, S I Bajlekov, P A Walker, S Kneip, S P D Mangles, S R Nagel, C A J Palmer, N Delerue, G Doucas, D Urner, O Chekhlov, R J Clarke, E Divall, K Ertel, P Foster, S J Hawkes, C J Hooker, B Parry, P P Rajeev, M J V Streeter, and S M Hooker. 'Investigation of the role of plasma channels as waveguides for laser-wakefield accelerators.' *New Journal of Physics*, **12(4)**:045008, 2010.

[3] N. Delerue, R. Bartolini, G. Doucas, P. Lau, K. Peach, A. Reichold, R. Senanayake, D. Urner, P. A. Walker, S. Bajlekov, N. Bourgeois, L. Caballero-Bendixsen, T. P. A. Ibbotson, S. M. Hooker, C. Thomas, G. Mazzitelli, and B Buonomo. 'Single-shot emittance measurement of a 508 Mev electron beam using the pepper-pot method.' In 'Proceedings of the Particle Accelerator Conference,' page paper TH5RFP065. 2009.

[4] T. P. A. Ibbotson. *An Investigation of Laser-Wakefield Acceleration in the Hydrogen-Filled Capillary Discharge Waveguide*. D.Phil. thesis, University of Oxford, 2012.

[5] T. Tajima and J. M. Dawson. 'Laser electron-accelerator.' *Phys. Rev. Lett.*, **43(4)**:267–270, 1979. ISSN 0031-9007.

[6] C. Joshi, T. Tajima, J. M. Dawson, H. A. Baldis, and N. A. Ebrahim. 'Forward raman instability and electron acceleration.' *Phys. Rev. Lett.*, **47**:1285–1288, Nov 1981. doi:10.1103/PhysRevLett.47.1285.

[7] P. Sprangle, E. Esarey, A. Ting, and G. Joyce. 'Laser wakefield acceleration and relativistic optical guiding.' *Appl. Phys. Lett.*, **53(22)**:2146–2148, Nov 28 1988. ISSN 0003-6951.

[8] M. N. Rosenbluth and C. S. Liu. 'Excitation of plasma waves by two laser beams.' *Phys. Rev. Lett.*, **29**:701–705, Sep 1972. doi:10.1103/PhysRevLett.29.701.

[9] E. Esarey, C. B. Schroeder, and W. P. Leemans. 'Physics of laser-driven plasma-based electron accelerators.' *Rev. Mod. Phys.*, **81**:1229–1285, Aug 2009. doi:10.1103/RevModPhys.81.1229.

[10] Donna Strickland and Gerard Mourou. 'Compression of amplified chirped optical pulses.' *Optics Communications*, **56(3)**:219 – 221, 1985. ISSN 0030-4018. doi:10.1016/0030-4018(85)90120-8.

[11] A. Modena, A. E. Najmudin, Z. andDangor, C. E. Clayton, K. A. Marsh, C. Joshi, V. Malka, C. B. Darrow, C. Danson, D. Neely, and F. N. Walsh. 'Electron acceleration from the breaking of relativistic plasma waves.' *Nature*, **377**:606 – 608, 1995.

[12] D. Umstadter, J. K. Kim, and E. Dodd. 'Laser injection of ultrashort electron pulses into wakefield plasma waves.' *Phys. Rev. Lett.*, **76(12)**:2073–2076, Mar 18 1996. ISSN 0031-9007.

[13] V. Malka, S. Fritzler, E. Lefebvre, M. M. Aleonard, F. Burgy, J. P. Chambaret, J. F. Chemin, K. Krushelnick, G. Malka, S. P. D. Mangles, Z. Najmudin, M. Pittman, J. P. Rousseau, J. N. Scheurer, B. Walton, and A. E. Dangor. 'Electron acceleration by a wake field forced by an intense ultrashort laser pulse.' *Science*, **298(5598)**:1596–1600, Nov 22 2002. ISSN 0036-8075.

[14] S. P. D. Mangles, C. D. Murphy, Z. Najmudin, A. G. R. Thomas, J. L. Collier, A. E. Dangor, E. J. Divall, P. S. Foster, J. G. Gallacher, C. J. Hooker, D. A. Jaroszynski, A. J. Langley, W. B. Mori, P. A. Norreys, F. S. Tsung, R. Viskup, B. R. Walton, and K. Krushelnick. 'Monoenergetic beams of relativistic electrons from intense laser-plasma interactions.' *Nature*, **431(7008)**:535–538, Sep 30 2004. ISSN 0028-0836.

[15] J. Faure, Y. Glinec, A. Pukhov, S. Kiselev, S. Gordienko, E. Lefebvre, J. P. Rousseau, F. Burgy, and V. Malka. 'A laser-plasma accelerator producing monoenergetic electron beams.' *Nature*, **431(7008)**:541–544, Sep 30 2004. ISSN 0028-0836.

[16] C. G. R. Geddes, C. Tóth, J. van Tilborg, E. Esarey, C. B. Schroeder, D. Bruhwiler, C. Nieter, J. Cary, and W. P. Leemans. 'High-quality electron beams from a laser wakefield accelerator using plasma-channel guiding.' *Nature*, **431(7008)**:538–541, Sep 30 2004. ISSN 0028-0836.

[17] W. P. Leemans, B. Nagler, A. J. Gonsalves, C. S. Tóth, K. Nakamura, C. G. R. Geddes, E. Esarey, C. B. Schroeder, and S. M. Hooker. 'Gev electron beams from a centimetre-scale accelerator.' *Nat. Phys.*, **2(10)**:696–699, 2006.

[18] K. Nakamura, B. Nagler, Cs. Toth, C. G. R. Geddes, C. B. Schroeder, E. Esarey, W. P. Leemans, A. J. Gonsalves, and S. M. Hooker. 'Gev electron beams from a centimeter-scale channel guided laser wakefield accelerator.' *Physics of Plasmas*, **14(5)**:056708, 2007. doi:10.1063/1.2718524.

[19] S. Karsch, J. Osterhoff, A. Popp, T. P. Rowlands-Rees, Z. Major, M. Fuchs, B. Marx, R. Horlein, K. Schmid, L. Veisz, S. Becker, U. Schramm, B. Hidding, G. Pretzler, D. Habs, F. Gruner, F. Krausz, and S. M. Hooker. 'Gev-scale electron acceleration in a gas-filled capillary discharge waveguide.' *New J. Phys.*, **9**:415, Nov 21 2007. ISSN 1367-2630.

[20] G. Genoud, K. Cassou, F. Wojda, H.E. Ferrari, C. Kamperidis, M. Burza, A. Persson, J. Uhlig, S. Kneip, S.P.D. Mangles, A. Lifschitz, B. Cros, and C.-G. Wahlström. 'Laser-plasma electron acceleration in dielectric capillary tubes.' *Applied Physics B*, **105**:309–316, 2011. ISSN 0946-2171. doi:10.1007/s00340-011-4639-4.

[21] Haiyang Lu, Mingwei Liu, Wentao Wang, Cheng Wang, Jiansheng Liu, Aihua Deng, Jiancai Xu, Changquan Xia, Wentao Li, Hui Zhang, Xiaoming Lu, Cheng Wang, Jianzhou Wang, Xiaoyan Liang, Yuxin Leng, Baifei Shen, Kazuhisa Nakajima, Ruxin Li, and Zhizhan Xu. 'Laser wakefield acceleration of electron beams beyond 1 GeV from an ablative capillary discharge waveguide.' *Applied Physics Letters*, **99(9)**:091502, 2011.

[22] S. Kneip, S. R. Nagel, S. F. Martins, S. P. D. Mangles, C. Bellei, O. Chekhlov, R. J. Clarke, N. Delerue, E. J. Divall, G. Doucas, K. Ertel, F. Fiuza, R. Fonseca, P. Foster, S. J. Hawkes, C. J. Hooker, K. Krushelnick, W. B. Mori, C. A. J. Palmer, K. Ta Phuoc, P. P. Rajeev, J. Schreiber, M. J. V. Streeter, D. Urner, J. Vieira, L. O. Silva, and Z. Najmudin. 'Near-gev acceleration of electrons by a nonlinear plasma wave driven by a self-guided laser pulse.' *Phys. Rev. Lett.*, **103**:035002, Jul 2009. doi:10.1103/PhysRevLett.103.035002.

[23] M Z Mo, A Ali, S Fourmaux, P Lassonde, J C Kieffer, and R Fedosejevs. 'Quasimonoenergetic electron beams from laser wakefield acceleration in pure nitrogen.' *Applied Physics Letters*, **100(7)**:074101, 2012.

[24] J Liu, C Xia, W Wang, H Lu, Ch Wang, A Deng, W Li, H Zhang, X Liang, Y Leng, X Lu, C Wang, J Wang, K Nakajima, R Li, and Z Xu. 'All-Optical Cascaded Laser Wakefield Accelerator Using Ionization-Induced Injection.' *Physical Review Letters*, **107(3)**:035001, July 2011.

[25] B Pollock, C Clayton, J Ralph, F Albert, A Davidson, L Divol, C Filip, S Glenzer, K Herpoldt, W Lu, K Marsh, J Meinecke, W Mori, A Pak, T Rensink, J Ross, J Shaw, G Tynan, C Joshi, and D Froula. 'Demonstration of a Narrow Energy Spread, 0.5 ÂĂÂL'GeV Electron Beam from a Two-Stage Laser Wakefield Accelerator.' *Physical Review Letters*, **107(4)**, July 2011.

[26] J. Faure, C. Rechatin, A. Norlin, A. Lifschitz, Y. Glinec, and V. Malka. 'Controlled injection and acceleration of electrons in plasma wakefields by colliding laser pulses.' *Nature*, **444(7120)**:737–739, Dec 7 2006. ISSN 0028-0836.

[27] A. Pak, K. A. Marsh, S. F. Martins, W. Lu, W. B. Mori, and C. Joshi. 'Injection and trapping of tunnel-ionized electrons into laser-produced wakes.' *Phys. Rev. Lett.*, **104**:025003, Jan 2010. doi:10.1103/PhysRevLett.104.025003.

[28] J. Osterhoff, A. Popp, Z. Major, B. Marx, T. P. Rowlands-Rees, M. Fuchs, M. Geissler, R. Hoerlein, B. Hidding, S. Becker, E. A. Peralta, U. Schramm, F. Gruener, D. Habs, F. Krausz, S. M. Hooker, and S. Karsch. 'Generation of stable, low-divergence electron beams by laser-wakefield acceleration in a steady-state-flow gas cell.' *Phys. Rev. Lett.*, **101(8)**:085002, Aug 22 2008. ISSN 0031-9007.

[29] J. Faure, Y. Glinec, J. J. Santos, F. Ewald, J.-P. Rousseau, S. Kiselev, A. Pukhov, T. Hosokai, and V. Malka. 'Observation of laser-pulse shortening in nonlinear plasma waves.' *Phys. Rev. Lett.*, **95(20)**:205003, Nov 2005. doi:10.1103/PhysRevLett.95.205003.

[30] F. Wojda, K. Cassou, G. Genoud, M. Burza, Y. Glinec, O. Lundh, A. Persson, G. Vieux, E. Brunetti, R. P. Shanks, D. Jaroszynski, N. E. Andreev, C.-G. Wahlström, and

B. Cros. 'Laser-driven plasma waves in capillary tubes.' *Phys. Rev. E*, **80(6)**:066403, Dec 2009. doi:10.1103/PhysRevE.80.066403.

[31] J. Schreiber, C. Bellei, S. P. D. Mangles, C. Kamperidis, S. Kneip, S. R. Nagel, C. A. J. Palmer, P. P. Rajeev, M. J. V. Streeter, and Z. Najmudin. 'Complete temporal characterization of asymmetric pulse compression in a laser wakefield.' *Phys. Rev. Lett.*, **105**:235003, Dec 2010. doi:10.1103/PhysRevLett.105.235003.

[32] X. Wang, R. Zgadzaj, N. Fazel, S. A. Yi, X. Zhang, W. Henderson, Y.-Y. Chang, R. Korzekwa, H.-E. Tsai, C.-H. Pai, Z. Li, H. Quevedo, G. Dyer, E. Gaul, M. Martinez, A. Bernstein, T. Borger, M. Spinks, M. Donovan, S. Y. Kalmykov, V. Khudik, G. Shvets, T. Ditmire, and M. C. Downer. 'Petawatt-laser-driven wakefield acceleration of electrons to 2GeV in $10^{17} cm^{-3}$ plasma.' *AIP Conference Proceedings*, **1507(1)**:341–344, 2012. doi:10.1063/1.4773719.

[33] William Kruer. *The physics of laser plasma interactions*. Addison-Wesley, 1988.

[34] C. D. Murphy. *Diagnosis of High Energy Electron Beams Produced by Laser Wakefield Accelerators*. D.Phil. thesis, Imperial College London, 2007.

[35] J. Wark. *Plasma Physics - lecture notes*. 2008.

[36] John M. Dawson. 'Nonlinear electron oscillations in a cold plasma.' *Phys. Rev.*, **113**:383–387, Jan 1959. doi:10.1103/PhysRev.113.383.

[37] P. Sprangle, E. Esarey, and A. Ting. 'Nonlinear theory of intense laser-plasma interactions.' *Phys. Rev. Lett.*, **64**:2011–2014, Apr 1990. doi:10.1103/PhysRevLett.64.2011.

[38] Paul Gibbon. *Short pulse laser interactions with matter : an introduction*. Imperial College Press, London, 2005.

[39] P. Sprangle, Cha-Mei Tang, and E. Esarey. 'Relativistic self-focusing of short-pulse radiation beams in plasmas.' *Plasma Science, IEEE Transactions on*, **15(2)**:145 –153, april 1987. ISSN 0093-3813. doi:10.1109/TPS.1987.4316677.

[40] E. Esarey, P. Sprangle, J. Krall, and A. Ting. 'Self-focusing and guiding of short laser pulses in ionizing gases and plasmas.' *Quantum Electronics, IEEE Journal of*, **33(11)**:1879 –1914, nov 1997. ISSN 0018-9197. doi:10.1109/3.641305.

[41] W.B. Mori. 'The physics of the nonlinear optics of plasmas at relativistic intensities for short-pulse lasers.' *Quantum Electronics, IEEE Journal of*, **33(11)**:1942 –1953, nov 1997. ISSN 0018-9197. doi:10.1109/3.641309.

[42] P. Sprangle, B. Hafizi, J. R. Penano, R. F. Hubbard, A. Ting, C. I. Moore, D. F. Gordon, A. Zigler, D. Kaganovich, and T. M. Antonsen. 'Wakefield generation and gev acceleration in tapered plasma channels.' *Phys. Rev. E*, **6305(5)**:–, May 2001. ISSN 1063-651X.

[43] W. Lu, M. Tzoufras, C. Joshi, F. S. Tsung, W. B. Mori, J. Vieira, R. A. Fonseca, and L. O. Silva. 'Generating multi-gev electron bunches using single stage laser wakefield acceleration in a 3d nonlinear regime.' *Phys. Rev. STAB*, **10(6)**:061301, Jun 2007. ISSN 1098-4402.

[44] D. F. Gordon, B. Hafizi, R. F. Hubbard, J. R. Peñano, P. Sprangle, and A. Ting. 'Asymmetric self-phase modulation and compression of short laser pulses in plasma channels.' *Phys. Rev. Lett.*, **90**:215001, May 2003. doi:10.1103/PhysRevLett.90.215001.

[45] T. P. Rowlands-Rees. *Laser Wakefield Acceleration in the Hydrogen-Filled Capillary Discharge Waveguide*. D.Phil. thesis, University of Oxford, 2009.

[46] C. D. Decker, W. B. Mori, K.-C. Tzeng, and T. Katsouleas. 'The evolution of ultra-intense, short-pulse lasers in underdense plasmas.' *Physics of Plasmas*, **3(5)**:2047–2056, 1996. doi:10.1063/1.872001.

[47] T. Katsouleas, S. Wilks, P. Chen, J. M. Dawson, and J. J. Su. 'Beam loading in plasma accelerators.' *Particle Accelerators*, **22**:81–99, 1987.

[48] M. Tzoufras, W. Lu, F. S. Tsung, C. Huang, W. B. Mori, T. Katsouleas, J. Vieira, R. A. Fonseca, and L. O. Silva. 'Beam loading in the nonlinear regime of plasma-based acceleration.' *Phys. Rev. Lett.*, **101**:145002, Sep 2008. doi:10.1103/PhysRevLett.101.145002.

[49] M. Tzoufras, W. Lu, F. S. Tsung, C. Huang, W. B. Mori, T. Katsouleas, J. Vieira, R. A. Fonseca, and L. O. Silva. 'Beam loading by electrons in nonlinear plasma wakes.' *Physics of Plasmas*, **16(5)**:056705, 2009. doi:10.1063/1.3118628.

[50] A. Pukhov and J. Meyer-ter Vehn. 'Laser wake field acceleration: the highly nonlinear broken-wave regime.' *Appl. Phys. B*, **74(4-5)**:355–361, Apr 2002. ISSN 0946-2171.

[51] Carl B. Schroeder and Michael H. Helle. 'Summary report of working group 1: Laser-plasma accelerators.' *AIP Conference Proceedings*, **1507(1)**:199–203, 2012. doi:10.1063/1.4773694.

[52] M. Fuchs. *Laser-Driven Soft-X-Ray Undulator Source*. D.Phil. thesis, Ludwig-Maximilians-Universität München, 2010.

[53] C. B. Schroeder, E. Esarey, B. A. Shadwick, and W. P. Leemans. 'Trapping, dark current, and wave breaking in nonlinear plasma waves.' *Physics of Plasmas*, **13(3)**:033103, 2006. doi:10.1063/1.2173960.

[54] C Rechatin, J Faure, A Lifschitz, X Davoine, E Lefebvre, and V Malka. 'Quasi-monoenergetic electron beams produced by colliding cross-polarized laser pulses in underdense plasmas.' *New Journal of Physics*, **11(1)**:013011, 2009.

[55] S. Bulanov, N. Naumova, F. Pegoraro, and J. Sakai. 'Particle injection into the wave acceleration phase due to nonlinear wake wave breaking.' *Phys. Rev. E*, **58(5)**:R5257–R5260, Nov 1998. ISSN 1063-651X.

[56] C. G. R. Geddes, K. Nakamura, G. R. Plateau, C. Tóth, E. Cormier-Michel, E. Esarey, C. B. Schroeder, J. R. Cary, and W. P. Leemans. 'Plasma-density-gradient injection of low absolute-momentum-spread electron bunches.' *Phys. Rev. Lett.*, **100(21)**:215004, May 30 2008. ISSN 0031-9007.

[57] A. J. Gonsalves, K. Nakamura, C. Lin, D. Panasenko, S. Shiraishi, T. Sokollik, C. Benedetti, C. B. Schroeder, C. G. R. Geddes, J. van Tilborg, J. Osterhoff, E. Esarey, C. Toth, and W. P. Leemans. 'Tunable laser plasma accelerator based on longitudinal density tailoring.' *Nat. Phys.*, **7**:862–866, 2011.

[58] K. Schmid, A. Buck, C. M. S. Sears, J. M. Mikhailova, R. Tautz, D. Herrmann, M. Geissler, F. Krausz, and L. Veisz. 'Density-transition based electron injector for laser driven wakefield accelerators.' *Phys. Rev. ST Accel. Beams*, **13**:091301, Sep 2010. doi:10.1103/PhysRevSTAB.13.091301.

[59] M. Chen, E. Esarey, C. B. Schroeder, C. G. R. Geddes, and W. P. Leemans. 'Theory of ionization-induced trapping in laser-plasma accelerators.' *Physics of Plasmas*, **19(3)**:033101, 2012. doi:10.1063/1.3689922.

[60] T. P. Rowlands-Rees, C. Kamperidis, S. Kneip, A. J. Gonsalves, S. P. D. Mangles, J. G. Gallacher, E. Brunetti, T. Ibbotson, C. D. Murphy, P. S. Foster, M. J. V. Streeter, F. Budde, P. A. Norreys, D. A. Jaroszynski, K. Krushelnick, Z. Najmudin, and S. M. Hooker. 'Laser-driven acceleration of electrons in a partially ionized plasma channel.' *Phys. Rev. Lett.*, **100(10)**:105005, Mar 14 2008. ISSN 0031-9007.

[61] C. McGuffey, A. G. R. Thomas, W. Schumaker, T. Matsuoka, V. Chvykov, F. J. Dollar, G. Kalintchenko, V. Yanovsky, A. Maksimchuk, K. Krushelnick, V. Yu. Bychenkov, I. V. Glazyrin, and A. V. Karpeev. 'Ionization induced trapping in a laser wakefield accelerator.' *Phys. Rev. Lett.*, **104**:025004, Jan 2010. doi:10.1103/PhysRevLett.104.025004.

[62] C. E. Clayton, J. E. Ralph, F. Albert, R. A. Fonseca, S. H. Glenzer, C. Joshi, W. Lu, K. A. Marsh, S. F. Martins, W. B. Mori, A. Pak, F. S. Tsung, B. B. Pollock, J. S. Ross, L. O. Silva, and D. H. Froula. 'Self-guided laser wakefield acceleration beyond 1 gev using ionization-induced injection.' *Phys. Rev. Lett.*, **105**:105003, Sep 2010. doi:10.1103/PhysRevLett.105.105003.

[63] M. Tzoufras, C. Huang, J. H. Cooley, F. S. Tsung, J. Vieira, and W. B. Mori. 'Simulations of efficient laser wakefield accelerators from 1 to 100gev.' *Journal of Plasma Physics*, **78**:401–412, 7 2012. ISSN 1469-7807. doi:10.1017/S0022377812000232.

[64] A. J. Gonsalves. *Investigation of a Hydrogen-filled Capillary Discharge Waveguide for Laser-driven Plasma Accelerators*. D.Phil. thesis, University of Oxford, 2006.

[65] F. Dorchies, J. R. Marquès, B. Cros, G. Matthieussent, C. Courtois, T. Vélikoroussov, P. Audebert, J. P. Geindre, S. Rebibo, G. Hamoniaux, and F. Amiranoff. 'Monomode guiding of $10^{16} W/cm^2$ laser pulses over 100 Rayleigh lengths in hollow capillary dielectric tubes.' *Phys. Rev. Lett.*, **82**:4655–4658, Jun 1999. doi:10.1103/PhysRevLett.82.4655.

[66] B. Cros, C. Courtois, G. Matthieussent, A. Di Bernardo, D. Batani, N. Andreev, and S. Kuznetsov. 'Eigenmodes for capillary tubes with dielectric walls and ultraintense laser pulse guiding.' *Phys. Rev. E*, **65**:026405, Jan 2002. doi:10.1103/PhysRevE.65.026405.

[67] N. E. Andreev, M. V. Chegotov, B. Cros, P. Mora, and G. Vieux. 'Spectral diagnostics of laser wakefield in capillary tubes.' *Physics of Plasmas*, **13(5)**:053109, 2006. doi:10.1063/1.2201537.

[68] B. Cros, J. Ju, A. Dopp, K. Cassou, H. E. Ferrari, G. Maynard, G. Genoud, F. Wojda, K. Svensson, M. Burza, O. Lundh, A. Persson, and C.-G. Wahlström. 'Electron beams and x ray radiation generated by laser wakefield in capillary tubes.' *AIP Conference Proceedings*, **1507(1)**:267–272, 2012. doi:10.1063/1.4773705.

[69] P. Sprangle and E. Esarey. 'Interaction of ultrahigh laser fields with beams and plasmas.' *Physics of Fluids B: Plasma Physics*, **4(7)**:2241–2248, 1992. doi:10.1063/1.860192.

[70] C. G. Durfee, J. Lynch, and H. M. Milchberg. 'Development of a plasma waveguide for high-intensity laser pulses.' *Phys. Rev. E*, **51**:2368–2389, Mar 1995. doi:10.1103/PhysRevE.51.2368.

[71] P. Volfbeyn, E. Esarey, and W. P. Leemans. 'Guiding of laser pulses in plasma channels created by the ignitor-heater technique.' *Physics of Plasmas*, **6(5)**:2269–2277, 1999. doi:10.1063/1.873503.

[72] D. J. Spence and S. M. Hooker. 'Investigation of a hydrogen plasma waveguide.' *Phys. Rev. E*, **63(2)**:015401, Jan 2001. ISSN 1063-651X.

[73] Arie Zigler, B. Greenberg, T. Palhan, D. Kaganovich, R. F. Hubbard, A. Ting, T. G. Jones, and P. Sprangle. 'Ablative and discharge capillaries for optical guiding and velocity control.' *AIP Conference Proceedings*, **647(1)**:47–53, 2002. doi:10.1063/1.1524857.

[74] Takashi Kameshima, Wei Hong, Kiyohiro Sugiyama, Xianlun Wen, Yuchi Wu, Chuanming Tang, Qihua Zhu, Yuqiu Gu, Baohan Zhang, Hansheng Peng, Shin ichi Kurokawa, Liming Chen, Toshiki Tajima, Tetsuro Kumita, and Kazuhisa Nakajima. '0.56 gev laser electron acceleration in ablative-capillary-discharge plasma channel.' *Applied Physics Express*, **1(6)**:066001, 2008. doi:10.1143/APEX.1.066001.

[75] R.A. Bendoyro, R.I. Onofrei, J. Sampaio, R. Macedo, G. Figueira, and N.C. Lopes. 'Plasma channels for electron accelerators using discharges in structured gas cells.' *Plasma Science, IEEE Transactions on*, **36(4)**:1728 –1733, aug. 2008. ISSN 0093-3813. doi:10.1109/TPS.2008.927145.

[76] D. Spence. *Plasma Waveguides for High-Intensity Laser Pulses*. D.Phil. thesis, University of Oxford, 2001.

[77] A. Butler. *Short-Wavelength Lasers Driven in Capillary-Discharge Plasma Waveguides*. D.Phil. thesis, University of Oxford, 2003.

[78] A. Butler, D. J. Spence, and S. M. Hooker. 'Guiding of high-intensity laser pulses with a hydrogen-filled capillary discharge waveguide.' *Phys. Rev. Lett.*, **89(18)**:185003, Oct 28 2002. ISSN 0031-9007.

[79] A. J. Gonsalves, T. P. Rowlands-Rees, B. H. P. Broks, J. J. A. M. van der Mullen, and S. M. Hooker. 'Transverse interferometry of a hydrogen-filled capillary discharge waveguide.' *Phys. Rev. Lett.*, **98(2)**:025002, Jan 12 2007. ISSN 0031-9007.

[80] A. Zigler, Y. Ehrlich, C. Cohen, J. Krall, and P. Sprangle. 'Optical guiding of high-intensity laser pulses in a long plasma channel formed by a slow capillary discharge.' *J. Opt. Soc. Am. B*, **13(1)**:68–71, Jan 1996. doi:10.1364/JOSAB.13.000068.

[81] N. A. Bobrova, A. A. Esaulov, J.-I. Sakai, P. V. Sasorov, D. J. Spence, A. Butler, S. M. Hooker, and S. V. Bulanov. 'Simulations of a hydrogen-filled capillary discharge waveguide.' *Phys. Rev. E*, **65**:016407, Dec 2001. doi:10.1103/PhysRevE.65.016407.

[82] B. H. P. Broks, K. Garloff, and J. J. A. M. van der Mullen. 'Nonlocal-thermal-equilibrium model of a pulsed capillary discharge waveguide.' *Physical Review E*, **71(1)**:016401, Jan 2005. doi:10.1103/PhysRevE.71.016401.

[83] A. Buck, K. Zeil, A. Popp, K. Schmid, A. Jochmann, S. D. Kraft, B. Hidding, T. Kudyakov, C. M. S. Sears, L. Veisz, S. Karsch, J. Pawelke, R. Sauerbrey, T. Cowan, F. Krausz, and U. Schramm. 'Absolute charge calibration of scintillating screens for relativistic electron detection.' *Review of Scientific Instruments*, **81(3)**:033301, 2010. doi:10.1063/1.3310275.

[84] K. Zeil, S. D. Kraft, A. Jochmann, F. Kroll, W. Jahr, U. Schramm, L. Karsch, J. Pawelke, B. Hidding, and G. Pretzler. 'Absolute response of fuji imaging plate detectors to picosecond-electron bunches.' *Review of Scientific Instruments*, **81(1)**:013307, 2010. doi:10.1063/1.3284524.

[85] J. Beringer et al. 'Review of particle physics.' *Phys. Rev. D*, **86**:010001, Jul 2012. doi:10.1103/PhysRevD.86.010001.

[86] S. P. D. Mangles. *Measurements of Relativistic Electrons from Intense Laser-Plasma Interactions*. D.Phil. thesis, Imperial College London, 2005.

[87] S. G. Gales and C. D. Bentley. 'Image plates as x-ray detectors in plasma physics experiments.' *Review of Scientific Instruments*, **75(10)**:4001 –4003, oct 2004. ISSN 0034-6748. doi:10.1063/1.1789256.

[88] N. Metropolis and S. Ulam. 'The monte carlo method.' *Journal of the American Statistical Association*, **44(247)**:335–341, 1949. doi:10.1080/01621459.1949.10483310.

[89] J. S. Coursey M. J. Berger and M. A. Zucker. 'Estar; computer program for calculating stopping- power and range tables for electrons.'

[90] G. Vignola et al. 'Status report on dafne.' *Second Workshop on Physics and Detectors for DAFNE in Frascati*, 1995.

[91] Bergoz Instrumentation. 'Integrating current transformer user's manual rev. 3.0.'

[92] 'Fuji internal report - http://www.fujifilm.com/products/lifescience/siimgplate/img plate.html.'

[93] L. Slifkin. 'Dynamics of self-trapped hole processes in agcl.' *Journal of Physics: Condensed Matter*, **13(10)**:2347, 2001.

[94] A. L. Meadowcroft, C. D. Bentley, and E. N. Stott. 'Evaluation of the sensitivity and fading characteristics of an image plate system for x-ray diagnostics.' *Review of Scientific Instruments*, **79(11)**:113102, 2008. doi:10.1063/1.3013123.

[95] Y. Glinec, J. Faure, A. Guemnie-Tafo, V. Malka, H. Monard, J. P. Larbre, V. De Waele, J. L. Marignier, and M. Mostafavi. 'Absolute calibration for a broad range single shot electron spectrometer.' *Review of Scientific Instruments*, **77(10)**:103301 –103301–6, oct 2006. ISSN 0034-6748. doi:10.1063/1.2360988.

[96] T. Radcliffe, G. Barnea, B. Wowk, R. Rajapakshe, and S. Shalev. 'Monte carlo optimization of metal/phosphor screens at megavoltage energies.' *Medical Physics*, **20(4)**:1161–1169, 1993. doi:10.1118/1.596970.

[97] A. H. von Engel. *Ionised Gases*. Oxford University Press, 1964.

[98] Y. P. Raizer. *Gas Discharge Physics*. New York: Springer, 1991.

[99] A Marotta and C A Arguello. 'A simmered pre-pulsed flashlamp dye laser.' *Journal of Physics E: Scientific Instruments*, **9(6)**:478, 1976.

[100] David M. Gaudiosi, Brendan Reagan, Tenio Popmintchev, Michael Grisham, Mark Berrill, Oren Cohen, Barry C. Walker, Margaret M. Murnane, Henry C. Kapteyn, and Jorge J. Rocca. 'High-order harmonic generation from ions in a capillary discharge.' *Phys. Rev. Lett.*, **96**:203001, May 2006. doi:10.1103/PhysRevLett.96.203001.

[101] F. M. Penning. *Electrical Discharges in Gases*. Philips Technical Library, 1957.

[102] D.A Jaroszynski, R Bingham, E Brunetti, B Ersfeld, J Gallacher, B van der Geer, R Issac, S.P Jamison, D Jones, M de Loos, A Lyachev, V Pavlov, A Reitsma, Y Saveliev, G Vieux, and S.M Wiggins. 'Radiation sources based on laser-plasma interactions.' **364(1840)**:689–710, 2006. doi:10.1098/rsta.2005.1732.

[103] D. M. Gaudiosi. *High power ultrafast laser design and high-order harmonic generation in capillary discharge plasmas*. D.Phil. thesis, University of Colorado, 2007.

[104] C.J. Hooker, J.L. Collier, O. Chekhlov, R. Clarke, E. Divall, K. Ertel, B. Fell, P. Foster, S. Hancock, A. Langley, D. Neely, J. Smith, and B. Wyborn. 'The astra gemini project - a dual-beam petawatt ti:sapphire laser system.' *J. Phys. IV France*, **133**:673–677, 2006. doi:10.1051/jp4:2006133135.

[105] G. Genoud, F. Wojda, M. Burza, A. Persson, and C.-G. Wahlström. 'Active control of the pointing of a multi-terawatt laser.' *Review of Scientific Instruments*, **82(3)**:033102, 2011. doi:10.1063/1.3556438.

[106] I. Blumenfeld, C. E. Clayton, F. J. Decker, M. J. Hogan, C. K. Huang, R. Ischebeck, R. Iverson, C. Joshi, T. Katsouleas, N. Kirby, W. Lu, K. A. Marsh, W. B. Mori, P. Muggli, E. Oz, R. H. Siemann, D. Walz, and M. M. Zhou. 'Energy doubling of 42 Gev electrons in a metre-scale plasma wakefield accelerator.' *Nature*, **445(7129)**:741–744, Feb 15 2007. ISSN 0028-0836.

[107] B. B. Pollock, J. S. Ross, G. R. Tynan, L. Divol, S. H. Glenzer, V. Leurent, J. P. Palastro, J. E. Ralph, D. H. Froula, C. E. Clayton, K. A. Marsh, A. E. Pak, T. L. Wang, and C. Joshi. 'Two-screen method for determining electron beam energy and deflection from laser wakefield acceleration.' In 'Proc. Particle Accelerator Conference,' Vancouver, Canada, 2009.

[108] S. P. D. Mangles, G. Genoud, M. S. Bloom, M. Burza, Z. Najmudin, A. Persson, K. Svensson, A. G. R. Thomas, and C.-G. Wahlström. 'Self-injection threshold in self-guided laser wakefield accelerators.' *Phys. Rev. ST Accel. Beams*, **15**:011302, Jan 2012. doi:10.1103/PhysRevSTAB.15.011302.

[109] 'http://www.edmundoptics.com/testing-targets/test-targets/resolution-test-targets/1951-usaf-glass-slide-resolution-targets/1790.'

[110] Rick Trebino and Daniel J. Kane. 'Using phase retrieval to measure the intensity and phase of ultrashort pulses: frequency-resolved optical gating.' *J. Opt. Soc. Am. A*, **10(5)**:1101–1111, May 1993. doi:10.1364/JOSAA.10.001101.

[111] Daniel J. Kane and Rick Trebino. 'Single-shot measurement of the intensity and phase of an arbitrary ultrashort pulse by using frequency-resolved optical gating.' *Opt. Lett.*, **18(10)**:823–825, May 1993. doi:10.1364/OL.18.000823.

[112] M. O'Shea, P.and Kimmel, X. Gu, and R. Trebino. 'Highly simplified device for ultrashort-pulse measurement.' *Opt. Lett.*, **26(12)**:932–934, Jun 2001. doi:10.1364/OL.26.000932.

[113] Rick Trebino. *Frequency-Resolved Optical Gating: The Measurement of Ultrashort Laser Pulses*. Springer, 2000.

[114] Kenneth W. DeLong and Rick Trebino. 'Improved ultrashort pulse-retrieval algorithm for frequency-resolved optical gating.' *J. Opt. Soc. Am. A*, **11(9)**:2429–2437, Sep 1994. doi:10.1364/JOSAA.11.002429.

[115] W. Sellmeier. *Ann. Phys. Chem.*, **143**:271, 1871.

[116] B. Hidding, T. Königstein, J. Osterholz, S. Karsch, O. Willi, and G. Pretzler. 'Monoenergetic energy doubling in a hybrid laser-plasma wakefield accelerator.' *Phys. Rev. Lett.*, **104**:195002, May 2010. doi:10.1103/PhysRevLett.104.195002.

[117] S. P. D. Mangles, A. G. R. Thomas, M. C. Kaluza, O. Lundh, F. Lindau, A. Persson, F. S. Tsung, Z. Najmudin, W. B. Mori, C.-G. Wahlström, and K. Krushelnick. 'Laser-wakefield acceleration of monoenergetic electron beams in the first plasma-wave period.' *Phys. Rev. Lett.*, **96**:215001, May 2006. doi:10.1103/PhysRevLett.96.215001.

[118] S. P. D. Mangles, A. G. R. Thomas, O. Lundh, F. Lindau, M. C. Kaluza, A. Persson, C. G. Wahlström, K. Krushelnick, and Z. Najmudin. 'On the stability of laser wakefield electron accelerators in the monoenergetic regime.' *Phys. Plasmas*, **14(5)**:056702, May 2007. ISSN 1070-664X.

[119] S.P.D. Mangles, A.G.R. Thomas, C. Bellei, A.E. Dangor, C. Kamperidis, S. Kneip, S.R. Nagel, L. Willingale, and Z. Najmudin. 'Self-guided wakefield experiments driven by petawatt-class ultrashort laser pulses.' *Plasma Science, IEEE Transactions on*, **36(4)**:1715 –1721, aug. 2008. ISSN 0093-3813. doi:10.1109/TPS.2008.2000961.

[120] F. S. Tsung, Ritesh Narang, W. B. Mori, C. Joshi, R. A. Fonseca, and L. O. Silva. 'Near-gev-energy laser-wakefield acceleration of self-injected electrons in a centimeter-scale plasma channel.' *Phys. Rev. Lett.*, **93**:185002, Oct 2004. doi:10.1103/PhysRevLett.93.185002.

[121] W. Lu, C. Huang, M. Zhou, M. Tzoufras, F. S. Tsung, W. B. Mori, and T. Katsouleas. 'A nonlinear theory for multidimensional relativistic plasma wave wakefields.' *Phys. Plasmas*, **13(5)**:056709, May 2006. ISSN 1070-664X.

[122] Patrick Mora and Jr. Thomas M. Antonsen. 'Kinetic modeling of intense, short laser pulses propagating in tenuous plasmas.' *Physics of Plasmas*, **4(1)**:217–229, 1997. doi:10.1063/1.872134.

[123] R.A. Fonseca, L.O. Silva, F.S. Tsung, V.K. Decyk, W. Lu, C. Ren, W.B. Mori, S. Deng, S. Lee, T. Katsouleas, and J.C. Adam. 'Osiris: A three-dimensional, fully relativistic particle in cell code for modeling plasma based accelerators.' Lecture Notes in Computer Science, pages 342–351. Springer Berlin Heidelberg, 2002. ISBN 978-3-540-43594-5.

[124] P. A. Walker, N. Bourgeois, W. Rittershofer, J. Cowley, N. Kajumba, A. R. Maier, J. Wenz, C. M. Werle, D. R. Symes, P. P. Rajeev, S. J. Hawkes, O. Chekhlov, C. J. Hooker, B. Parry, Y. Tang, V. A. Marshall, S. Karsch, F. Grüner, and S. M. Hooker. 'Electron acceleration driven in plasma channels at the astra-gemini laser facility.' *AIP Conference Proceedings*, **1507(1)**:193–198, 2012. doi:10.1063/1.4773693.

[125] P A Walker, N Bourgeois, W Rittershofer, J Cowley, N Kajumba, A R Maier, J Wenz, C M Werle, S Karsch, F Grüner, D R Symes, P P Rajeev, S J Hawkes, O Chekhlov, C J Hooker, B Parry, Y Tang, and S M Hooker. 'Investigation of gev-scale electron acceleration in a gas-filled capillary discharge waveguide.' *New Journal of Physics*, **15(4)**:045024, 2013.

[126] H. P. Schlenvoigt, K. Haupt, A. Debus, F. Budde, O. Jackel, S. Pfotenhauer, H. Schwoerer, E. Rohwer, J. G. Gallacher, E. Brunetti, R. P. Shanks, S. M. Wiggins, and D. A. Jaroszynski. 'A compact synchrotron radiation source driven by a laser-plasma wakefield accelerator.' *Nat. Phys.*, **4(2)**:130–133, Feb 2008. ISSN 1745-2473.